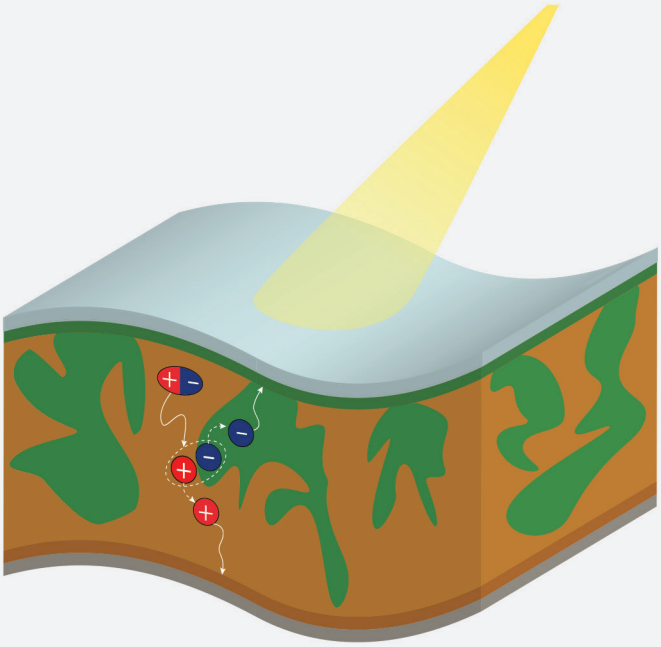

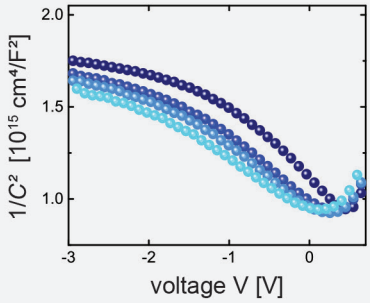

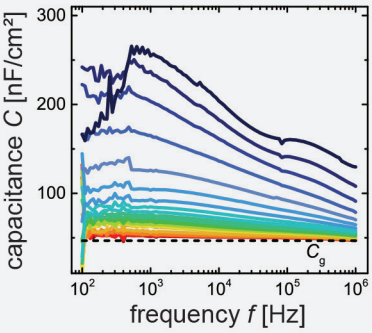

Capacitance-Based Methods to Study Charge Transport and Recombination in Organic Solar Cells

Irene Zonno

Energie & Umwelt / Energy & Environment
Band / Volume 530
ISBN 978-3-95806-528-4

Mitglied der Helmholtz-Gemeinschaft

JÜLICH
Forschungszentrum

Schriften des Forschungszentrums Jülich
Reihe Energie & Umwelt / Energy & Environment Band / Volume 530

Forschungszentrum Jülich GmbH
Institut für Energie- und Klimaforschung
IEK-5 Photovoltaik

Capacitance-Based Methods to Study Charge Transport and Recombination in Organic Solar Cells

Irene Zonno

Schriften des Forschungszentrums Jülich
Reihe Energie & Umwelt / Energy & Environment Band / Volume 530

ISSN 1866-1793 ISBN 978-3-95806-528-4

Bibliografische Information der Deutschen Nationalbibliothek.
Die Deutsche Nationalbibliothek verzeichnet diese Publikation in der
Deutschen Nationalbibliografie; detaillierte Bibliografische Daten
sind im Internet über http://dnb.d-nb.de abrufbar.

Herausgeber und Vertrieb:	Forschungszentrum Jülich GmbH Zentralbibliothek, Verlag 52425 Jülich Tel.: +49 2461 61-5368 Fax: +49 2461 61-6103 zb-publikation@fz-juelich.de www.fz-juelich.de/zb
Umschlaggestaltung:	Grafische Medien, Forschungszentrum Jülich GmbH
Druck:	Grafische Medien, Forschungszentrum Jülich GmbH
Copyright:	Forschungszentrum Jülich 2021

Schriften des Forschungszentrums Jülich
Reihe Energie & Umwelt / Energy & Environment, Band / Volume 530

D 464 (Diss. Duisburg, Univ., 2020)

ISSN 1866-1793
ISBN 978-3-95806-528-4

Vollständig frei verfügbar über das Publikationsportal des Forschungszentrums Jülich (JuSER)
unter www.fz-juelich.de/zb/openaccess.

Contents

Acknowledgments

First of all, I would like to thank my advisor Prof. Dr. Kirchartz for giving me the opportunity to discover the fascinating world of organic photovoltaics and for guiding and supporting me during this incredible journey.

I am grateful to Benedikt for the always useful discussions and to Alberto for teaching me how to fabricate organic solar cells and the delightful conversations we had in Spanish. They both made the office and the lab a comfortable and very enjoyable place to work in. Moreover, a thanks goes to all the students who worked in our research group and gave me the chance to prove myself as a supervisor.

I would like to thank Luca and Davide for sharing our different, and yet so similar, PhD experiences. Together with Elisa and Audrey they have been a big part of my "Bochum life" and made these years unforgettable.

A big thank you goes to my parents, my brother, and my sister who never stopped believing in me and having my back under any circumstances.

Finally, my deepest thanks to Francesco for being the perfect complement to my life, for always being on my side, and for showing me the light even in the darkest moments. I would never have reached this goal without him.

Abstract

In the last decades, organic photovoltaics has emerged as a promising environment-friendly and low-cost technology for the production of energy. Even though the efficiency of organic solar cells has increased rapidly during the last years, further improvements in terms of device lifetime and performance are still needed for a successful commercialization of such solar cells.

In this work, two important processes affecting the efficiency of organic solar cells, namely the recombination and the transport of charge carriers, are investigated. Solution-processed solar cells based on different polymer:fullerene systems are studied by using impedance-based techniques, specifically capacitance-voltage and capacitance-frequency measurements, in combination with steady state current-voltage measurements and numerical simulations.

In the first step, current-voltage measurements and drift-diffusion simulations are used together to develop a method to discriminate between surface and bulk recombination in organic solar cells. The application of the method to a range of current-voltage data of organic solar cells based on different polymer:fullerene systems and with diverse architectures confirms the validity of the method and shows the possibility to observe the whole range of cases, from mostly surface limited to purely bulk limited recombination, in the field of organic photovoltaics.

After the steady-state analysis, the focus of this work shifts to the investigation of organic solar cells via frequency-resolved methods, such as capacitance-voltage measurements. The features observed in capacitance-voltage measurements performed on fully depleted organic solar cells under illumination are explained with a combination of the photogenerated space charge in the device and the charge-carrier mobility, whose value

can thus be extracted from such measurements. Then, the analysis of the capacitance of a partially depleted device under illumination and short-circuit conditions is addressed. The discussion of three analytical models for the determination of the charge-density in the neutral region of such devices and the introduction of the relation between charge density, capacitance under illumination, and charge-carrier lifetime permit to highlight the possibility of extracting the lifetime value from capacitance data at short circuit. Furthermore, the crucial influence of sample properties and measurement conditions on the applicability of methods to analyze capacitance-voltage data is highlighted and emphasized.

Finally, an analysis of capacitance-frequency measurements on organic solar cells under illumination is presented. The possibility to approximate the charge density present in the active layer of such devices under reverse bias with the density of photo-generated charge carriers derived from capacitance-frequency data is first verified and then used to identify the dominant recombination mechanism and to determine either the charge-carrier lifetime or the bimolecular recombination coefficient.

Zusammenfassung

In den letzten Jahrzehnten hat sich die organische Photovoltaik als potentielle umweltfreundliche und billige Technologie für die Energieversorgung herausgestellt. Obwohl die Effizienz der organischen Solarzellen in den letzten Jahren rapide zugenommen hat, sind weitere Verbesserungen bezüglich der Lebensdauer und der Leistung dieser Bauelemente für eine erfolgreiche Kommerzialisierung solcher Solarzellen noch notwendig.

Diese Arbeit erforscht die Rekombination und den Transport von Ladungsträgern, d.h. zwei wichtige Prozesse, die die Effizienz der organischen Solarzellen beeinflussen. Lösungsprozessierte Solarzellen basierend auf verschiedenen Polymer:Fulleren Systemen werden durch eine Kombination von Impedanz-basierten Methoden, stationären Strom-Spannungs-Messungen und numerischen Simulationen untersucht.

Im ersten Schritt wird eine durch Strom-Spannungs-Messungen und Drift-Diffusion Simulationen entwickelte Methode für die Unterscheidung zwischen Oberflächenrekombination und Volumenrekombination vorgestellt. Die Anwendung dieser Methode auf Strom-Spannung-Daten von organischen Solarzellen basierend auf verschiedenen Polymer:Fulleren Systemen mit unterschiedlichen Kontaktschichten bestätigt ihre Anwendbarkeit und zeigt, dass in der organischen Photovoltaik das ganze Spektrum, von meist oberflächenlimitierte bis voll bulklimitierte Rekombination, zu beobachten ist.

Nachdem die erste Methode stationäre Messungen von Strom und Spannung der Solarzelle zur Extraktion von Parametern nutzt, konzentriert diese Arbeit sich auf die Untersuchung der organischen Solarzellen mittels frequenzaufgelöster Methoden, wie zum Beispiel Kapazität-Spannungs-Messungen. Die Eigenschaften der an beleuchten und komplett verarmten Solarzellen durchgeführten Kapazität-Spannung-Messungen werden durch eine Kombination von photogenerierter Raumladung und Ladungsträgerbe-

weglichkeit erklärt und die Ermittlung der Ladungsträgerbeweglichkeit von Kapazität-Spannungs-Daten wird präsentiert. Danach wird die Kurzschlusskapazität von teilweise verarmten Solarzellen unter Beleuchtung untersucht. Die Darstellung von drei analytischen Modellen für die Bestimmung der Ladungsträgerdichte in der neutralen Zone solcher Solarzellen und die Vorstellung des Zusammenhangs zwischen Ladungsträgerdichte, Kapazität unter Beleuchtung und Ladungsträgerlebensdauer zeigen die Möglichkeit, die Lebensdauer aus der Kurzschlusskapazität zu ermitteln. Außerdem wird der entscheidende Einfluss von Probeneigenschaften und Messbedingungen auf die Anwendbarkeit der Analysemethoden für Kapazität-Spannungs-Daten hervorgehoben und betont.

Abschließend wird eine Analyse der Kapazität-Frequenz-Messungen an organischen Solarzellen unter Beleuchtung vorgestellt. Die Annäherung der Ladungsträgerdichte in der aktiven Schicht solcher Solarzellen unter negative Spannung mit der Dichte von photogenerierten Ladungsträgern ermöglicht die Identifizierung der dominierenden Rekombinationsmechanismus und die Bestimmung von entweder der Ladungsträgerlebensdauer oder des bimolekularen Rekombinationskoeffizients.

Chapter 1

Introduction

In the last years, the continuous increase of energy demand, prompted by the fast growth of world population, has highlighted the urgent need for a nonpolluting, affordable, and sustainable energy supply. Traditional fossil energy resources, such as coal and oil, have been exploited for decades without considering the consequences of atmosphere pollution, but are now unable to satisfy the growing demand of energy without significantly spoiling the earth environment. Renewable energies, with their potential to help solving this important problem, have been attracted a strongly increasing attention during the last years. In 2008 the European Union (EU) adopted its first package of climate and energy measures which fixed the target of a 20% reduction of greenhouse gas emissions and a 20% share of energy from renewable sources by 2020 [1]. Few years later, in 2014, a new and more ambitious renewable energy target of at least 27% of EU's final energy consumption by 2030 was decided by EU countries [2]. The achievement of these ambitious targets relies on the further development of renewable energy sources, as well as the optimization of the energy storage system and the reorganization of the electricity grid.

Besides wind energy, hydroelectric energy, and biomass, another promising environment-friendly energy source is the photovoltaic energy which in the last decades has assumed a significant role in the renewable energy production. For example, in 2017 solar systems generated around 39 billion kilowatt hours electricity in Germany [3] and 24 billion kilowatt hours in Italy [4]. This energy production derives from the conversion of the solar irradiation into electrical energy by means of photovoltaic devices which exploit the photovoltaic effect. The latter describes the ability of a semiconductor

material to convert electromagnetic radiation, like the solar radiation, into electric power and was first observed by Becquerel in 1839 [5]. However, it was only in 1954 that, thanks to the discovery of a way to manufacture silicon *p*-*n* junction structures, a silicon solar cell with a power conversion efficiency (PCE) of about 6% was realized by D. Chapin, C. S. Fuller and G. Pearson at the Bell Laboratories [6]. In the following decades the efficiency of these monocrystalline *p*-*n* junctions strongly increased and, with its actual value of 26.7% [7], has almost reached the theoretical limit of about 30% calculated by W. Shockley and H.J. Queisser [8] for a single layer silicon solar cell. Nevertheless, the laborious, costly, and energy consuming processing of silicon wafers for the production of conventional silicon solar cells has encouraged the development of inorganic thin-film technologies, like copper indium gallium selenide (CIGS) or cadmium telluride (CdTe) solar cells. Despite the higher absorption coefficient of the materials used in these devices and the consequent smaller amount of needed material, the mass production of these solar cells is hindered by the use of rare elements like indium and gallium which are essential for obtaining high device efficiencies.

A completely new approach for the realization of cheap solar cells arose after the discovery of conductive polymers by H. Shirakawa, A. MacDiarmid and A. J. Heeger [9]. Industrial and scientific research around this younger and innovative technology based on the use of organic semiconductors has quickly grown in the last two decades thanks to the potential use of flexible cheap substrates and the promise of easy upscaling and low-temperature mass production. In fact, semiconducting polymers employed in organic solar cells are typically soluble in standard organic solvents, like chlorobenzene, and can therefore be deposited via spin coating, doctor blading, or mass printing techniques, such as roll-to-roll printing [10, 11]. Moreover, the high absorption coefficient of organic materials implies a reduced amount of needed material and the consequent possibility to fabricate light thin-film devices for innovative, mobile applications [12] or semitransparent solar cells for building integration [13]. Despite these numerous potential advantages and power conversion efficiencies that recently reached 16% [14–16], there are still important issues that have to be tackled in order to achieve a successful commercialization of organic solar cells. Beside the improvement of the stability in terms of cell degradation and the extension of the device lifetime, a complete understanding of the working principles and the physics of organic solar cells is essential for the further development of this technology.

One of the most central and highly relevant topics in the field of organic photovoltaics is the identification and quantification of the kinetics of charge-carrier recombination and transport processes [17–20]. Among the most widely used techniques to study charge transport and recombination in solar cells are frequency-resolved methods that analyze the response of a device to a periodic, most frequently electrical, excitation. The impedance or admittance of a solar cell can be studied as a function of frequency [21,22], temperature [23,24], DC bias voltage [25,26], and sometimes also AC voltage amplitude [27,28]. The capacitance, which may be derived from the imaginary part of the admittance, is sensitive to the density of charge carriers and, depending on the range of bias voltages and illumination conditions, may yield the doping density of the solar cell absorber layer or the optically or electrically injected charge-carrier density. From the frequency and temperature dependence of the capacitance one may also derive the density and kinetics of localized states [29,30], if certain conditions are met. While the variation of measurement conditions allows admittance-based characterization techniques to be sensitive to a plethora of information, access to this information requires the development of, often quite sophisticated, analysis methods. This is certainly true for frequency and temperature dependent variations of admittance spectroscopy, but also for the simplest variant, namely the measurement of the capacitance as a function of DC voltage and under different illumination conditions. The classic application of capacitance-voltage measurements is the determination of the doping concentration from the space-charge capacitance [31]. In order to avoid misinterpretation, this measurement has to be done at reverse bias and in the dark and it works if the absorber layer is only partially depleted [32], i.e. if the width w of the space-charge region is smaller than the absorber thickness d over a sufficient voltage range. Under forward bias, the chemical capacitance of the optically and electrically injected charges will at some point dominate the space-charge capacitance [33] and the measurement of the capacitance will become sensitive to the density of states. Even though the different measurement conditions of a capacitance-voltage measurement in the dark are by now mostly understood, the analysis of capacitance-voltage measurements under illumination on devices fully or partially depleted (conditions highlighted in Table 1.1) has so far been mostly neglected in the literature. The present work attempts to fill this gap presenting new methods to analyze capacitance-voltage and capacitance-frequency measurements performed under illumination on bulk heterojunction solar cells. Experi-

mental data, numerical simulations and analytical equations are in this work considered together in order to achieve a coherent picture of the mechanisms affecting capacitance-voltage measurements under illumination and to identify a model-free method for the determination of recombination parameters from capacitance-frequency measurements under illumination.

Table 1.1: Information accessible through the analysis of capacitance-voltage data depending on the measurement conditions and the sample properties.

	$w < d$	$w \approx d$
DARK	at $V \leq 0$ space-charge capacitance provides the doping density	at $V > 0$ chemical capacitance related to the density of states
LIGHT	at $V = 0$ to be discussed in this work	at $V \leq 0$ to be discussed in this work

This thesis is divided into two main parts, with the initial chapters focusing on the theoretical background and the last chapters containing the experimental results obtained investigating charge transport and recombination with a combination of numerical simulations and steady-state or frequency-resolved techniques. After giving a general overview on organic semiconductors and organic solar cell structures, the device working principle and basic device physics are discussed. Then, the main recombination mechanisms are presented, followed by the description of the device fabrication procedure and the introduction of the organic materials, the experimental techniques, and the simulation tools used in this work. The second part of the thesis presents first a study of charge-carrier recombination via steady-state measurements, specifically current-voltage measurements, which led to a method to discriminate between bulk and surface recombination in organic solar cells. Subsequently, capacitance-voltage measurements under illumination on devices fully and partly depleted are examined and the big influence of sample properties and measurement conditions on the applicability of methods to analyze capacitance-voltage data is highlighted. Finally, capacitance-frequency measurements under illumination are addressed and the possibility to extract the charge-carrier density and recombination parameters from such measurements is verified.

Chapter 2

Organic Photovoltaics

This chapter provides a basic introduction to organic semiconductors and their application in organic photovoltaics. It also presents and discusses the different structures, the working principles, and the basic physics of organic solar cells and it is finalized by a section on the solar cell characteristics.

2.1 Organic Semiconductors

The basis of the semiconducting behavior in organic compounds is the presence of carbon atoms with π-conjugated bonds which allow a delocalization of electrons. In its ground state the carbon atom has the configuration $1s^2 2s^2 2p^2$ and four valence electrons. When two carbon atoms interact, one $2s$ and two of the $2p$ orbitals can form three sp^2 hybrid orbitals leaving one p_z orbital perpendicular to the plain of the sp^2 orbitals. This hybridization permits neighboring carbon atoms to constitute three coplanar σ-bonds arranged at an angle of 120° and one perpendicular π-bond. The σ-bonds characterized by strongly bound electrons shape the backbone of the molecule, whereas the p_z orbital, overlapping with a p_z orbital of a neighbor carbon atom, forms the π-conjugated bond with electrons weakly bound that tend to be delocalized. The interaction of several carbon atoms leads to the splitting of the p_z orbitals into multiple binding and anti-biding orbitals, slightly shifted in energy. If the number of carbon atoms further increases, two energy bands are formed, as shown in Fig. 2.1. The band lower in energy is called highest occupied molecular orbital (HOMO), has binding character, and is populated, while the band higher in energy is named lowest unoccupied

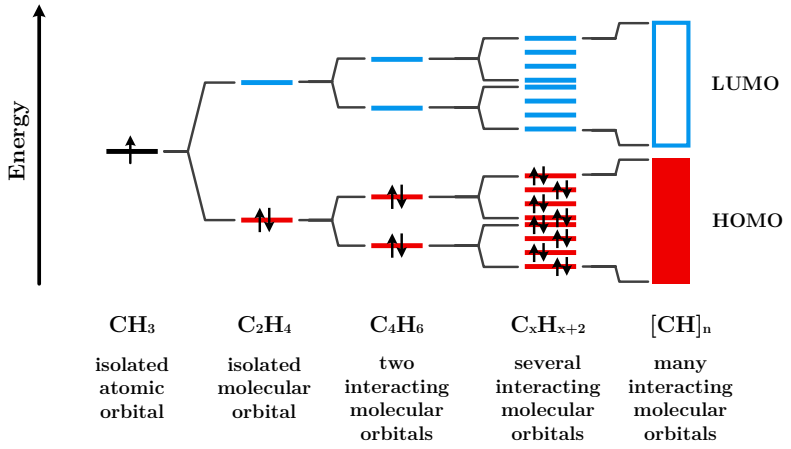

Figure 2.1: Formation of the energy bands in semiconducting polymers [34]. The increasing number of interacting carbon atoms results in a transition from a single carbon with three sp^2 hybrid orbitals and one p_z orbital to a conjugated polymer with alternating single-double bonds and two energy bands separated by an energy gap.

molecular orbital (LUMO), has anti-binding character, and is unoccupied. HOMO and LUMO represent for organic semiconductors what the valence and conduction band are for inorganic semiconductors. The separation of HOMO and LUMO constitutes in fact the energy gap needed for the occurrence of the semiconducting character. The energy gap is typically in the range of 1-3 eV [35] and is thus accessible by visible light. Its origin can be assigned to the Peierls distortion [36,37], which accounts for the slightly varying distances between neighboring carbon atoms. The alternation of single and double bonds between carbon atoms, together with the conjugation, is therefore an essential requirement for the realization of molecules and polymers with semiconducting properties.

2.2 Organic Solar Cell Structures

The most basic structure of an organic solar cell is displayed in Fig. 2.2(a) and is composed by an organic semiconductor sandwiched between two metal electrodes, one of whom being transparent [38]. For this single layer solar cell the conversion of light

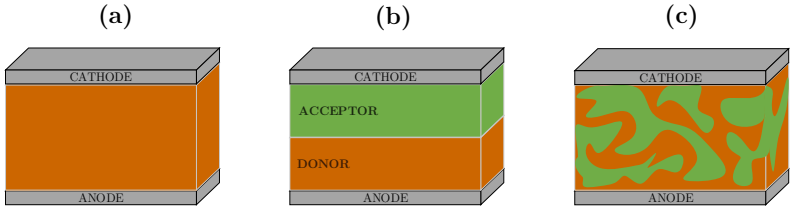

Figure 2.2: Structure of single layer (a), single junction (b), and bulk heterojunction (c) solar cells. The single layer solar cell is composed by a single semiconductor sandwiched between two electrodes, whereas a single junction consists of adjacent acceptor and donor layers. A bulk heterojunction solar cell contains an active layer composed by a donor-acceptor blend.

into electricity starts with the absorption of the light by the organic semiconductor and the consequent generation of strongly bound electron-hole pairs called excitons [39,40]. This strongly bound excitons are localized on a single molecule or a single conjugated segment and, due to the low dielectric constants of organic compounds ($\varepsilon_r \approx 3-4$ [35]), hardly dissociate into free charges. The Coulomb energy binding these localized charges is in fact high (~ 1 eV) compared to the thermal energy and, consequently, the charge generation process in single layer solar cells is very poor. To enhance exciton dissociation, a single junction solar cell as the one presented in Fig. 2.2(b) can be used [41]. The intrinsic difficulties of exciton dissociation are here reduced by introducing a second semiconductor with an higher affinity for electrons. Hence, in this type of solar cells the absorber layer, also called active layer, is formed by two organic semiconducting materials with different electron affinities (EA) deposited one after the other. The material with lower EA is called electron donor and the material with higher EA is denoted as electron acceptor. In this architecture, once the light is absorbed and the exciton is generated, the latter diffuses to the donor-acceptor interface where the energy offset drives its dissociation into an electron and a hole. Thanks to the higher EA, the electron moves to the acceptor and travels to the cathode. On the other hand, the hole remains in the donor and proceeds towards the anode. However, the small exciton diffusion length ($\sim$10 nm) [42–44] and the restricted donor-acceptor interface area still limit the efficiency of this type of solar cells. These limits are mitigated by blending the two semiconductors to form an interpenetrating and bicontinuous network of separated donor-rich and acceptor-rich domains (Fig. 2.2(c)). Such a structure is called

bulk heterojunction (BHJ) and, providing a larger interfacial area, further facilitates the exciton dissociation. In BHJ solar cells the absorber layer is often considered a single effective semiconductor with the LUMO of the electron acceptor and the HOMO of the electron donor [45,46]. A bulk heterojunction solar cell can be realized using two possible configurations [47]. The first possibility, denoted as superstrate configuration, is the most used and allows the light to enter the device through a transparent superstrate on which the front electrode and subsequently the device are built. In the second possible configuration, referred to as substrate configuration, all solar cell layers are deposited on top of a substrate which can also be opaque since the illumination of the device occurs through the front contact. Figure 2.3 shows the schematic illustrations of a BHJ solar cell with a standard and inverted structure, both in superstrate configuration. In the former, the transparent electrode, usually Indium Tin Oxide (ITO), acts as hole collecting electrode and a metal with low workfunction, such aluminum, is used as electron collecting electrode. However, in the presence of moisture, these low workfunction metals are quite sensitive to oxidation. This limitation is partially overcome using an inverted structure, in which the electron collecting electrode is the semitransparent electrode and a high workfunction metal, like silver or gold, acts as hole collecting electrode.

All the devices used in this study are bulk heterojunction solar cells with an inverted structure in superstrate configuration.

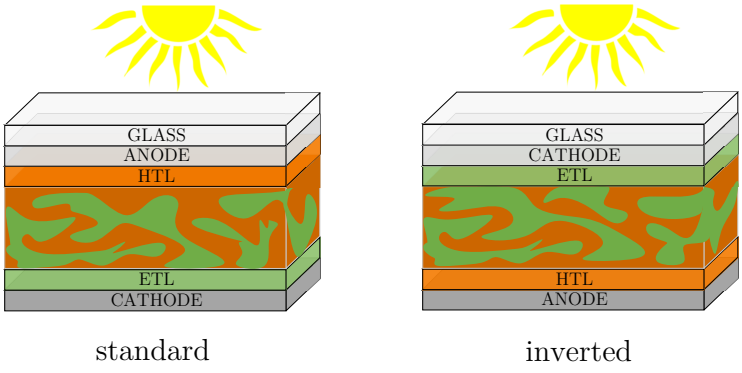

Figure 2.3: Device structure of a bulk heterojunction solar cell with standard and inverted architecture in superstrate configuration.

2.3 Organic Solar Cell Operating Principles

As illustrated in Fig. 2.4, the operation of a bulk heterojunction solar cell relies on four main physical processes:

1. Absorption of the light within the active layer and exciton formation;
2. Exciton diffusion and dissociation;
3. Charge-carrier transport;
4. Charge-carrier extraction at the contacts.

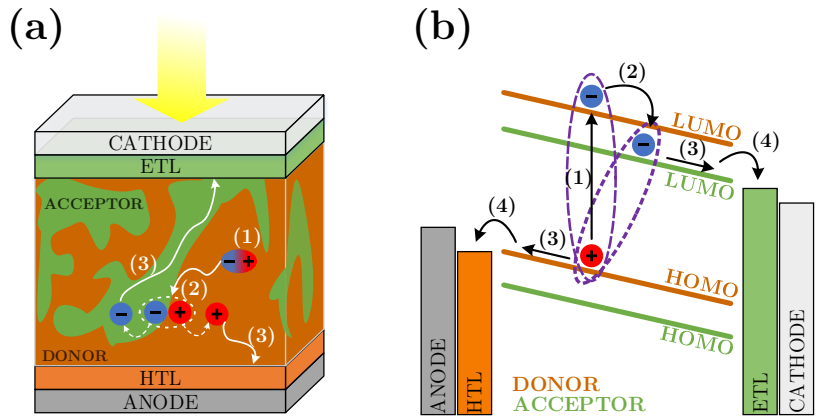

Figure 2.4: Device structure (a) and energy-band diagram (b) depicting the four crucial physical processes of an organic solar cell: (1) light absorption and exciton generation, (2) exciton diffusion to the donor-acceptor interface and exciton dissociation, (3) free charge-carrier transport to the electrodes, (4) charge extraction at the contacts with the help of interlayers.

2.3.1 Photon Absorption and Exciton Generation

The conversion of solar light into electricity in an organic solar cell starts with the absorption of photons by the materials composing the active layer. The absorption

coefficient of organic compounds is usually high and therefore, in principle, both constituents of the active layer, the donor and the acceptor, can absorb the incident light. However, the conjugated polymers mostly used as donor materials have higher absorption coefficient than fullerene derivatives applied as acceptors [48] and, consequently, the former act as principal light absorber. Thanks to the high absorption coefficients, an active layer which is few hundred nanometers thick already absorbs an adequate amount of light and can provide reasonable solar cell characteristics [49]. The photoexcitation of the active-layer materials, differently from what happens in an inorganic semiconductor, results in the generation of electrically neutral and strongly bound excited states called excitons. The existence of these bound excitons prior to the generation of free charge carriers represents one main difference between the charge generation in organic and inorganic solar cells. As already mentioned, due to the low dielectric constants of the organic semiconductors, the exciton binding energies are much higher than the thermal energy $k_{\mathrm{B}}T$ [50, 51]. Under these conditions, the internal electric field is not high enough to allow charge pairs to be generated spontaneously and efficiently at room temperature. Thus, an intermediate step via a less strongly bound electron-hole pair is needed. In order for this step to take place, the excitons have to diffuse to the interface between donor and acceptor.

2.3.2 Exciton Diffusion and Dissociation

In order to be dissociated, the excitons need to travel to the donor-acceptor interface. The distance they can diffuse before they recombine is called exciton diffusion length and in organic materials is in the order of a few tens of nanometers [48, 51]. Excitons which are generated at a distance from the donor-acceptor interface longer than this diffusion length will recombine before dissociating. Hence, the ideal active-layer blend is obtained when the maximum distance to the next donor-acceptor interface does not exceed the exciton diffusion length. When an exciton reaches an interface between donor and acceptor materials, the electron is transferred from the donor to the acceptor, due to the higher electron affinity of the latter, whereas the hole remains in the donor. This charge transfer occurs only if it is energetically favorable, i.e. if the energy offset between the donor and acceptor LUMO levels is greater than the exciton binding energy or, in other words, if the difference in free energies between the exciton and the charge separated state overcomes the lost exciton binding energy [35, 42]. Once the exciton

is dissociated, the charges are still linked by Coulombic forces despite being physically separated and residing on different molecules, the electron on an acceptor molecule and the hole on a donor molecule. However, their binding energy is now substantially tinier and, therefore, a total charge separation by internal/external electric field becomes possible. This intermediary bound state with still Coulombically linked charges which are physically separated at the interface between donor and acceptor is called charge transfer (CT) state.

2.3.3 Charge-Carrier Transport

After a successful exciton dissociation, the separated electron and hole are transported to the corresponding electrodes inside the acceptor- and donor-phase, respectively. Unlike in inorganic semiconductors where the three dimensional periodic lattice structure allows the electron wave function to delocalize over the entire crystal, the charge transport in organic semiconductors is characterized by the disordered nature of the materials and the lack of long range order. The delocalization just over single molecules or conjugated polymer segments obliges charge carriers to be transported by hopping from one localized state to another [52–54]. In order to describe in general the charge transport properties of the active-layer materials the charge-carrier mobility μ is used. The latter is defined as the proportionality constant between the carrier drift velocity ν_d and the electric field F [48, 55]

$$\nu_\mathrm{d} = \mu F. \tag{2.1}$$

For most organic semiconductors the charge-carrier mobility is relatively low, lying between 10^{-4} and 10^{-3} $\mathrm{cm}^2/\mathrm{Vs}$ [40, 52]. The carriers of opposite charge, on their way towards the respective electrodes, may also meet each other and annihilate. This loss mechanism, named nongeminate recombination, can have severe impact on the device performance and will be discussed in detail in section 3.2.

In order to reach an effective charge-carrier transport to the respective electrodes, uninterrupted percolation paths are needed in the active layer [42,56]. Thus, the search for the perfect morphology, able to maximize the efficiency of a bulk heterojunction solar cell, is an interplay between two opposing prerequisites: well intermixed donor-acceptor phases necessary for efficient exciton dissociation and extended phases and percolation paths essential for charge transport.

2.3.4 Charge-Carrier Extraction

If there are continuous pathways to the electrodes and the charge carriers are not lost due to nongeminate recombination processes, they can be finally extracted at their respective electrodes and released into an external circuit. To guide the charge carriers to the corresponding electrode and hinder the drift towards the 'wrong' electrode, interfacial layers are usually introduced between the organic absorber layer and the electrodes. More specifically, a hole extracting layer, also referred to as hole transport layer (HTL), is adopted at the anode and an electron extracting layer, also named electron transport layer (ETL), is employed at the cathode. These thin interlayers add selectivity to the relevant carriers at the contacts and help reducing the extraction barrier facilitating to obtain quasi-ohmic contacts [57] and an efficient charge extraction [58]. Besides selectively collecting electrons and holes, the electrodes also define the built-in potential V_{bi}, which is given by the difference between the work functions of the cathode and the anode [59, 60].

2.4 Device Physics

Despite the differences in terms of charge-carrier photogeneration and transport, the physics of organic and inorganic solar cells follows the same fundamental principles. In the following the terminology commonly applied to inorganic semiconductors is therefore used to briefly present the physics at the basis of the function of organic devices.

In the active layer of a bulk heterojunction solar cell the electrostatic potential due to charge carriers obeys Poisson's equation [61]

$$\nabla^2 \Phi = -\frac{\rho}{\varepsilon_0 \varepsilon_{\mathrm{r}}}, \tag{2.2}$$

with Φ being the electrostatic potential, ε_0 the dielectric permittivity of the vacuum, ε_{r} the relative permittivity of the active layer, and ρ the space charge which results from both mobile and fixed charges. The distinction between fixed and mobile charges is crucial within the analysis of *p*-*n* junctions, where two electrically different regions, namely the space-charge region and the neutral region, can be identified. When a *n*-doped and a *p*-doped semiconductors are brought into contact, the free electrons diffuse from the *n*-type material into the *p*-type material and the free holes diffuse from

the p-type material into the n-type material. The result of this diffusion process is the depletion of free charge carriers in the region around the junction interface and the build-up of negative charge in the p-doped semiconductor and of positive charge in the n-doped semiconductor. The electrostatic potential originating from the build-up of space charges makes it then increasingly harder for both electrons and holes to diffuse across the junction and eventually an equilibrium between diffusion effects and electrostatic forces is reached. This thermal equilibrium state, characterized by the equalizing of the Fermi levels of the two semiconductors, determines the final dimensions of the region depleted of free charge carriers, i.e. the width of the space-charge region. Since the space-charge region is the region around the junction interface that gets depleted of free charge carriers, it is also referred to as depletion region. The space-charge region features an electric field different from zero and is usually considered to contain just fixed ionized doping atoms, whereas the neutral region, i.e. the region far from the junction interface, is field-free and contains mobile charge carriers. By separating the contribution of mobile and fixed charge, the Poisson's equation can be rewritten as

$$\nabla^2\Phi = \frac{q}{\varepsilon_0\varepsilon_\mathrm{r}}\left(-\rho_\mathrm{fixed} + n - p\right), \tag{2.3}$$

where ρ_fixed is the local density of fixed charges, and n and p are the free electron and hole densities, respectively. The principle of the conservation of charges is expressed by the continuity equations for electrons and holes

$$\frac{\mathrm{d}n}{\mathrm{d}t} = \frac{1}{q}\frac{\mathrm{d}J_\mathrm{n}}{\mathrm{d}x} + G - R \tag{2.4}$$

$$\frac{\mathrm{d}p}{\mathrm{d}t} = -\frac{1}{q}\frac{\mathrm{d}J_\mathrm{p}}{\mathrm{d}x} + G - R, \tag{2.5}$$

with q being the elementary charge, and G and R the generation and the recombination rates. J_n and J_p are the electron and hole current densities which can be articulated as

$$J_\mathrm{n} = qn\mu_\mathrm{n}F + qD_\mathrm{n}\frac{\mathrm{d}n}{\mathrm{d}x} \tag{2.6}$$

$$J_\mathrm{p} = qp\mu_\mathrm{p}F - qD_\mathrm{p}\frac{\mathrm{d}p}{\mathrm{d}x}. \tag{2.7}$$

Here μ_n and μ_p are the electron and hole mobilities, F is the electric field, and D_n

and D_p are the diffusion coefficients of electrons and holes given by Einstein's relation: $D_{\mathrm{n/p}} = \mu_{\mathrm{n/p}} \frac{k_\mathrm{B} T}{q}$. The diffusion coefficients are also related to the diffusion length which is a measure of the distance a minority charge carrier will travel on average before recombining. According to Eqs. (2.6) and (2.7), the current densities can possess a diffusion component and a drift component whose relevance depends on the net electric field within the active layer. The combination of the current equations with the continuity equations under steady-state condition results in the transport equations for electrons and holes

$$D_\mathrm{n} \frac{\mathrm{d}^2 n}{\mathrm{d}x^2} + \mu_\mathrm{n} F \frac{\mathrm{d}n}{\mathrm{d}x} + \mu_\mathrm{n} n \frac{\mathrm{d}F}{\mathrm{d}x} + G - R = 0 \tag{2.8}$$

$$D_\mathrm{p} \frac{\mathrm{d}^2 p}{\mathrm{d}x^2} + \mu_\mathrm{p} F \frac{\mathrm{d}p}{\mathrm{d}x} + \mu_\mathrm{p} p \frac{\mathrm{d}F}{\mathrm{d}x} + G - R = 0. \tag{2.9}$$

Under thermal equilibrium conditions, the most stable energetic distribution of electrons in a semiconducting material is described by the Fermi-Dirac statistics and the average probability of electron occupation at a energy level E is given by the Fermi-Dirac distribution function f_0 [61]

$$f_0\left(E, E_\mathrm{F}, T\right) = \frac{1}{1 + e^{\frac{(E - E_\mathrm{F})}{k_\mathrm{B} T}}}. \tag{2.10}$$

Here E_F is the Fermi energy, T is the temperature in K, and k_B is the Boltzmann's constant. Knowing the density of electronic states as function of energy $g_\mathrm{c}(E)$, the electron density in a conduction band with minimum energy E_c can be calculated by

$$n = \int_{E_\mathrm{c}}^{\infty} g_\mathrm{c}(E) f_0\left(E, E_\mathrm{F}, T\right) \mathrm{d}E. \tag{2.11}$$

Analogously, once the density of states as function of energy $g_\mathrm{v}(E)$ in a valence band with maximum energy E_v is known, the density of holes is given by

$$p = \int_{-\infty}^{E_\mathrm{v}} g_\mathrm{v}(E) \left(1 - f_0\left(E, E_\mathrm{F}, T\right)\right) \mathrm{d}E. \tag{2.12}$$

If the Fermi energy is far enough from both band edges, e.g. in thermal equilibrium,

the integrals in Eqs. (2.11) and (2.12) simplify and the electron and hole densities can be expressed as [62]

$$n = N_{\mathrm{c}} e^{\left(\frac{E_{\mathrm{F}} - E_{\mathrm{c}}}{k_{\mathrm{B}} T}\right)} \tag{2.13}$$

$$p = N_{\mathrm{v}} e^{\left(\frac{E_{\mathrm{v}} - E_{\mathrm{F}}}{k_{\mathrm{B}} T}\right)}, \tag{2.14}$$

where N_{c} and N_{v} are the effective densities of states of the conduction and valence band, respectively. According to Eqs. (2.13) and (2.14), the electron and hole densities vary exponentially with the position of the Fermi level inside the bandgap and their product is constant at a given temperature. This constant value defines the intrinsic carrier density n_{i}

$$n_{\mathrm{i}}^2 = np = N_{\mathrm{c}} N_{\mathrm{v}} e^{-\frac{E_{\mathrm{g}}}{k_{\mathrm{B}} T}} \tag{2.15}$$

which is equal to the density of electrons thermally excited in the conduction band of a semiconductor in thermal equilibrium. Here, the energy gap E_{g} is given by the difference between the minimum energy of the conduction band and the maximum energy of the valence band: $E_{\mathrm{g}} = E_{\mathrm{c}} - E_{\mathrm{v}}$. When the system is disturbed from equilibrium by illumination or by the application of an external bias, the population of electrons and holes changes and thus can no longer be described by the Fermi-Dirac distribution function f_0. However, if the disturbance is not too big, the charge carriers will relax within their bands to achieve a state of quasi-thermal equilibrium. The definition of quasi-thermal equilibrium is possible because the charge carriers relax within the bands much faster than between the bands. This allows each band to be at local equilibrium and have its own separate Fermi level. Hence, a splitting of the Fermi levels arises and its size depends on the entity of the disturbance. The separate Fermi levels $E_{\mathrm{F_n}}$ and $E_{\mathrm{F_p}}$, for electrons and holes respectively, are called quasi-Fermi levels. Assuming quasi-thermal equilibrium, the electron and hole densities can be expressed by substituting the unique Fermi level E_{F} in Eqs. (2.13) and (2.14) with the two quasi-Fermi levels $E_{\mathrm{F_n}}$ and $E_{\mathrm{F_p}}$

$$n = N_{\mathrm{c}} e^{\left(\frac{E_{\mathrm{F_n}} - E_{\mathrm{c}}}{k_{\mathrm{B}} T}\right)} \tag{2.16}$$

$$p = N_{\mathrm{v}} e^{\left(\frac{E_{\mathrm{v}} - E_{\mathrm{F_p}}}{k_{\mathrm{B}} T}\right)}. \tag{2.17}$$

The splitting of the quasi-Fermi levels measured at the contacts at open circuit, i.e. the difference of the electrochemical potential at the electron and hole contacts, defines the

open-circuit voltage (V_{oc}) measurable from a solar cell under illumination [55, 63]

$$V_{oc} = \frac{1}{q}\left(E_{Fn,c} - E_{Fp,a}\right), \tag{2.18}$$

with $E_{Fn,c}$ being the electron quasi-Fermi level at the cathode and $E_{Fp,a}$ the hole quasi-Fermi level at the anode.

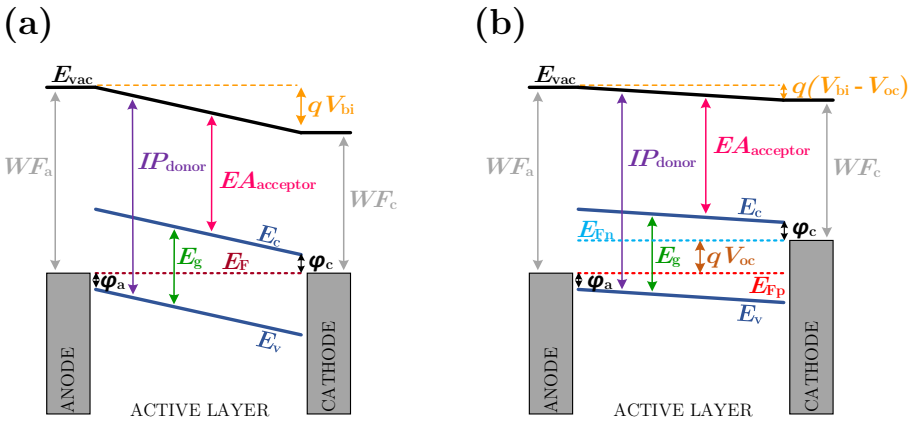

Figure 2.5: Schematic energy-band diagram of a bulk heterojunction solar cell with the active layer sandwiched between two metallic contacts (a) at short circuit in the dark and (b) at open circuit under illumination. The vacuum level E_{vac} is represented together with the contact work functions, the contact barriers φ_a and φ_c at the anode and the cathode, the electron affinity of the acceptor, the ionization potential of the donor, the energy bandgap E_g, the built-in voltage V_{bi}, the open-circuit voltage V_{oc}, and the Fermi levels E_F, E_{F_n}, and E_{F_p}.

Figure 2.5 displays the schematic energy-band diagram at short and open circuit of a bulk heterojunction solar cell with the active layer sandwiched between two metallic contacts. In both diagrams the donor:acceptor blend of the active layer appears as a single effective semiconductor with a conduction band (or LUMO) defined by the electron affinity of the acceptor and a valence band (or HOMO) defined by the ionization potential of the donor. These conduction and valence bands are separated by a bandgap with energy E_g and the potential difference between the front and back contact is determined by the difference between the built-in voltage V_{bi} and the applied voltage V. Depicted in the diagrams are also the work functions of anode and cathode and

the contact barriers φ_a and φ_c derived from the difference between the contact work functions and the conduction and valence band edges at the two contacts. Despite the similarities, there is yet a significant difference between the two diagrams displayed in Fig. 2.5, namely the Fermi level position. At short circuit, i.e. when $V = 0$ V (Fig. 2.5(a)), there is a unique Fermi level E_F in the bandgap, whereas at open circuit (Fig. 2.5(b)) the splitting of the Fermi levels occurs and the two quasi-Fermi levels E_{F_n} and E_{F_p} for electrons and holes arise and define the measurable open-circuit voltage V_{oc}.

2.5 Solar Cell Characteristics

The standard method of assessing the photovoltaic performance of a solar cell is the current-voltage measurement which provides current-voltage (J-V) curves like the ones schematically represented in Fig. 2.6. The measurement performed in the dark delivers a curve in which three regions can be identified [64, 65]. Under reverse bias ($V < 0$) and small forward bias a leakage current flowing through the parallel resistance R_{sh} governs the dark curve; in the ideal case, i.e. when $R_{sh} \to \infty$, this current is very small. Approaching the flat band condition, the injection of charge carriers from the contacts becomes significant and an exponential current increase is observed. Finally, at voltages bigger than V_{bi} the electric field is reversed and the current gets limited by the resistivity of the material constituting the active layer. Thus, the behavior of a solar cell in the dark resembles the behavior of a diode which under forward bias admits much larger current than under reverse bias. When the solar cell is illuminated the photovoltaic effect takes place, the entire curve is shifted towards more negative currents (orange curve in Fig. 2.6), and throughout it some characteristic points can be identified. The current density at zero bias is referred to as short-circuit current density J_{sc} and the voltage at which the current density equals zero is called open-circuit voltage V_{oc}. Moreover, the cell power density reaches a maximum at the maximum power point (MPP) which is identified by a certain voltage V_{mpp} and the corresponding current density J_{mpp}. The fill factor, defined as

$$FF = \frac{J_{mpp} V_{mpp}}{J_{sc} V_{oc}}, \tag{2.19}$$

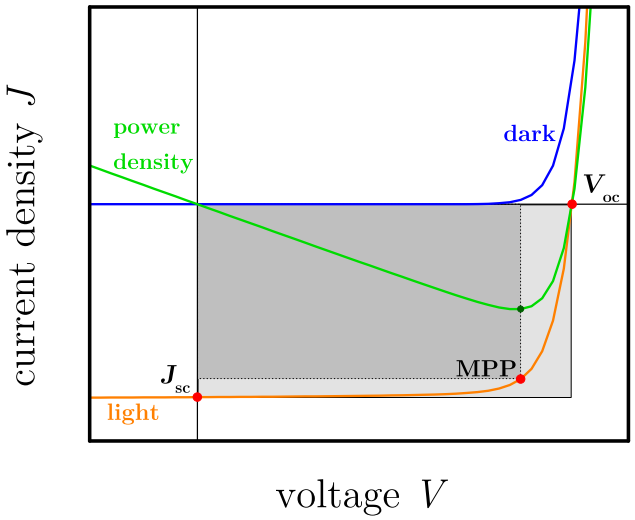

Figure 2.6: Schematic representation of the dark (blue) and light (orange) current-voltage response of a solar cell. The green line represents the output power density whose maximum identifies the maximum power point (MPP) which is marked in red like the short-circuit current density J_{sc} and the open-circuit voltage V_{oc}. The fill factor is defined by the ratio of the areas of the small and big rectangles.

describes the 'squareness' of the current-voltage curve and is represented in Fig. 2.6 by the ratio between the small and the big rectangles. Finally, the solar cell power conversion efficiency η is the ratio between the power generated by the device at the maximum power point and the incident light power P_{light}

$$\eta = \frac{J_{\text{mpp}} V_{\text{mpp}}}{P_{\text{light}}} = \frac{J_{\text{sc}} V_{\text{oc}} FF}{P_{\text{light}}}. \tag{2.20}$$

In order to allow data comparisons among different research groups, these four key performance parameters (J_{sc}, V_{oc}, FF, and η) should be defined under the standard test condition (STC), i.e. Air Mass 1.5 spectrum, incident power density of 1000 W/m^2, and temperature of 25 °C. Other important performance indicators for solar cells are the external and internal quantum efficiencies. The former, together with the incident

light spectrum, determines the value of the short-circuit current via [61]

$$J_{\mathrm{sc}} = q \int \phi(E)\mathrm{EQE}(E)\mathrm{d}E. \tag{2.21}$$

Here $\phi(E)$ is the incident spectral photon flux density and EQE is the external quantum efficiency which defines the probability that an incident photon of a given energy will be converted in an electron collected at the electrodes. Thus, EQE is basically a measure of how efficiently incident photons are converted into usable power and is expressed by the ratio between the number of collected electrons and the number of incident photons of a given energy. The internal quantum efficiency (IQE) is instead the ratio of the number of collected charge carriers to the number of photons of a given energy absorbed by the solar cell.

The operating conditions needed by a solar cell to generate power to an external load are represented in the fourth quadrant of the current-voltage curve in Fig. 2.6, i.e. when the voltage $V \geq 0$ and the current density $J \leq 0$. All the different operating points can be probed by sweeping the voltage from short circuit ($V = 0$) to open circuit ($V = V_{\mathrm{oc}}$). This voltage sweep modifies the net electric field considerably and consequently also the energy-band diagram undergoes big changes. Figure 2.7 schematically displays the configuration of the band diagram at three different operating points in the third and fourth quadrant of a current-voltage curve. At $V < 0$ the high injection barriers for electrons at the anode and for holes at the cathode prevent charge injection from the electrodes and the strong internal electric field allows the complete extraction of the photogenerated charges. At low forward bias the drift component of the current decreases and less charge carriers are extracted. For voltages larger than V_{oc} the electric field changes sign, the energy bands are tilted in the opposite direction, and charges are injected from the electrodes causing a strong current increase.

As already mentioned, a solar cell in the dark behaves like a diode. For an ideal diode the general voltage and temperature dependence of the dark current density J_{dark} is expressed by the Shockley equation [66]

$$J_{\mathrm{dark}}(V) = J_0 \left(e^{\frac{qV}{k_{\mathrm{B}}T}} - 1 \right), \tag{2.22}$$

where J_0 is the saturation current density which can be defined as the recombination current density in thermal equilibrium [67]. According to this definition, the value

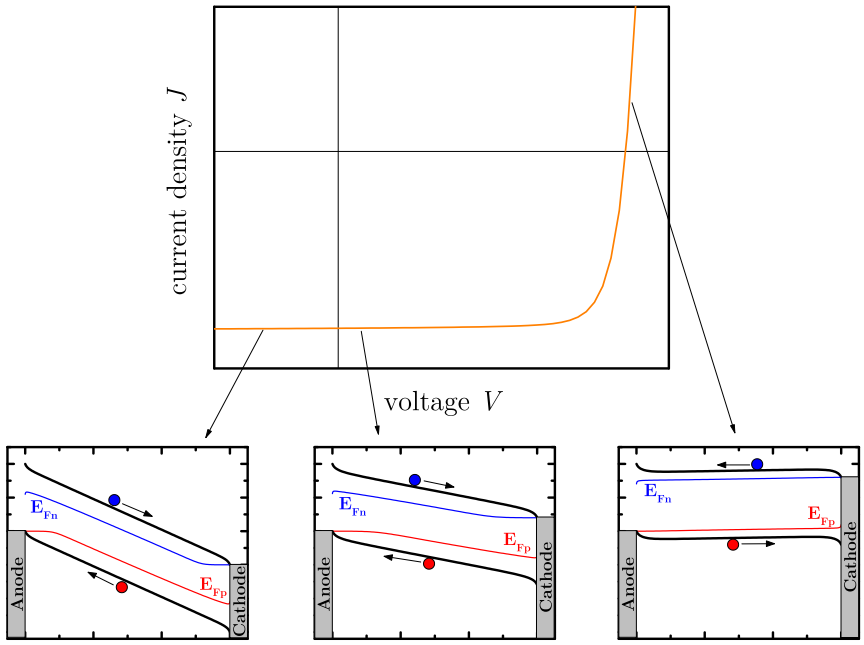

Figure 2.7: Schematic display of the band diagram at three different points on a current-voltage characteristics. Under reverse bias the internal electric field is strong and allows all generated charge carriers to be extracted. At low forward bias the entity of the electric field decreases and less carriers are collected at the electrodes. At voltages greater than V_{oc} a change in the sign of the electric field occurs and a strong charge injection from the contacts takes place.

of the current density J_0 does not depend on external factors like applied voltage or illumination, but is entirely determined by the temperature and the properties of the materials composing the active layer of the solar cell [68]. Since under illumination the current-voltage response of a solar cell can be approximated by superimposing the dark J-V curve and a photogeneration term J_{gen} [65, 69], the expression of the current density becomes

$$J(V) = -J_{gen} + J_0 \left(e^{\frac{qV}{n_{id} k_B T}} - 1 \right). \tag{2.23}$$

Here, the ideality factor n_{id} is introduced to account for the deviations from the ideal diode behavior; its value depends on the recombination mechanism and typically lies

between 1 and 2 [46, 70]. As already mentioned, the potential difference between the electrodes reaches its maximum value, defined as open-circuit voltage, when the dark current equals the short-circuit current, or in other words when the recombination of charges balances the generation of charges. Applying this condition to Eq. (2.23) results in an expression for V_{oc} that highlights its logarithmic dependence on J_{gen} and, therefore, also on the light intensity [71]

$$V_{\mathrm{oc}} = \frac{n_{\mathrm{id}} k_{\mathrm{B}} T}{q} \ln\left(\frac{J_{\mathrm{gen}}}{J_0} + 1\right). \tag{2.24}$$

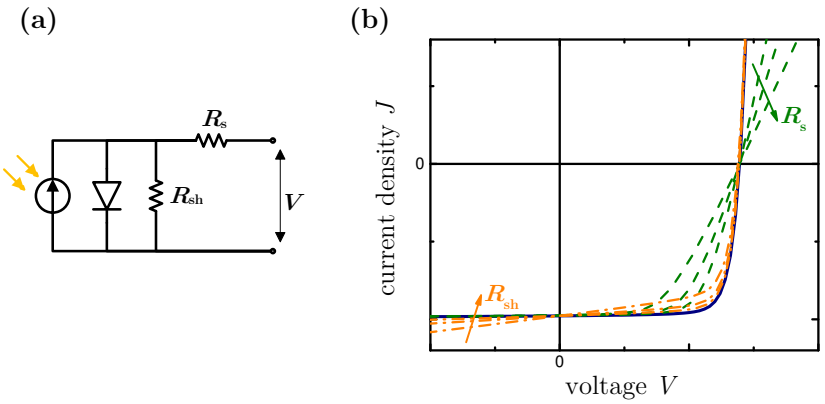

Figure 2.8: (a) Simple equivalent circuit of a real solar cell containing a photocurrent source, a diode, and parallel and series resistances. (b) Influence of parallel resistance R_{sh} and series resistance R_{s} on the current-voltage curve. Both resistances reduce the fill factor.

From the electrical point of view, a solar cell can be modeled with a light-dependent current generator in parallel with a non-linear and asymmetric resistive element, i.e. a diode. To this simple model, a series and a shunt resistor are added to describe the non-ideal behavior of a real device [63, 72]. Figure 2.8(a) depicts the resultant electrical circuit with its four constituent parts [65]. The photocurrent source represents the conversion of absorbed photons into free charge by the solar cell and the diode models the recombination of electrons and holes in the device. The series resistor accounts

for the resistance of the cell materials to current flow and includes the resistance of the bulk active layer and the resistance of the contacts. The shunt resistor models the leakage currents through the cell (e.g. via pinholes), around the sides of the device, and between contacts of different polarity. Based on this model, the current density J provided by a real solar cell and recorded on the external load can be expressed as

$$J(V) = -J_{\mathrm{gen}} + J_0 \left(e^{\frac{q(V - JR_{\mathrm{s}})}{n_{\mathrm{id}} k_{\mathrm{B}} T}} - 1 \right) + \frac{V - JR_{\mathrm{s}}}{R_{\mathrm{sh}}}, \tag{2.25}$$

where R_{s} and R_{sh} are the series and shunt resistance, respectively. Both R_{s} and R_{sh} cause a reduction of the solar cell fill factor but their effect on the J-V curve is different, as displayed in Fig. 2.8(b). Since without a current the voltage drop at a resistor is zero, the series resistance has no influence on V_{oc}. Similarly the shunt resistance does not affect J_{sc} because at short circuit the voltage and, thus the current at R_{sh}, equals zero. Equation (2.25) clearly indicates that to be efficient a solar cell needs to posses a small as possible series resistance and a big as possible shunt resistance.

Chapter 3

Recombination Dynamics

In section 2.3 the photovoltaic process for the successful conversion of the incident photons into electrons and holes collected at the contacts was presented. In real devices, each step of this process presents potential loss mechanisms which limit the efficiency of the solar cell. This chapter focuses on the losses caused by the recombination of charge carriers, i.e. the annihilation of electrons and holes, presenting the two main recombination processes. Firstly, the recombination of still Coulombically bound electron-hole pairs, denoted as geminate recombination, is addressed (see Sec. 3.1). Secondly, the nongeminate recombination, involving free charge carriers on their way to the electrodes, is considered (see Sec. 3.2). Since free charge carriers can recombine either in the bulk of the active layer or at the interface between active layer and contacts, section 3.2 also introduces and discusses the distinction between bulk and surface recombination.

3.1 Geminate Recombination

As mentioned in section 2.3 the formation of free charge carriers is hindered by the relatively strong Coulomb binding energy of the electron-hole pair. If this binding energy is not overcome, the electron-hole pair undergoes a recombination process commonly called geminate recombination. Specifically, geminate recombination denotes the recombination at the donor-acceptor interface of an electron and a hole originating from the same photon, while they have not separated into free charges and still are under their mutual electrostatic interaction influence. This process is typical of organic semiconductors which are characterized by low mobilities, low conductivities, and a high

degree of disorder [35, 73]. Geminate recombination takes place on a time scale up to few nanoseconds [74–77] and is considered a monomolecular process [42, 78]. Its contribution largely depends on the Coulomb binding energy of electron-hole pairs and, therefore, may be reduced by applying an external electric field which lowers the energy barrier for free-charge formation. Nevertheless, voltage-dependent geminate recombination has found to be negligible for many state-of-the-art organic solar cells [79–82]. Since every absorbed photon generates one electron-hole pair, geminate recombination scales linearly with light intensity [83], and that is a feature important for the distinction between geminate and nongeminate recombination.

3.2 Nongeminate Recombination

In contrast to geminate recombination, the term nongeminate recombination refers to all processes involving electrons and holes originating from different photons. Nongeminate recombination occurs during the transport of free charge carriers to the electrodes and takes place when two oppositely charged carriers approach below the Coulomb capture radius, i.e. the distance at which the Coulomb binding energy equals the thermal energy. This type of recombination is of great importance in organic solar cells because the low charge-carrier mobilities and the interpenetrating phases make likely the encounter of opposite charges before they reach the electrodes. Free electrons and holes can recombine either in the bulk of the active layer (bulk recombination) or in the vicinity of the opposite electrode (surface recombination).

3.2.1 Bulk Recombination

The term bulk recombination encompasses the recombination events involving free charge carriers in the active layer and, in general, can be limited either by the diffusion of the charge carriers towards each other or by the dissipation of the electron-hole pair energy into vibrational energy. Traditionally, the diffusion-limited recombination has been considered the dominant mechanism in organic solar cells [84–86] but recently Benduhn et al. showed that for a wide range of OSC the energy dissipation step controls the magnitude of non-radiative recombination losses [87].

In the diffusion limit, the basis for the description of direct or bimolecular recombination, i.e. the recombination between two independent and mobile charge carriers,

is the Langevin's model [88,89]. According to this model, every time an electron and a hole approach below the Coulomb capture radius, they recombine. The bimolecular or direct recombination rate R_{dir} is then limited by the slow motion of oppositely charged carriers that need to come together and is given by

$$R_{\mathrm{dir}} = k_{\mathrm{L}}\left(np - n_{\mathrm{i}}^2\right). \tag{3.1}$$

Here n and p are the electron and hole densities, n_{i} represents the intrinsic charge-carrier concentration, and k_{L} is the Langevin recombination prefactor which depends on the charge-carrier mobilities μ_{n} and μ_{p}

$$k_{\mathrm{L}} = \frac{q}{\varepsilon_0 \varepsilon_r}\left(\mu_{\mathrm{n}} + \mu_{\mathrm{p}}\right). \tag{3.2}$$

Since direct recombination requires both charge-carrier types to take place, it is considered a second order process and the recombination probability is expected to be proportional to both charge-carrier densities as stated by Eq. (3.1). Because n_{i}^2 is generally smaller than np, it can be neglected and thus, assuming electric neutrality, i.e. $n \approx p$, Eq. (3.1) can be simplified to

$$R_{\mathrm{dir}} \approx k_{\mathrm{L}} n^2. \tag{3.3}$$

Nevertheless, for many organic solar cells the calculation of R_{dir} via Eq. (3.3) leads to an overestimation of the recombination rate. In order to account for this discrepancy and reproduce the experimentally determined recombination coefficients, a material-specific and temperature-dependent Langevin reduction factor has been introduced [83,90] and the Langevin expression of Eq. (3.3) got to be considered as an upper limit for the bimolecular recombination rate which can be more generally expressed via the direct recombination coefficient k_{dir}: $R_{\mathrm{dir}} = k_{\mathrm{dir}} n^2$.

As mentioned above, the dissipation-limited recombination has recently been found to be of great importance in many donor-acceptor blends and device architectures. Interpreting their results on the basis of the energy gap law, Benduhn et al. [87] showed an inverse relation between the non-radiative energy loss and the energy of the charge transfer (CT) state generated either during charge separation or when the charge carriers meet at the donor-acceptor interface. In fact, according to their model, the rate

of the transition from the CT state to the ground state is proportional to the vibrational wavefunction overlap between these two states, which decreases when the CT state energy is increased. In other words, the energy E_{CT} of the charge transfer state controls the non-radiative recombination rate R_{nrd} because the higher the former is the more phonons with energy $\hbar\omega$ are needed for the energy dissipation and consequently the lower R_{nrd} is [91]

$$R_{\mathrm{nrd}} \propto e^{-\frac{E_{\mathrm{CT}}}{\hbar\omega}}. \tag{3.4}$$

Being the overlap of the vibrational modes of the CT state and the ground state responsible for the increased recombination rate, the high energy intramolecular vibrations in organic molecules can be considered a main cause for non-radiative recombination losses in organic solar cells. In particular, the presence in the backbone of any conjugated polymer or small molecule of C=C double bonds with a vibrational energy of ~ 160 meV makes this non-radiative recombination an intrinsic loss in organic materials.

A reduction of the number of phonons involved in a recombination event may also be caused by the presence of traps and defect states. The recombination with the mediation of traps, commonly called trap-assisted recombination or Shockley-Read-Hall (SRH) recombination, always involves two transitions, namely the transition from conduction band to trap and the transition from trap to valence band [92]. Hence, it is clear that the slower of these two transitions will limit the total recombination rate. If the trap lies in the middle of the energy gap, i.e. it is equally distant to conduction and valence band, the number of phonons involved in the two transitions will be minimized and the recombination rate will be maximized. On the other hand, any shift of the trap position relative to midgap will enlarge the energy of one of the two transitions involved in the recombination process leading to an increase of the number of phonons required and a reduction of the recombination rate. Typically, the recombination via traps is described using Shockley-Read-Hall statistics and the recombination rate R_{SRH} is obtained considering the equations for capture and release of electrons in the conduction band and holes in the valence band by trap states with concentration N_{t} [62]

$$R_{\mathrm{SRH}} = N_{\mathrm{t}}\beta_{\mathrm{n}}\beta_{\mathrm{p}}\frac{np - n_{\mathrm{i}}^2}{n\beta_{\mathrm{n}} + p\beta_{\mathrm{p}} + e_{\mathrm{n}} + e_{\mathrm{p}}}, \tag{3.5}$$

where $\beta_{\mathrm{n/p}}$ is the rate constant for electron/hole capture and $e_{\mathrm{n/p}}$ is the rate constant

for the electron/hole release. The rate constant $\beta_{\mathrm{n/p}}$ is usually expressed in terms of capture cross section $\sigma_{\mathrm{n/p}}$ and thermal velocity $\upsilon_{\mathrm{n/p,th}}$

$$\beta_{\mathrm{n/p}} = \upsilon_{\mathrm{n/p,th}} \sigma_{\mathrm{n/p}}, \tag{3.6}$$

whereas $e_{\mathrm{n/p}}$ is related to the electron and hole densities, n_{t} and p_{t}, obtained when the Fermi level coincides with the energy of the trap through which the recombination occurs. It is also possible to define a lifetime $\tau_{\mathrm{SRH,n/p}}$ for the electron/hole capture which depends on the density of trap states, the thermal velocity, and the capture cross section

$$\tau_{\mathrm{SRH,n/p}} = \frac{1}{\beta_{\mathrm{n/p}} N_{\mathrm{t}}} = \frac{1}{\upsilon_{\mathrm{n/p,th}} \sigma_{\mathrm{n/p}} N_{\mathrm{t}}}. \tag{3.7}$$

The definitions in Eqs. (3.6) and (3.7) permit the expression of the SRH recombination rate as a function of the charge-carrier lifetimes and densities

$$R_{\mathrm{SRH}} = \frac{np - n_{\mathrm{i}}^2}{\tau_{\mathrm{SRH,p}} \left(n + n_{\mathrm{t}}\right) + \tau_{\mathrm{SRH,n}} \left(p + p_{\mathrm{t}}\right)}. \tag{3.8}$$

The expression of R_{SRH} presented by Eq. (3.8) simplifies even further if doped semiconductors are considered. For example, for a p-type semiconductor with doping density N_{A}, provided that $N_{\mathrm{A}} \gg p_{\mathrm{t}}$ and $\tau_{\mathrm{SRH,n}} N_{\mathrm{A}} \gg \tau_{\mathrm{SRH,p}} n_{\mathrm{t}}$, the recombination rate gets proportional to the electron density n

$$R_{\mathrm{SRH}} = \frac{n}{\tau_{\mathrm{SRH,n}}}. \tag{3.9}$$

According to Eq. (3.9), the recombination probability depends just on the amount of mobile charge carriers, which makes the trap-assisted recombination a first order process.

More generally, the recombination rate R can be expressed by a power law with the charge concentration n

$$R \propto n^{\delta}, \tag{3.10}$$

where δ, referred to as the reaction order, describes how R scales with the charge-carrier density and its value relates to the dominant recombination mechanism. In case of direct recombination $\delta = 2$, whereas for trap-assisted recombination $\delta = 1$

because it is assumed that the density of deeply trapped charges does not vary with voltage and illumination. For the intermediate cases, with both bimolecular and trap-assisted recombination, δ lies between 1 and 2. However, in practice, the reaction orders determined experimentally are often greater than 2 [93–95].

Although once the charge-carrier mobilities and the electron density are accurately determined it is possible to calculate the bimolecular recombination rate via Eqs. (3.2) and (3.3), the nongeminate recombination rate can also be obtained from the charge-carrier lifetime and the electron density [79]

$$R = \frac{\mathrm{d}n}{\mathrm{d}t} = \frac{n}{\tau\,(n)} = kn^{\delta}, \tag{3.11}$$

with k being an empirical recombination coefficient and τ an effective charge-carrier lifetime which, enclosing all nongeminate recombination processes, is a measure of the average time a free charge carrier exists before recombining.

It is clear that all nongeminate recombination events reduce the photocurrent by removing charge carriers that otherwise could contribute to the photocurrent. The current losses due to bulk recombination are described by the bulk recombination current $J_{\mathrm{rec,B}}$ obtained integrating the total bulk recombination rate R_{B} over the active-layer thickness d

$$J_{\mathrm{rec,B}} = q\int_{0}^{d} R_{\mathrm{B}}\mathrm{d}x, \tag{3.12}$$

with $R_{\mathrm{B}} = R_{\mathrm{dir}} + R_{\mathrm{SRH}}$.

3.2.2 Surface Recombination

Besides at the internal donor-acceptor interfaces, recombination may take place also at the interfaces between active layer and contacts. This type of recombination, called surface recombination, is governed by the excess minority carriers concentration Δn_{min} at the electrode-active layer interface (holes at the cathode or electrons at the anode) and the surface recombination velocity S_{min}. The surface recombination current density $J_{\mathrm{rec,S}}$, which quantifies the losses due to surface recombination, can be expressed via [96]

$$J_{\mathrm{rec,S}} = qS_{\mathrm{min}}\Delta n_{\mathrm{min.}} \tag{3.13}$$

The surface recombination velocity depends on the concentration of surface states active in recombination and their capture cross section, whereas the concentration of minority carriers at the anode or cathode is decided by their ability of diffusing against the built-in electric field towards the counter electrode [97]. Hence, in addition to S_{min}, surface recombination is affected by charge-carrier mobility, device thickness, and built-in voltage.

Chapter 4

Experimental Setups and Characterization Techniques

In this chapter the organic materials used during this work are introduced together with the device fabrication procedure. Subsequently, the experimental techniques and the simulation tools employed to study charge-carrier transport and recombination are presented and explained.

4.1 Organic Solar Cell Materials

In the last years, the extensive research in the field of organic photovoltaics has led to the development of innumerable organic materials featuring different electrical and optical properties. Depending on their electron affinity, these materials are typically classified as donors or acceptors. This section presents the donor and acceptor materials employed to fabricate the solar cells studied in this work.

4.1.1 Donor Materials

The electron donating materials used in this work are polymers, i.e. macromolecules comprising repeating monomer units. Figure 4.1 displays the chemical structure of the employed donors: the extensively studied poly(3-hexylthiophene-2,5-diyl) normally abbreviated to P3HT, the low bandgap poly({4,8-bis[(2-ethylhexyl)oxy]benzo[1,2-b:4,5-b´]dithiophene-2,6-diyl}{3-fluoro-2-[(2-ethylhexyl)carbonyl]thieno[3,4-b]thiophenediyl})

commonly called PTB7, the copolymer poly[(4,8-bis-(2-ethylhexyloxy)-benzo(1,2-b:4,5-b´)dithiophene)-2,6-diyl-alt-(4-(2-ethylhexanoyl)-thieno[3,4-b]thiophene-)-2-6-diyl)] denoted as PBDTTT-C, and the rather new high-efficiency and low bandgap poly[4,8-bis(5-(2-ethylhexyl)thiophen-2-yl)benzo[1,2-b;4,5-b']dithiophene-2,6-diyl-alt-(4-(2-ethylhexyl)-3-fluorothieno[3,4-b]thiophene-)-2-carboxylate-2-6-diyl)] usually referred to as PCE10.

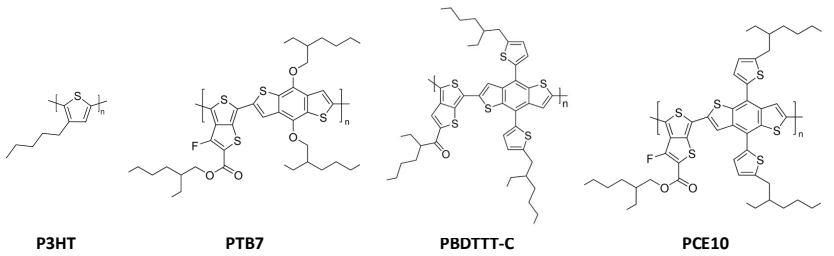

Figure 4.1: Chemical structure of the donor materials used in this work.

P3HT is one of the most studied donor polymers and consists of thiophene rings with an attached hexyl side chain that ensures its solubility. The arrangement of monomers in an alternating head-to-tail configuration results in a polymer with semi-crystalline nature which provides good charge-transport properties and well adapts to the required morphology for bulk heterojunction solar cells. It absorbs light with wavelength from 400 to 650 nm [98] and has a bandagp of 1.9 eV [99]. PTB7 is a well know polymer based on the alternation of ester substituted thieno[3,4-b]thiophene units and benzodithiophene units. In addition to branched side chains in ester and benzodithiophene, which render it well soluble in organic solvents, it features a strong and broad absorption from 550 to 750 nm and a bandgap of 1.84 eV [100]. PBDTTT-C is a benzodithiophene based copolymer with a chemical structure similar to PTB7, a bandgap of 1.57 eV, and an absorption rage up to 770 nm [101]. Finally, the polymer PCE10, obtained incorporating the 2-ethylhexyl-thienyl group into the benzodithiophene unit of PTB7, features a bandgap of 1.58 eV, a broad absorption range (500-785 nm), and higher absorption coefficient compared to PTB7 [102].

4.1.2 Acceptor Materials

Acceptor materials are strongly electronegative compared to the donors and have a LUMO level which allows a fast electron transfer from the donor to the acceptor molecule. In the last decades, the most used and the best performing electron accepting materials have been the fullerene derivatives. One well-known fullerene acceptor molecule is [6,6]-phenyl-C_{61}butyric acid methyl ester ($PC_{61}BM$) obtained adding a side chain to the spherical fullerene C_{60}, which consists of a cage of 60 carbon atoms resembling a football. Thanks to the addition of a side chain, $PC_{61}BM$ becomes easily soluble in typical organic solvents and, thus, can be used for the fabrication of solution-processed solar cells. One of the downsides of $PC_{61}BM$, namely its weak absorption in the visible range, can be partially overcome by using an asymmetrical cage of 70 carbon atoms. The latter is at the basis of the acceptor molecule [6,6]-phenyl-C_{71}butyric acid methyl ester ($PC_{71}BM$) [103] whose chemical structure is displayed in Fig. 4.2. The usage of $PC_{71}BM$ blended with a donor polymer has shown to deliver devices with higher EQE and enhanced photocurrent generation compared to $PC_{61}BM$-based devices [104, 105]. Thus, $PC_{71}BM$ was chosen as principal acceptor material for this work.

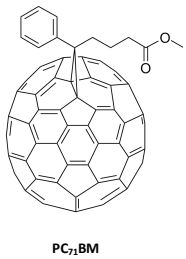

Figure 4.2: Chemical structure of the acceptor molecule $PC_{71}BM$.

4.2 Sample Preparation

As mentioned in section 2.2, the BHJ solar cells used in this work have an inverted structure (see Fig. 2.3) comprising a transparent cathode, a cathode interlayer, an anode interlayer and a non-transparent anode. The fabrication process of such devices

starts with glass substrates covered with indium tin oxide (ITO), which acts as cathode allowing at the same time the illumination of the sample. Before further treatments, all the substrates are cleaned in an ultrasonic bath by consecutive steps with deionized water, acetone, and isopropanol for 10 minutes each. Then, a thin zinc oxide (ZnO) layer ($\sim$ 30 nm) is spin coated on top as cathode interlayer whose purpose is the enhancement of contact selectivity. For this layer a sol-gel method is used in which zinc acetate dihydrate ($Zn\,(CH_3COO)_2 \cdot 2H_2O$) is dissolved in a mixture of 2-methoxyethanol and monoethanolamine. After being annealed at 200 °C for 15 minutes, the substrates are transferred into a two-chamber glovebox with nitrogen atmosphere, which permits to carry out the subsequent steps in absence of oxygen and water, both detrimental for organic materials. The active layer, consisting of an acceptor-donor blend dissolved in an organic solvent (chlorobenzene (CB) or di-chlorobenzene (DCB)), is deposited by spin coating. Different active-layer thicknesses can in this step be achieved by varying the solution concentration and the spin speed parameters. Some acceptor-donor combinations necessitate an additional solvent, namely an additive, to achieve better device performances. Specifically, for the PTB7:$PC_{71}BM$ and the PCE10:$PC_{71}BM$ based samples a 3% by volume of the additive 1,8-diiodooctane (DIO) was used. In addition, the samples based on P3HT:$PC_{71}BM$ underwent solvent annealing for 20 minutes and thermal annealing at 110 °C for 10 minutes to enhance the active-layer morphology before proceeding with the evaporation of the anode. Finally, a 7 nm-thick molybdenum trioxide (MoO_3) layer and a 100 nm-thick silver (Ag) layer are evaporated in high vacuum as metal anode. Figure 4.3 shows the sample stack used in this work whereas Fig. 4.4 depicts the energy levels of the materials employed for the contacts [102, 106, 107], as well as the ones of the donors and the acceptor used for this thesis [102, 108–110].

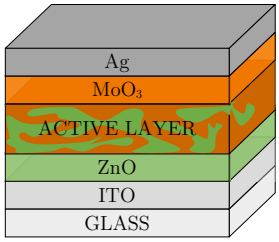

Figure 4.3: Sample stack used in this work.

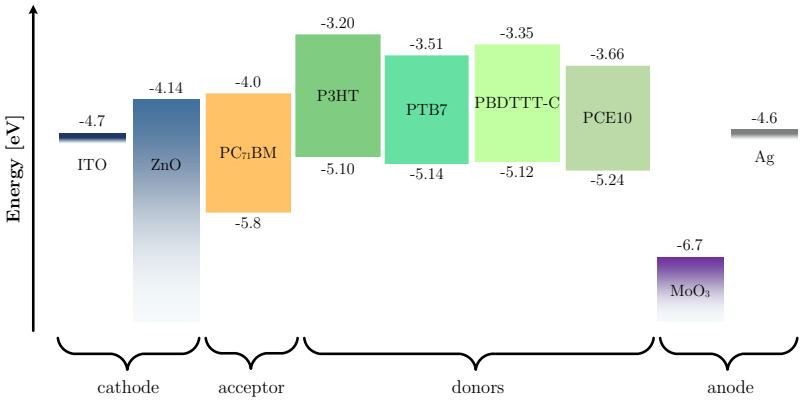

Figure 4.4: Energy levels of the materials used to fabricate the solar cells investigated in this work.

4.3 *J-V* Curves

The first test aimed to check the performance of the fabricated samples was the record of current-voltage *(J-V)* curves in the dark and under illumination. In order to prevent the samples from getting in contact with oxygen and water during the measurements, they were placed inside an hermetic samplebox before taking them out from the glovebox. The measurement light source consisted in a solar simulator from the company LOT Quantum Design encompassing a 150 W xenon lamp and an AM 1.5 filter able to recreate the solar spectrum. A Keithley 2450 acted as source measurement unit applying the desired voltage to the solar cell and measuring the output current. All *J-V* curves were recorded using a 4-cable configuration to reduce the influence of the electrical circuit.

4.4 Impedance Measurements: *C-V* and *C-f* Curves

Impedance spectroscopy (IS) is a widely used method to study the operational mechanisms of various thin-film solar cells including organic solar cells. Impedance-based techniques have in fact been successfully used to investigate charge recombination [111,112], doping concentration [113,114], and the density of states [33] in these devices.

Generally speaking, impedance-based techniques measure the electrical current response of a system to which a small AC voltage perturbation of a certain frequency is applied. Usually, the amplitude of this perturbation is kept below few tens of mV to ensure the linearity of the system response. The measurement of the solar cell impedance, i.e. its complex resistance, is realized using the small AC excitation signal coupled with a DC signal which fixes the operating point of the cell. The ratio between the applied voltage V and the measured current I delivers the impedance Z

$$Z = \frac{V}{I} = Z_0 e^{i\vartheta} = Z_0 \left(\cos\vartheta + i \sin\vartheta\right). \tag{4.1}$$

Besides expressing the impedance with the modulus Z_0 and the phase angle ϑ, it is possible to express it as the sum of a real part Z' and an imaginary part Z'': $Z = Z' + iZ''$. The real part Z' represents the resistance of the system and Z'' the reactance which is determined by the inductance and the capacitance of the measured circuit. However, since in organic solar cells changing magnetic fields are typically not present, no inductance is expected and the imaginary component Z'' is only determined by the capacitance whose value can, therefore, be extracted directly from impedance data. The analysis of the sample signal response is also possible by using its complex admittance Y, which is the inverse of the impedance Z. Analogously to the impedance, the admittance is expressed by the sum of the conductance, representing the real part Y', and the susceptance, identifying the imaginary part Y'': $Y = Y' + iY''$.

In this thesis, the focus will be on the frequency and voltage dependence of the capacitance C, which reveals information about stored or trapped charge in the device as well as transport processes. Two different types of measurement have been carried out with the same setup consisting in the xenon lamp used also for J-V measurements and a Gamry Interface 1000 potentiostat with a 4-cable configuration. In fact, the impedance can be recorded at a fixed frequency f as a function of the DC voltage, or at a fixed DC voltage as a function of the frequency. The former method allows the extraction of a capacitance-voltage (C-V) curve whereas the latter delivers a capacitance-frequency (C-f) curve.

4.4.1 Mott-Schottky Analysis

The analysis of C-V data obtained performing a voltage-dependent impedance measurement in the dark is usually based on the depletion approximation, which assumes that the space-charge region, i.e. the charged region around the junction, is precisely defined and contains just fixed ionized donor or acceptor atoms, no free charge carriers. At the edges of the space-charge region (SCR) the electric field falls to zero and the neutral regions begin. Within these neutral regions, the majority carrier density equals the equilibrium value and the current, driven just by diffusion in absence of an electric field, is determined only by variations in the minority carrier concentration. Under these assumptions, the capacitance C of typical silicon solar cells at low forward or reverse bias behaves like the capacitance of a flat plate capacitor in which the distance between oppositely charged plates is equal to the space-charge region width w determined by the equilibrium between diffusion and electrostatic forces in the junction

$$C = \frac{\varepsilon_0 \varepsilon_\mathrm{r} A}{w}. \tag{4.2}$$

Here ε_0 is the dielectric constant of vacuum, ε_r the relative dielectric constant of the semiconducting material, and A the area of the device. It is well known that for a Schottky junction, i.e. for a one-sided, abruptly ending junction, the SCR width w depends on the doping density N_A, the built-in voltage V_bi and the applied DC bias V [115]

$$w = \sqrt{\frac{2\varepsilon_0 \varepsilon_\mathrm{r} \left(V_\mathrm{bi} - V\right)}{q N_\mathrm{A}}}. \tag{4.3}$$

The substitution of Eq. (4.3) in Eq. (4.2) leads to an expression which emphasizes the proportionality between the inverse square of capacitance and the applied voltage

$$C^{-2} = \frac{2\left(V_\mathrm{bi} - V\right)}{q \varepsilon_0 \varepsilon_\mathrm{r} A^2 N_\mathrm{A}}. \tag{4.4}$$

According to Eq. (4.4), the so-called Mott-Schottky plot of C^{-2} versus applied bias, one example of which is displayed in Fig. 4.5(a), provides a straight line whose extrapolated interception with the voltage axis yields the apparent built-in voltage and whose slope allows the calculation of the apparent doping density via

$$N_{\mathrm{A}} = -\frac{2}{q\varepsilon_0\varepsilon_{\mathrm{r}}}\left[\frac{\mathrm{d}\,(C^{-2})}{\mathrm{d}V}\right]^{-1}. \tag{4.5}$$

As Fig. 4.5(a) clearly shows, the slope of the Mott-Schottky curve gradually decreases to zero as the applied voltage is decreased, i.e. as w approaches the device thickness and the space-charge region capacitance converges to the geometrical capacitance $C_{\mathrm{g}} = \varepsilon_0\varepsilon_{\mathrm{r}}\frac{A}{d}$ of the device determined by the device thickness d and area A. According

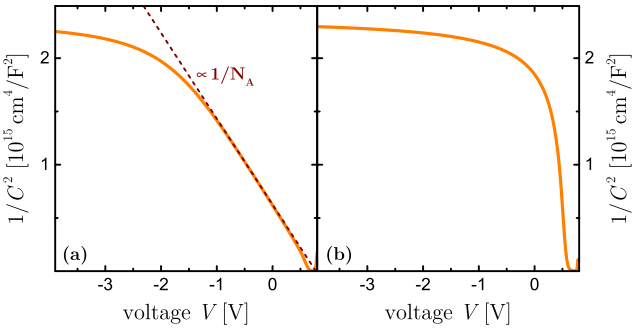

Figure 4.5: Example of Mott-Schottky plot for (a) a 150 nm-thick device with a rather high doping density ($N_{\mathrm{A}} = 5 \cdot 10^{16}$ cm^{-3}) and (b) a 150 nm-thick intrinsic device. In the first case the presence of a clear straight line at forward and low reverse bias allows the determination of the doping density, whereas for the intrinsic device the measured capacitance almost immediately converges to the geometrical capacitance hindering the use of the Mott-Schottky analysis.

to Eq. (4.3), the lower the doping density the bigger w gets and, therefore, the faster w equals the device thickness. Here, it is important to stress that organic solar cells are typically characterized by low doping densities and active-layer thicknesses in the range of few hundred nanometers, and therefore most of them get fully depleted already at low reverse bias, i.e. the width w of the space-charge region equals the absorber-layer thickness d already at small negative applied voltages. Thus, the measured capacitance converges quickly to the plateau defined by C_{g}, as it is displayed in Fig. 4.5(b). As a consequence, the determination of the doping concentration in organic solar cells by using Mott-Schottky analysis becomes rather difficult [32]. Moreover, even for devices with thick active layers or high doping densities, the use of Eq. (4.4) for the interpretation of the Mott-Schottky plot and the use of Eq. (4.5) for the determination

of the apparent doping density is effective only if C-V data obtained in the dark are considered. The interpretation of the results from capacitance-voltage measurements performed under illumination is in fact more difficult and will be addressed in more detail in chapters 6 and 7.

4.4.2 Analysis of *C-f* Data

When the frequency-dependence of the impedance has to be studied, the impedance is measured over a broad frequency range, usually from mHz to MHz. The resulting impedance data can be either displayed as capacitance-frequency curves, an example of which is shown in Fig. 4.6(a), or in the so-called Nyquist plot, which presents the real part Z' on the x-axis and the opposite of the imaginary part Z'' on the y-axis (Fig. 4.6(b)). The latter mode is particularly convenient when the impedance data are

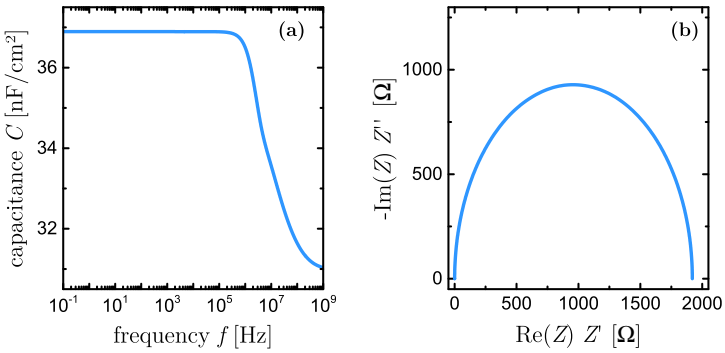

Figure 4.6: Example of (a) capacitance-frequency curve and (b) Nyquist plot under illumination.

treated with the commonly used equivalent circuit analysis, which consists in modeling the system under test with a network of passive electrical circuit elements and in fitting the impedance of this electrical circuit to the measured impedance. Figure 4.7 shows the equivalent circuit used in this work together with the Nyquist plot obtained measuring a bulk heterojunction solar cell under 0.01-sun illumination. The circuit in Fig. 4.7(a) consists of an external series resistance R_s which accounts for the resistive losses due to wires and connection to the device electrodes, an internal series resis-

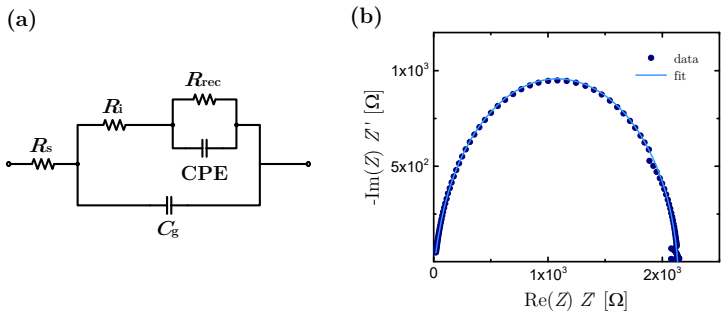

Figure 4.7: (a) Equivalent circuit model used in this work and (b) Nyquist plot of a bulk heterojunction solar cell obtained measuring under 0.01-sun illumination. The response of the equivalent circuit can be calculated and compared to the measured impedance data. The resulting fit line is displayed by the light blue line in (b).

tance R_{i} that considers the losses occurring during the transport of charge carriers, a capacitance C_{g} corresponding to the geometrical capacitance, and a parallel between the recombination resistance R_{rec} and the constant phase element *CPE* , both associated to the recombination events occurring in the bulk of the active layer [116]. The constant phase element is often used in place of a capacitor to describe materials whose microscopic properties are distributed and which are characterized by a distribution of relaxation times. In fact, the *CPE* acts as non-ideal capacitor featuring a distribution of time constants and enables the simplification of the equivalent circuit model. The impedance of a constant phase element is defined as

$$Z_{\mathrm{CPE}} = \frac{1}{Y_0 \left(i\omega\right)^{\alpha}}, \tag{4.6}$$

where Y_0 represents the magnitude of the *CPE* and α is a factor that indicates how much the behavior of the *CPE* differs from the behavior of an ideal capacitor. The factor α assumes the value 1 for an ideal capacitor and decreases towards zero as the behavior of the *CPE* deviates from the one of an ideal capacitor. By using the definition expressed in Eq. (4.6), the impedance of the parallel connection between the recombination resistance and the constant phase element is found to be

$$Z_{\mathrm{R_{rec}}\|\mathrm{CPE}} = \frac{R_{\mathrm{rec}}}{1 + R_{\mathrm{rec}} Y_0 \left(i\omega\right)^{\alpha}}. \tag{4.7}$$

The response of the equivalent circuit depicted in Fig. 4.7(a) can therefore be calculated and compared to the actual response of the device under investigation. An example of the use of the aforementioned equivalent circuit to fit experimental data plotted in form of Nyquist plot is presented in Fig 4.7(b). This fitting procedure allows the extraction of two key parameters, namely the chemical capacitance due to the charge carriers accumulated in the active layer and the recombination resistance, which together permit to determine the charge-carrier lifetime. Since in the equivalent circuit considered here the ideal capacitor representing the chemical capacitance is replaced by the constant phase element, an equivalent capacitance C_{eq} is needed for the determination of the average lifetime τ_{avg} [116]

$$\tau_{\mathrm{avg}} = (R_{\mathrm{rec}} Y_0)^{\frac{1}{\alpha}} \tag{4.8}$$

and

$$C_{\mathrm{eq}} = \frac{\tau_{\mathrm{avg}}}{R_{\mathrm{rec}}} = \frac{(R_{\mathrm{rec}} Y_0)^{\frac{1}{\alpha}}}{R_{\mathrm{rec}}}. \tag{4.9}$$

The definition of the equivalent capacitance allows to more easily relate the properties of the *CPE* with the physical process of charge-carrier accumulation in the photoactive layer, which is normally associated with the chemical capacitance [117].

Upon the application of an appropriate equivalent electrical circuit to fit the measured impedance spectra, the deconvolution of the overall system response and the acquisition of some insights into the individual processes occurring inside the sample become possible. However, this approach has some downsides. First of all, in order to be effective, this analysis needs some prior knowledge on how the system might be modeled. Moreover, the choice of the appropriate circuit can be challenging due to the non-uniqueness of the equivalent circuit, which implies that several circuit models may provide the same impedance response over the chosen frequency range. Another disadvantage lies in the possibility to fit the measured impedance spectra with a potential infinitely complex equivalent circuit with only few elements having a real physical meaning. A more universal method to extract information about the charge-carrier density and lifetime avoiding the aforementioned problems involves the direct analysis of the frequency-dependent capacitance measured at different voltages. This approach will be introduced in chapter 8.

4.5 Solar Cell Simulation

In parallel with the experimental measurements described above, drift-diffusion simulations were regularly carried out during the work presented in this thesis. The simulation of the optical and electrical behavior of semiconductor devices is indeed a powerful tool to improve the understanding of the physics relevant to the device operation. For all simulations the effective medium approach was used. Under the assumption of an intimate intermixing, the active-layer blend might in fact be treated as one effective medium whose hole conducting properties are derived from the donor material and whose electron conducting properties are defined by the acceptor material. Thus, all the charge-carrier-related properties of the effective medium are defined by the appropriate pristine material and the effective energy gap is given by the difference between the acceptor LUMO and the donor HOMO level. The effective medium approach works rather well for blends with a very fine phase separation, but it is unable to correctly describe the behavior of blends with coarser phase separation. Nevertheless, performing simulations based on the effective medium assumption saves numerical time and effort and offers the possibility of gaining a good insight into the impact of microscopic properties (such as charge-transport and recombination properties) on macroscopic device parameters, like J-V and C-V characteristics [118–121]. For this thesis two numerical simulation tools were used, namely ASA and SCAPS .

4.5.1 ASA

The software ASA (Advanced Semiconductor Analysis) [122] is a one-dimensional, steady-state device simulator developed at Delft University of Technology. It is designed to model both optical and electrical properties of multi-layer device structures. For the drift-diffusion simulations, ASA uses the free electron and free hole concentrations and the electrostatic potential as variables and solves the Poisson equation together with the continuity equations for electrons and holes. The software permits to define the solar cell as a multi-layer structure consisting of electrically-active layers and layers that are only relevant to the optical behavior of the device. The parameters defining these layers are contained in the main input file. The latter includes the structure specification (number, type, and thickness of the layers), the material specifications (semiconducting material properties of the layers, doping density, charge-carrier

mobility, and charge-carrier lifetime), the valence and conduction band tail state distributions, and the contact conditions at the boundaries of the simulation grid. The user can perform simulations both with Shockley-Read-Hall and direct recombination as bulk recombination mechanism while surface recombination of holes at the cathode and electrons at the anode can be set. Once all structural and material parameters are defined, ASA simulates the device performance and the relevant device physical quantities can be obtained. The natural outputs of a simulation performed with ASA are the electric potential of the vacuum level, the free electron concentration, and the free hole concentration as a function of position in the solar cell. However, also device performance parameters such as the open-circuit voltage, the short-circuit current, the fill factor, and the current-voltage characteristics in the dark and under illumination are obtained from an ASA simulation.

As already mentioned, ASA also allows to perform optical simulations to obtain absorption and generation profiles in solar cells. Several optical models are implemented, but for the work presented in this thesis only the *genpro1* subroutine was used. Here, the solar cell is treated as a multi-layer optical system whose optical behavior, i.e. reflectance, transmittance, and absorptance, is calculated using the theory of thin-film optics. In this approach, transmission and reflection at all interfaces as well as the absorption in all layers of the system are taken into account, while scattering at interfaces is neglected.

4.5.2 SCAPS

SCAPS (Solar Cell Capacitance Simulator) [123] is a one-dimensional solar cell simulator developed at the University of Gent. It was originally developed for simulating thin-film Cu(In,Ga)Se_2 and CdTe devices, but it has recently been used also for amorphous silicon and organic solar cells. Analogously to ASA, the software SCAPS simulates the behavior of a solar cell by solving the Poisson equation and the continuity equations for electrons and holes. However, it allows to perform not only steady-state simulations but also frequency-domain simulations. This means that also the capacitance of the solar cell can be modeled as a function of frequency, voltage, or temperature. Thanks to the interactive graphical interface, SCAPS is relatively easy to learn and intuitive to control and use. All parameters defining the contacts and the active layer of the device can be easily set by using the Solar Cell Definition Panel, which also allows to

choose the bulk recombination mechanism and the amount of surface recombination at the contacts. All simulations can be performed in the dark or under illumination, even though SCAPS does not provide sophisticated optical models. However, it is possible to create a generation profile using another optical simulator and then import this generation profile in SCAPS.

Chapter 5

Distinguishing between Surface and Bulk Recombination

This chapter presents a study of charge-carrier recombination in bulk heterojunction solar cells realized through current-voltage measurements. It introduces a method, based on the thickness dependence of the saturation current density, to distinguish between surface and bulk recombination in organic solar cells. First, numerical simulations are used to illustrate and present the methodological approach. Secondly, the saturation current density of organic solar cells based on different polymer:fullerene systems and characterized by diverse architectures is derived from light J-V curves and its thickness dependence is analyzed using the new approach. This chapter is based on the results presented in the paper *Discriminating between surface and bulk recombination in organic solar cells by studying the thickness dependence of the open-circuit voltage* by Zonno et al. [124], which is published by AIP Publishing.

5.1 Introduction

The identification of the main source of nongeminate recombination losses in a given device is of high general interest for the field of photovoltaics due to the detrimental effect of these losses on the open-circuit voltage. Even though it may be possible to identify the dominant bulk recombination mechanism, the distinction between recombination at the interface between absorber and electrodes, i.e. surface recombination, and

recombination in the bulk of the absorber can be extremely challenging [96, 125]. This is especially true when dealing with new material systems such as absorbers based on organic molecules; their mobilities and bulk lifetimes might in fact not be sufficiently well known to be able to take their influence into account quantitatively such that surface properties can be extracted from measurements of the effective lifetime of the whole device. The present chapter provides an analysis of the thickness dependence of the saturation current density aimed to determine which recombination mechanism between surface and bulk recombination is more dominant in different organic solar cells.

5.2 Theoretical Background

Surface and bulk recombination currents depend differently on the absorber-layer thickness. This relatively trivial observation is based on the fact that bulk recombination currents scale at a given recombination rate linearly with the thickness, while surface recombination should be either unaffected by thickness or even decrease in relevance. The decrease in the contribution of surface recombination would be expected since the diffusion of charge carriers to the surface becomes less efficient the further away the surface is on average [126]. Thus, if material and interface properties, like the bulk lifetime and the surface recombination velocity, stay constant as a function of absorber-layer thickness, we would expect the total recombination current to scale differently in a device dominated by surface recombination than in a device dominated by bulk recombination. From a practical perspective, we have to first of all decide how to compare recombination currents between devices with different thicknesses. Because we are interested in the conditions under illumination, it would be ideal to derive recombination currents from the light current-voltage curves of the solar cells under investigation. The open-circuit condition could be a suitable working point to study because the voltage at open circuit depends entirely on the balance between generation and recombination and not like at other working points also on resistive effects. However, a look at the equation defining the open-circuit voltage, $V_{\mathrm{oc}} = \frac{n_{\mathrm{id}} k_{\mathrm{B}} T}{q} \ln\left(\frac{J_{\mathrm{gen}}}{J_0} + 1\right)$, makes clear that the thickness dependent open-circuit voltage does not directly reveal how recombination scales with thickness because it also includes information about how photogeneration scales with thickness. Because the solar cell absorptance, and therefore the total amount of

charge carriers photogenerated, is a strong and not always easy to predict function of absorber-layer thickness, it is advisable to firstly disentangle the effects of generation and recombination. One way of doing this at open circuit, i.e. when the total current is zero, is to equate the current densities J_{gen} due to generation and J_{rec} due to recombination

$$J_{\mathrm{gen}} = J_0 e^{\frac{qV_{\mathrm{oc}}}{k_{\mathrm{B}}T}} = J_{\mathrm{rec}}. \tag{5.1}$$

Here $k_{\mathrm{B}}T$ is the thermal energy, q the elementary charge, V_{oc} the open-circuit voltage, and $V_{\mathrm{oc}} \gg k_{\mathrm{B}}T/q$ is assumed. According to Eq. (5.1), the current density due to recombination J_{rec} can be divided into an exponentially voltage dependent factor $e^{\frac{qV_{\mathrm{oc}}}{k_{\mathrm{B}}T}}$ and a voltage independent or weakly voltage dependent factor J_0. One can then define the saturation current density J_0 via [127]

$$J_0 = J_{\mathrm{gen}} e^{-\frac{qV_{\mathrm{oc}}}{k_{\mathrm{B}}T}}. \tag{5.2}$$

In many cases, where solar cells collect charges efficiently at short circuit, the short-circuit current density J_{sc} is already a good approximation for J_{gen}. If this is not the case, J_{gen} can be approximated by the photocurrent density $J_{\mathrm{ph}} = J_{\mathrm{light}} - J_{\mathrm{dark}}$ at a sufficiently high reverse bias where collection has saturated. Here, J_{light} and J_{dark} are the current densities under illumination and in the dark, respectively. Note that Eq. (5.2) lacks the ideality factor because it assigns any voltage dependence of recombination that does not follow the ideal relation $J_{\mathrm{rec}} \propto e^{\frac{qV_{\mathrm{oc}}}{k_{\mathrm{B}}T}}$ to a voltage dependence of J_0. It is therefore important to notice that the obtained J_0 corresponds to a specific situation in the device, namely open circuit under specific illumination conditions (i.e. the conditions used to determine J_{gen} and V_{oc} in Eq. (5.2)).

The recombination current density $J_{\mathrm{rec}} = J_{\mathrm{rec,S}} + J_{\mathrm{rec,B}}$ can be expressed as a sum of the contribution $J_{\mathrm{rec,S}}$ from surface recombination and $J_{\mathrm{rec,B}}$ from bulk recombination. The current density $J_{\mathrm{rec,S}}$ follows from the excess minority charge densities and surface recombination velocities at the electrodes via

$$J_{\mathrm{rec,S}} = qS_{\mathrm{na}}\Delta n_{\mathrm{a}} + qS_{\mathrm{pc}}\Delta p_{\mathrm{c}}, \tag{5.3}$$

where S_{na} is the surface recombination velocity of electrons at the interface to the anode and S_{pc} is the surface recombination velocity of holes at the interface to the

cathode. The surface recombination velocities S_{na} and S_{pc} have to be multiplied with the excess electron concentration Δn_{a} at the anode and the excess hole concentration Δp_{c} at the cathode, respectively, to obtain the surface recombination rate per area. Multiplication with the elementary charge q finally yields the current density $J_{\mathrm{rec,S}}$. The bulk recombination current density can be obtained from an integral of the bulk recombination rate R_{B} over the depth of the absorber via

$$J_{\mathrm{rec,B}} = q \int_0^d R_{\mathrm{B}}(x)\mathrm{d}x. \tag{5.4}$$

Here, x is the spatial position in the absorber layer of thickness d. In addition, since at open circuit $J_{\mathrm{gen}} = J_{\mathrm{rec}}$, we can use $J_{\mathrm{rec,S}}$ and $J_{\mathrm{rec,B}}$ together with Eq. (5.2) to split up the saturation current density into two parts, namely

$$J_{0,\mathrm{S}} = J_{\mathrm{rec,S}} e^{-\frac{qV_{\mathrm{oc}}}{k_{\mathrm{B}}T}} \tag{5.5}$$

and

$$J_{0,\mathrm{B}} = J_{\mathrm{rec,B}} e^{-\frac{qV_{\mathrm{oc}}}{k_{\mathrm{B}}T}}, \tag{5.6}$$

where $J_0 = J_{0,\mathrm{S}} + J_{0,\mathrm{B}}$ is valid.

5.3 Results from Simulation

We have now seen how to express the saturation current density as function of the surface and bulk recombination currents which help splitting it up into two parts, $J_{0,\mathrm{S}}$ and $J_{0,\mathrm{B}}$. While $J_{0,\mathrm{S}}$ and $J_{0,\mathrm{B}}$ are not accessible from experiments, it is possible to use Eqs. (5.3)-(5.6) to calculate them using numerical simulations. The drift-diffusion simulations were performed using the electrical model of the software ASA together with its built-in transfer matrix code *genpro1* to create a real generation profile. As already explained in section 4.5.1, the subroutine *genpro1* allows a rather precise determination of the absorption profile of the solar cell under study treating it as a multi-layer optical system whose optical behavior is calculated using the theory of thin-film optics. The device stack used for the creation of the generation profile was glass/indium-tin oxide (ITO)/poly(3,4-ethylenedioxylenethiophene):poly(4-

styrenesulfonic acid) (PEDOT:PSS)/P3HT:$PC_{61}BM$/Ca/Al and the thicknesses of the glass, ITO, PEDOT:PSS, Ca, and Al layers were set respectively to 1 mm, 120 nm, 25 nm, 30 nm, and 150 nm. Figure 5.1 displays the optical data, namely the refractive index n and the extinction coefficient k, of the materials constituting the simulated device that were used to create the generation profile. The software ASA allowed to

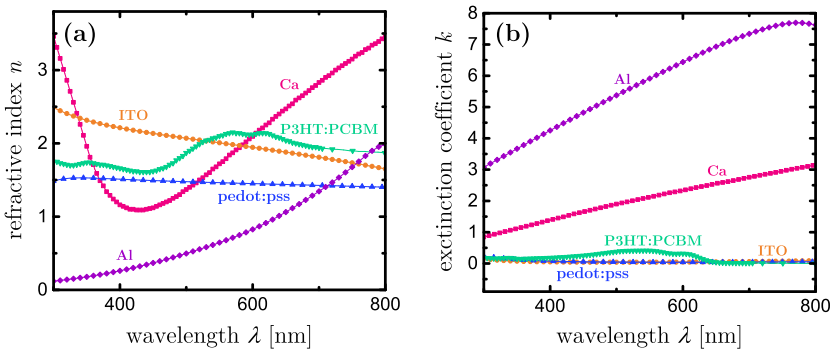

Figure 5.1: Refractive index n and extinction coefficient k of the simulated device materials utilized to create the generation profile with ASA [128–130].

simulate the chosen device with two different models for recombination, namely direct recombination and Shockley-Read-Hall (SRH) recombination, and permitted to vary the thickness of the active layer from 50 to 1000 nm. The parameters used for the simulations performed with the software ASA are summarized in Table 5.1. The simulations results contained the values of all quantities needed for the determination of the surface and bulk recombination currents as well as the open-circuit voltage necessary to calculate the saturation current density. Figure 5.2 shows the results for J_0, $J_{0,\mathrm{B}}$, and $J_{0,\mathrm{S}}$ calculated from simulated data for different conditions. Figures 5.2(a) and 5.2(c) show the case of direct recombination as only bulk recombination mechanism, i.e. the bulk recombination rate is given by $R_\mathrm{B} = k_\mathrm{dir}\,(np - n_\mathrm{i}^2)$, where k_dir is the recombination coefficient, n and p are the electron and hole concentrations, respectively, and n_i^2 is the intrinsic charge-carrier concentration. On the other hand, Figs. 5.2(b) and 5.2(d) present the case where bulk recombination is dominated by Shockley-Read-Hall recombination and, thus, $R_\mathrm{B} = (np - n_\mathrm{i}^2)\,/\,(n\tau_\mathrm{p} + p\tau_\mathrm{n})$, where τ_n and τ_p are the electron and hole lifetimes. In order to investigate in detail the effect of surface recombination

Table 5.1: Parameters used for the simulations with the software ASA.

	Quantity	Default set
Band mobility	μ_n [cm^2/Vs]	10^{-4}
	μ_p [cm^2/Vs]	10^{-4}
Effective density of states	$N_\mathrm{C} = N_\mathrm{V}$ [cm^{-3}]	10^{19}
Density of tail states	$N_\mathrm{Ctail} = N_\mathrm{Vtail}$ [cm^{-3}]	5×10^{19}
Characteristic tail slope	$E_\mathrm{ch,C} = E_\mathrm{ch,V}$ [meV]	50
Capture coefficients	β_n^+ [cm^3/s]	10^{-12}
	β_p^0 [cm^3/s]	10^{-10}
	β_p^- [cm^3/s]	10^{-12}
	β_n^0 [cm^3/s]	10^{-10}
Bandgap	E_g [eV]	1.12
Thickness	d [nm]	Variable
Doping concentration	N_A [cm^{-3}]	0
Surface recombination velocity	S [cm/s]	10 or 10^4
Contact barrier heights	φ_b [meV]	50
Generation rate	G [cm^{-3}s^{-1}]	Calculated with a transfer matrix algorithm
Direct recombination coefficient	k_dir [cm^3/s]	10^{-12}
Shockley-Read-Hall lifetime	$\tau_\mathrm{SRH,n}$ [μs]	10
	$\tau_\mathrm{SRH,p}$ [μs]	10

on the saturation current, simulations with two different surface recombination velocities were performed. The results in Figs. 5.2(a) and 5.2(b) correspond to the cases with a relatively lower amount of surface recombination ($S = 10$ cm/s) than the cases presented in Figs. 5.2(c) and 5.2(d) ($S = 10^4$ cm/s).

In general, it can be observed that the saturation current density $J_\mathrm{0,B}$ due to bulk recombination is increasing with thickness and its slope $d\ln(J_\mathrm{0,B})/d\ln(d)$ seems to be

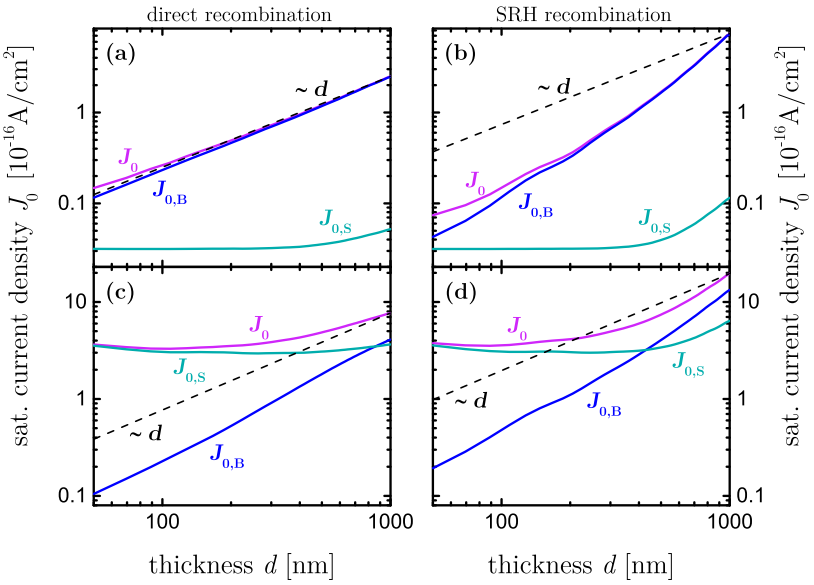

Figure 5.2: Saturation current densities J_0, $J_{0,B}$, and $J_{0,S}$ calculated from simulated data for different conditions. (a) and (c) present the case of direct recombination only. (b) and (d) present the case where bulk recombination is dominated by Shockley-Read-Hall recombination. The results in (a) and (b) were obtained using a relatively lower amount of surface recombination than the results in (c) and (d). In all cases, the saturation current density $J_{0,B}$ due to bulk recombination increases with thickness and its slope is 1 or higher. In contrast, the saturation current density $J_{0,S}$ due to surface recombination decreases or remains constant with thickness for $d < 400$ nm.

1 or higher. In contrast, the saturation current density $J_{0,S}$ due to surface recombination shows a more complicated behavior. For low thicknesses ($d < 100$ nm) and high surface recombination velocities S (Figs. 5.2(c) and 5.2(d)), $J_{0,S}$ decreases with thickness, i.e. $d\ln(J_{0,S})/d\ln(d) < 0$. This is due to the fact that the transport of charge carriers to the surface limits surface recombination [131] and this transport is more efficient when the surface is close by, i.e at low thicknesses [126]. In contrast, if the surface recombination velocity is small (Figs. 5.2(a) and 5.2(b)) the transport to the surface is efficient and recombination at the surface is the rate limiting step [131]. In this latter case, $J_{0,S}$ is constant for small thicknesses. Regardless of the dominant

bulk recombination mechanism, for larger thicknesses ($d > 400$ nm) $J_{0,S}$ increases with thickness because the optical generation is spatially inhomogeneous. In fact, at larger thicknesses, a large amount of photons will be absorbed close to the transparent front electrode that sees the light first. This will also create an inhomogeneous profile of charge carriers (even at open circuit) that will lead to increased recombination rates where the optical generation rates are higher. Because this occurs close to one of the contacts, surface recombination at this contact will become very important and lead to $d\ln(J_{0,S})/d\ln(d) > 0$.

By looking at Fig. 5.2 it becomes evident that, even though there is a quantitative difference between direct (Figs. 5.2(a) and 5.2(c)) and SRH recombination (Figs. 5.2(b) and 5.2(d)), the trends for J_0, $J_{0,B}$, and $J_{0,S}$ are qualitatively the same. Especially at higher thicknesses, SRH recombination allows $J_{0,B}$ to scale superlinearly with thickness, while direct recombination typically leads to a slope $d\ln(J_{0,B})/d\ln(d)$ very close to 1 in all performed simulations.

Since $J_{0,B}$ and $J_{0,S}$ behave differently as a function of the absorber-layer thickness and the saturation current density J_0 is given by their sum, it subsists the possibility to assign the dominant recombination mechanism either to the surface or to the bulk (or internal interfaces in case of organic solar cells) from studying J_0 as a function of thickness.

5.4 Experimental Results

In order to test whether the explanation of the simulated data presented in the previous section is applicable also to experimental data, we checked our predictions on data obtained measuring bulk heterojunction solar cells. Devices with a PTB7:$PC_{71}BM$ active layer were fabricated with and without the solvent additive 1,8-diiodooctane (DIO) using the inverted structure glass/ITO/ZnO/PTB7:$PC_{71}BM$/MoO_3/Ag, as described in section 4.2. The use of different revolution speeds by the spin coating of the polymer:fullerene solution allowed us to obtain various active-layer thicknesses (from 68 to 242 nm). Moreover, thanks to the large body of work available on organic solar cells, additional data referred to devices based on several polymer:fullerene systems could be analyzed with our method. Figure 5.3 presents the results for the saturation current density J_0 calculated using Eq. (5.2) on a range of experimental data from our labo-

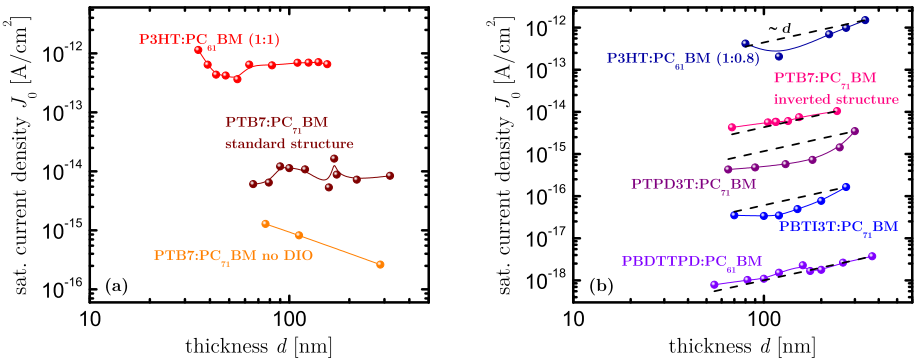

Figure 5.3: Saturation current density J_0 calculated for a range of different polymer:fullerene systems. The filled circles represent the values of J_0 derived from the open-circuit voltage and the short-circuit current, while the lines are just a guide to the eye. The dashed lines indicate a proportionality between J_0 and d, i.e. a slope of $d\ln(J_0)/d\ln(d) = 1$. Panel (a) shows the cases where recombination is mostly limited by recombination at the surface, while panel (b) presents the cases of mostly and purely bulk dominated recombination.

ratory and from literature. Figure 5.3(a) shows three cases where J_0 either is constant or decreases with active-layer thickness. The device fabricated in our laboratory using PTB7 as electron donor and $PC_{71}BM$ as electron acceptor and without the additive DIO shows a saturation current density J_0 which decreases with thickness, indicating a surface limited recombination. The device made from PTB7 and $PC_{71}BM$ with a standard structure as described in Ref. [132] exhibits a nearly constant value for J_0 over the entire thickness range considered. This behavior suggests a system where the transport of charge carriers to the surface is efficient and the rate limiting step is the recombination at the surface. For the device based on P3HT and $PC_{61}BM$ blended with a 1:1 weight-ratio as reported in Ref. [133] the slope $d\ln(J_0)/d\ln(d)$ is negative at low thicknesses. This trend is similar to the one presented in Fig. 5.2(c) where the surface recombination is so high that it is limited by the transport of charge carriers to the contacts. In conclusion, it can be assumed that for these cells surface recombination is the dominant recombination mechanism.

Figure 5.3(b) presents cases where recombination in the bulk plays a bigger role in determining the dominant recombination mechanism. For both self-prepared PTB7:

$PC_{71}BM$ with DIO and an inverted structure and poly(di(2-ethylhexyloxy)benzo[1,2-b:4,5-b']dithiophene-co-octylthieno[3,4-c]pyrrole-4,6-dione) (PBDTTPD):$PC_{61}BM$ (fabricated as described in Ref. [134]) devices, the saturation current density J_0 increases monotonously with thickness and its slope $d\ln(J_0)/d\ln(d)$ is approximately equal to 1 over the whole thickness range considered. This trend clearly identifies bulk recombination as the dominant recombination mechanism in both systems. In contrast, the P3HT:$PC_{61}BM$ (1:0.8), poly[N-(2-hexyldodecyl)-2,2'-bithiophene-3,3'-dicarboximide-alt-5,5-(2,5-bis(3-decylthiophen-2-yl)-thiophene)] (PBTI3T):$PC_{71}BM$, and poly[5-(2-hexyl dodecyl)-1,3-thieno[3,4-c]pyrrole-4,6-dione-alt-5,5-(2,5-bis(3-dodecylthiophen-2-yl)-thio phene)] (PTPD3T):$PC_{71}BM$ samples, fabricated as described in Ref. [135], [86], and [116], respectively, exhibit an intermediate behavior with J_0 affected by both surface and bulk recombination. In fact, the saturation current density J_0 of these three systems decreases or remains constant with d for low thicknesses, while it increases with d for larger thicknesses. Thus, at low thicknesses the slope $d\ln(J_0)/d\ln(d)$ is equal to 0 or less, suggesting a bigger impact of surface recombination, and at high thicknesses $d\ln(J_0)/d\ln(d)$ is higher than 1, indicating that bulk recombination starts being more dominant at open circuit.

5.5 Conclusions

In this chapter, a new method to discriminate between surface and bulk recombination in organic solar cells was presented. The basis of this novel approach lies on the thickness dependence of the saturation current density which is derived from the open-circuit voltage and the photocurrent at short circuit or reverse bias. Numerical simulations performed with the software ASA showed that the bulk recombination current increases with thickness while for low thicknesses ($d < 400$ nm) the surface recombination current decreases or remains constant with thickness. This different scaling with thickness allows one to assign the dominant recombination mechanism of the solar cell under investigation either to the surface or to the bulk. The application of the new method on a range of experimental data from our laboratory and from literature pointed out that in the field of organic photovoltaics the whole range of cases, from mostly surface limited to purely bulk limited recombination, can be observed.

Chapter 6

Understanding Mott-Schottky Measurements under Illumination

In this chapter, capacitance-voltage measurements on bulk heterojunction solar cells under illumination are studied with the purpose of identifying which physical mechanisms affect the Mott-Schottky analysis under illumination and determining whether the charge-carrier mobility can be extracted from such measurements. The first part introduces the theoretical model for the description of the photocapacitance whereas the second part shows experiments and simulations aimed to explain the features observed in capacitance-voltage measurements performed under illumination on lowly doped and relatively thin devices. The results presented here are published in the paper *Understanding Mott-Schottky Measurements under Illumination in Organic Bulk Heterojunction Solar Cells* by Zonno et al. [136] whose copyright lies by the American Physical Society.

6.1 Introduction

As already illustrated in section 4.4.1, the Mott-Schottky analysis in the dark is a useful method to determine the doping concentration of semiconductors from capacitance-voltage (C-V) measurements. This basic impedance-based technique has been frequently used also in the field of organic photovoltaics because it allows one to derive the doping concentration for sufficiently thick absorber layers [32, 115] and gives some

information about the amount of band bending in the device under investigation. However, while the analysis of capacitance-voltage measurements in the dark is relatively well established, the analysis of data taken under illumination is currently not fully understood. In fact, C-V measurements under illumination have shown features that were not straightforward [137, 138] to explain with analytical equations and, therefore, have been much more difficult to interpret [139, 140]. In the following, capacitance-voltage measurements performed at reverse bias on fully depleted organic solar cells under illumination are analyzed. The case considered here is therefore the one highlighted in Table 6.1, which presents an overview of the different options to analyze capacitance-voltage measurements as a function of the properties of the sample and the conditions of the measurement.

Table 6.1: Information accessible through the analysis of capacitance-voltage data depending on the sample properties and the measurement conditions.

	$w < d$	$w \approx d$
DARK	at $V \leq 0$ space-charge capacitance provides the doping density	at $V > 0$ chemical capacitance related to the density of states
LIGHT	at $V = 0$ to be discussed in chapter 7	at $V \leq 0$ to be discussed here

6.2 Theoretical Model

For a diode under illumination, the quasi-Fermi levels at short circuit are equal at the two contacts, i.e. the voltage is zero. However, they are not necessarily equal in the bulk of the device and, depending on the charge-carrier mobilities and the amount of illumination, charge carriers can build up in the device. This concept is illustrated in Fig. 6.1 which displays the effect of charge-carrier mobility on the energy-band diagram obtained from the simulation at 0 V (short-circuit conditions) of a 100 nm-thick intrinsic solar cell under 1-sun illumination. The data were obtained performing frequency-dependent drift-diffusion simulations with the software SCAPS (see Sec. 4.5.2) using the parameters summarized in Table 6.2. The chosen bandgap (1.0 eV) is representative

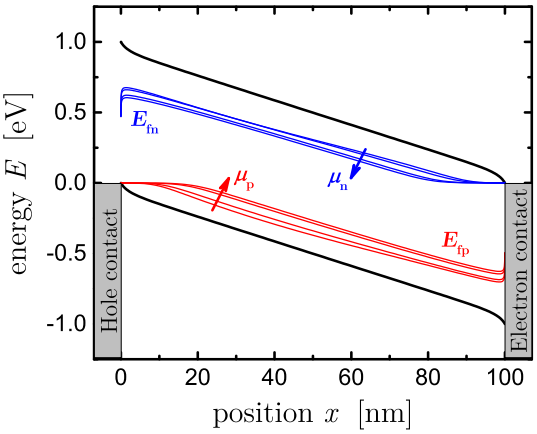

Figure 6.1: Band diagram of a 100 nm-thick intrinsic solar cell under 1-sun illumination and short-circuit conditions (applied voltage $V_{ext} = 0\,V$) for different electron and hole mobilities. The quasi-Fermi-level splitting $E_{Fn} - E_{Fp}$ in the active layer increases with decreasing mobility and the charge-carrier densities change consequently.

of the energy of a charge transfer state in a very low bandgap blend and the other parameters are typical for organic semiconductors used in solar cell. Figure 6.1 clearly shows that the quasi-Fermi-level splitting, $E_{Fn} - E_{Fp}$, in the active layer increases progressively with decreasing mobility and, consequently, the charge density increases as well. The amount of illumination has the opposite effect on the charge density, since the latter increases with increasing light intensity. Thus, the higher the illumination and the lower the mobilities, the more charge carriers will exist at short circuit in a device and will, therefore, contribute to its capacitance. From this observation, it becomes evident that a measurement of either the charge density or the capacitance under illumination will provide information about the charge-carrier mobilities. This concept has been used previously in the time domain, for instance by Shuttle et al. [141], to determine the mobility in organic solar cells by measuring the extracted charge density under illumination at short circuit. Equivalent information can be obtained also using capacitance measurements under illumination and at short circuit or reverse bias once the photocapacitance, i.e. the capacitance due to illumination, is expressed with an analytical equation. An expression for the photocapacitance of a *p-i-n* *a*-Si:H solar cell was derived by Crandall [142] in 1983, but here we will briefly present an

Table 6.2: Parameters used for the simulations with the software SCAPS if not stated otherwise.

	Quantity	Default set
Band mobility	μ_n [cm^2/Vs]	5×10^{-4}
	μ_p [cm^2/Vs]	5×10^{-4}
Effective density of states	$N_\mathrm{C} = N_\mathrm{V}$ [cm^{-3}]	10^{19}
Bandgap	E_g [eV]	1.0
Thickness	d [nm]	100
Doping concentration	N_A [cm^{-3}]	0
Relative permittivity	ε_r	3.5
Direct recombination coefficient	k_dir [cm^3/s]	5×10^{-12}

easier and shorter derivation of the same expression.

The starting point for the derivation of the photocapacitance of an illuminated solar cell is the consideration of the continuity equations for electrons and holes

$$\frac{\mathrm{d}n}{\mathrm{d}t} = \frac{1}{q}\frac{\mathrm{d}J_\mathrm{n}}{\mathrm{d}x} + G - R \tag{6.1}$$

$$\frac{\mathrm{d}p}{\mathrm{d}t} = -\frac{1}{q}\frac{\mathrm{d}J_\mathrm{p}}{\mathrm{d}x} + G - R, \tag{6.2}$$

where p and n are the density of holes and electrons, J_p and J_n are the hole and electron currents, q represents the elementary charge, x refers to the distance from the left contact, G is the generation rate, and R is the recombination rate. In order to analytically solve these equations, some approximations are needed. First, we assume that diffusion is negligible so that the electron and hole currents are produced only by drift in the electric field, i.e.

$$J_\mathrm{n} = q\mu_\mathrm{n} n F \tag{6.3}$$

$$J_\mathrm{p} = q\mu_\mathrm{p} p F, \tag{6.4}$$

with F being the electric field and μ_n and μ_p the electron and the hole mobilities, respectively. Moreover, under steady state conditions and considering the case of negligible

recombination, the time derivatives in Eqs. (6.1) and (6.2) as well as the recombination rate R can be set to zero. Then, the substitution of Eqs. (6.3) and (6.4) into the continuity equations results in two expressions for the electron and hole densities

$$n = \frac{Gd^2}{\mu_{\mathrm{n}} \left(V_{\mathrm{bi}} - V\right)} \tag{6.5}$$

$$p = \frac{Gd^2}{\mu_{\mathrm{p}} \left(V_{\mathrm{bi}} - V\right)}, \tag{6.6}$$

where the electric field F has been expressed as a function of the difference between built-in voltage V_{bi} and applied voltage V. Now we consider a solar cell with the left contact acting as p-contact and the right contact acting as n-contact so that in absence of diffusion $n = 0$ at $x = 0$ and $p = 0$ at $x = d$, with d referring to the active-layer thickness. We can imagine to divide such a cell into two parts: the p-part, from $x = 0$ to $x = d/2$, where the hole density is higher than the electron density and the n-part, from $x = d/2$ to $x = d$, where the electron density is higher than the hole density. This procedure allows us to approximate the whole system as two plate capacitors connected in series whose capacitance values, $C_{\mathrm{ph,p}}$ and $C_{\mathrm{ph,n}}$ for the p-part and n-part respectively, can be calculated using Eqs. (6.5) and (6.6) along with the capacitance definition ($C = \mathrm{d}Q/\mathrm{d}V$)

$$C_{\mathrm{ph,n}} = \frac{qGd^3}{2\mu_{\mathrm{n}} \left(V_{\mathrm{bi}} - V\right)^2} \tag{6.7}$$

$$C_{\mathrm{ph,p}} = \frac{qGd^3}{2\mu_{\mathrm{p}} \left(V_{\mathrm{bi}} - V\right)^2}. \tag{6.8}$$

Finally, according to our approximation, the total photocapacitance C_{ph} of the solar cell is due to the series connection of these two plate capacitors and therefore is readily found to be

$$C_{\mathrm{ph}} = \frac{C_{\mathrm{ph,n}} \cdot C_{\mathrm{ph,p}}}{C_{\mathrm{ph,n}} + C_{\mathrm{ph,p}}} = \frac{qGd^3}{2\left(\mu_{\mathrm{p}} + \mu_{\mathrm{n}}\right)\left(V_{\mathrm{bi}} - V\right)^2}. \tag{6.9}$$

This expression for the photocapacitance is identical to the one derived by Crandall for a p-i-n amorphous silicon solar cell and, under certain circumstances, can also apply to organic solar cells. The derivation of Eq. (6.9) presented here, as well as the one followed by Crandall in Ref. [142], relies on three assumptions in order to be valid. The assumptions are that recombination has to be negligible, the photocurrent can be

approximated by a drift current (diffusion is neglected), and the electric field in the device is constant and equal to $(V_{\mathrm{bi}} - V)/d$. This means that space-charge effects due to, e.g., asymmetric mobilities [143–145], doping [45, 146, 147], or asymmetric contact barriers [125] would not be included in the theory. These effects would be more likely to matter in an organic solar cell of a given thickness than in an amorphous Si solar cell because the relative permittivity of the organic layers is small, and space charge has a stronger influence on the electric field. It is important to note that the breakdown of the assumptions of negligible recombination rate and constant electric field used in the derivation will be important later to explain deviations from Crandall's equation observed in experiment.

Equation (6.9) shows how the photocapacitance C_{ph} depends on the light intensity through the generation rate, the active-layer thickness, the built-in voltage, and the applied DC bias, as well as on the electron and hole mobilities. Thus, given the thickness of the active layer, the light intensity, and the effective electric field, the value of the capacitance due to illumination is uniquely determined by the mobilities μ_{n} and μ_{p}. This means that knowing the absorber thickness and the generation rate, it is possible to extract the mobility directly from capacitance-voltage measurements under illumination. Equation (6.9) can, in fact, be rewritten to emphasize the proportionality between the reciprocal of the square root of the photocapacitance and the applied bias V. Considering that the total measured capacitance C_{tot} is the sum of the photocapacitance C_{ph} and the dark capacitance C_{dark}, which includes the geometrical capacitance, we obtain a straight line from the data if we plot

$$\frac{1}{\sqrt{C_{\mathrm{ph}}}} = \frac{1}{\sqrt{C_{\mathrm{tot}} - C_{\mathrm{dark}}}} = \frac{\sqrt{4\mu}}{\sqrt{qGd^3}} \left(V_{\mathrm{bi}} - V\right) \tag{6.10}$$

versus the applied DC bias; the slope of this line can then be used to estimate the average charge-carrier mobility μ. When the same capacitance-voltage measurement is performed under different light intensities, the plot of $(C_{\mathrm{tot}} - C_{\mathrm{dark}})^{-1/2}$ versus the applied bias can be replaced by the plot of $(C_{\mathrm{ph,norm}})^{-1/2}$ versus the applied bias, where the thickness and generation-rate-normalized photocapacitance is defined as

$$C_{\mathrm{ph,norm}} = \frac{4C_{\mathrm{ph}}}{qGd^3}. \tag{6.11}$$

This definition of $C_{\mathrm{ph,norm}}$ is pretty convenient because, according to Eq. (6.10), the $(C_{\mathrm{ph,norm}})^{-1/2} - V$ plot should lead to a series of overlapping straight lines whose slope can be used to determine the charge-carrier mobility.

6.3 Comparison between Models to Extract the Capacitance from the Total Impedance

Before presenting the experimental results, it is important to stress the fact that when a capacitance-voltage measurement is performed, the quantity recorded as function of voltage is the total impedance of the device at a certain frequency from which the capacitance can later be extracted. In order to analyze measurements done as function of voltage at a single frequency, the device under investigation has to be modeled with a simple equivalent circuit consisting of a resistor and a capacitor. In principle there are two ways to connect these two elements: in series, which we call the $\mathrm{C_sR_s}$ mode, or in parallel, which we call $\mathrm{C_pR_p}$ mode. At reverse bias or short circuit, i.e. in the voltage range where we mostly analyze our data, the resistance of the diode in parallel to the capacitor C is large and certainly not negligible relative to C. Thus, the $\mathrm{C_pR_p}$ mode is surely the more sensible mode for the analysis of capacitance-voltage measurements. However, the use of the $\mathrm{C_sR_s}$ mode leads, especially under illumination, to quite peculiar results that are relevant to the analysis of C-V measurements. Therefore, in the following, we will briefly sketch how these two different modes lead to different values for the resulting capacitance.

In the $\mathrm{C_sR_s}$ mode the total impedance $Z_{\mathrm{s,tot}}$ is simply the sum of the impedance of the resistor Z_{R} and the impedance of the capacitor Z_{C} ($Z_{\mathrm{s,tot}} = Z_{\mathrm{R}} + Z_{\mathrm{C}}$), while in the $\mathrm{C_pR_p}$ mode the inverse of $Z_{\mathrm{p,tot}}$ is equal to the sum of the inverse of Z_{R} and the inverse of Z_{C} ($1/Z_{\mathrm{p,tot}} = 1/Z_{\mathrm{R}} + 1/Z_{\mathrm{C}}$). Thus, in the former case the capacitance C_{s} can be calculated from the imaginary part of the total impedance $Z_{\mathrm{s,tot}}$ via

$$\mathrm{Im}\,(Z_{\mathrm{s,tot}}) = -\frac{1}{\omega C_{\mathrm{s}}} \tag{6.12}$$

and in the latter case the capacitance C_{p} from the imaginary part of the total impedance

$Z_{\mathrm{p,tot}}$

$$\mathrm{Im}\left(Z_{\mathrm{p,tot}}\right) = -\frac{\omega C_{\mathrm{p}} R_{\mathrm{p}}^2}{1+\omega^2 C_{\mathrm{p}}^2 R_{\mathrm{p}}^2}, \tag{6.13}$$

where $\omega = 2\pi f$ is the angular frequency and R_{p} the value of the resistor connected in parallel with the capacitor C_{p}. The two analysis modes normally provide different capacitance values, as shown in Fig. 6.2 which presents the C–V characteristics and C^{-2}–V characteristics (Mott-Schottky plot) obtained calculating the capacitance from the exact same impedance data resulting from the measurement of a PBDTTT-C: $PC_{71}BM$ (1:1.5 wt%) sample. The difference between the two modes particularly stands

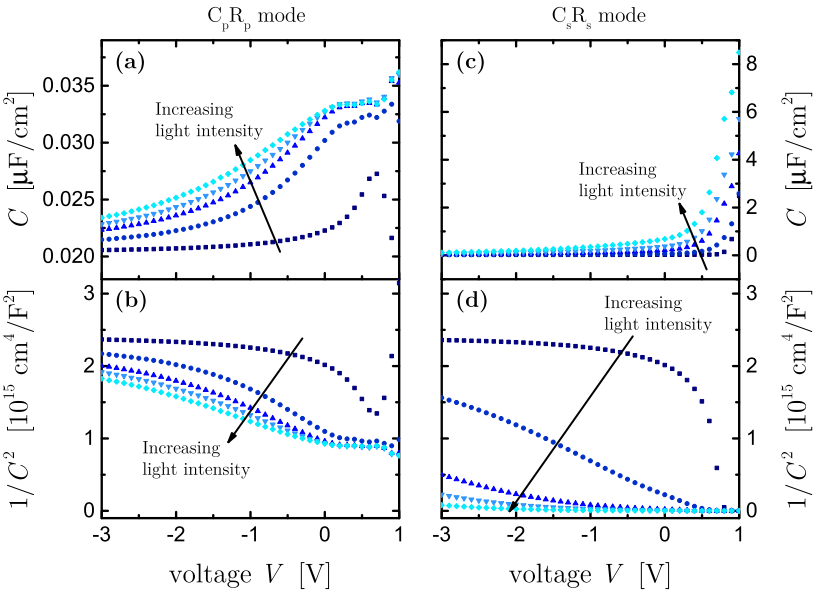

Figure 6.2: (a,c) Capacitance C and (b,d) C^{-2} versus applied bias for different light intensities (dark, 0.2, 0.5, 0.7, and 1 sun) obtained measuring a PBDTTT-C:$PC_{71}BM$ (1:1.5 wt%) device. The panels on the left (a, b) show the case where a capacitor in parallel with a resistor was used to evaluate the impedance data, while the panels on the right (c, d) show the case where a resistor in series with a capacitor was used. The data obtained from the two modes differ drastically, especially with respect to their light-intensity dependence.

out when looking at Figs. 6.2(a) and 6.2(c) which have a y-axis scale that differs by

two orders of magnitude and when considering their light-intensity dependence. In particular, the Mott-Schottky plot in C_pR_p mode (Fig. 6.2(b)) is much less affected by the amount of illumination than the Mott-Schottky plot in C_sR_s mode (Fig. 6.2(d)). In this latter case, the use of the standard Mott-Schottky analysis to calculate the built-in voltage from data obtained under illumination leads to V_{bi} values which are much lower than the value obtained in the dark and may even be negative for high light intensities, as shown by Guerrero et al. [139] and Bisquert et al. [138].

Equating the right-hand sides of Eqs. (6.12) and (6.13) and solving for C_s leads to

$$C_s = \frac{1}{\omega^2 C_p R_p^2} + C_p. \tag{6.14}$$

Thus, according to Eq. (6.14), the difference between the capacitance C_s derived using the C_sR_s mode and the capacitance C_p derived using the C_pR_p mode mostly depends on the value of the resistance R_p. This value is not constant but depends on the light intensity: the higher the light intensity, the smaller R_p is. This means that when the light intensity is increased, R_p changes as well becoming smaller and, consequently, the difference between C_s and C_p gets bigger. This tendency is also shown in Fig. 6.2 where it is evident that the difference between C_s and C_p becomes larger as the light intensity is increased, while it approaches zero in the case of measurements performed in the dark and under reverse bias. Since the C_pR_p mode is physically more meaningful than the C_sR_s mode, we chose to use it for the analysis of impedance data and, therefore, all the following presented capacitance data are obtained with the C_pR_p analysis mode.

6.4 Results and Discussion

In order to test the validity of Eq. (6.9), capacitance-voltage measurements in the dark and as a function of light intensity were performed at a fixed frequency of 5 kHz on solar cells composed of PTB7 blended with $PC_{71}BM$ and solar cells composed of PBDTTT-C blended with $PC_{71}BM$. All the devices were fabricated with the inverted architecture glass/ITO/ZnO/polymer:$PC_{71}BM$/MoO_3/Ag following the procedure described in section 4.2. The resulting PTB7 based devices were 190 nm thick, while the PBDTTT-C based devices were 170 nm thick. Figure 6.3(a) shows the plot of $(C_{ph,norm})^{-1/2}$ versus applied bias for different light intensities (0.2, 0.5, 0.7, and 1 sun) obtained measuring

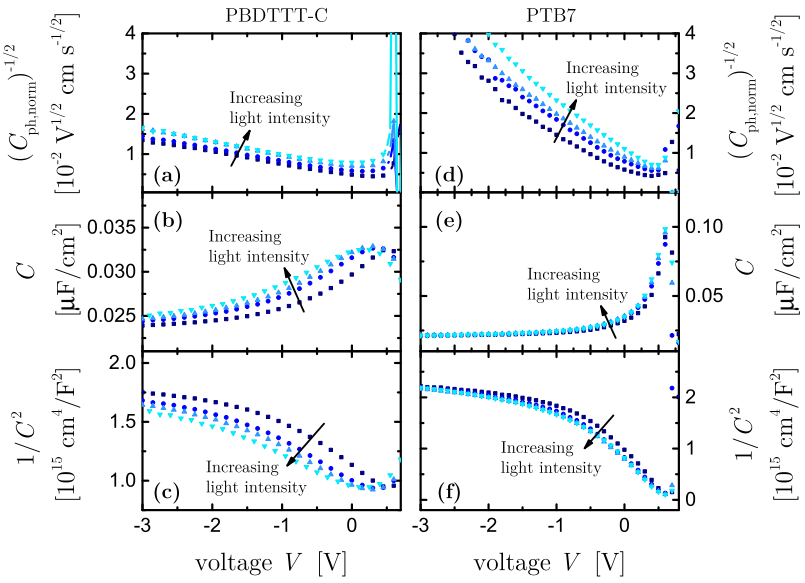

Figure 6.3: Capacitance-voltage measurements of (a)-(c) a PBDTTT-C:$PC_{71}BM$ (1:1 wt%) solar cell and (d)-(f) a PTB7:$PC_{71}BM$ (1:1.5 wt%) solar cell as function of light intensity (0.2, 0.5, 0.7, and 1 sun). In the case of the PBDTTT-C:$PC_{71}BM$ device, the curves of $(C_{ph,norm})^{-1/2}$ versus the applied voltage shift to more positive voltage as the light intensity increases. However, they remain parallel allowing the extraction of the mobility from their slope. The peak in C-V characteristics becomes more left shifted and the C^{-2} curves shift to more negative voltage as the light intensity increases. In the case of the PTB7:$PC_{71}BM$ device the shift of the peak in C-V characteristics and the shift of the C^{-2} curves are less pronounced and the curves of $(C_{ph,norm})^{-1/2}$ versus the applied voltage slightly move to more positive voltage as the light intensity increases.

the PBDTTT-C based device, whereas Fig. 6.3(d) shows the same plot for the PTB7 based device. It can be seen that in both cases the lines corresponding to the different light intensities are not overlapping as predicted by Eq. (6.10). However, all the lines are parallel, indicating that the mobility values extracted from the linear fit remain roughly the same as a function of light intensity. The charge-carrier mobility for the PBDTTT-C-based device extracted from the curves in Fig. 6.3(a) considering $J_{sc} \approx qGd$ for the calculation of the generation rate G, exhibits a nearly constant value equal to 1.24×10^{-5}

+/– 1.3×10^{-6} cm^2/Vs, which is in agreement with literature values for the mobilities measured with other techniques such as charge extraction by linearly increasing voltage (CELIV) [108] and simple charge extraction [148]. On the other hand, the mobility for the PTB7:$PC_{71}BM$ sample extracted from the curves in Fig. 6.3(d) presents a nearly constant value of 1.25×10^{-4} +/– 3.9×10^{-5} cm^2/Vs which is in good agreement with the literature values measured with other methods such as open-circuit-corrected charge-carrier extraction (OTRACE) [149] and time of flight [150].

The possibility to estimate the mobility even in the case of parallel lines was verified by means of numerical simulations performed using the software SCAPS. However, it is important to note that when the mobilities are asymmetric (and at least one is fairly low), the value extracted using this method is much closer to the value of the lowest mobility than to the average mobility. The same simulation resulting in parallel $(C_{\mathrm{ph,norm}})^{-1/2}$-$V$ curves was performed using a constant generation rate and a real generation profile created with the software ASA and its built-in transfer matrix code *genpro1* together with the optical data displayed in Fig. 6.4. The results of these simulations

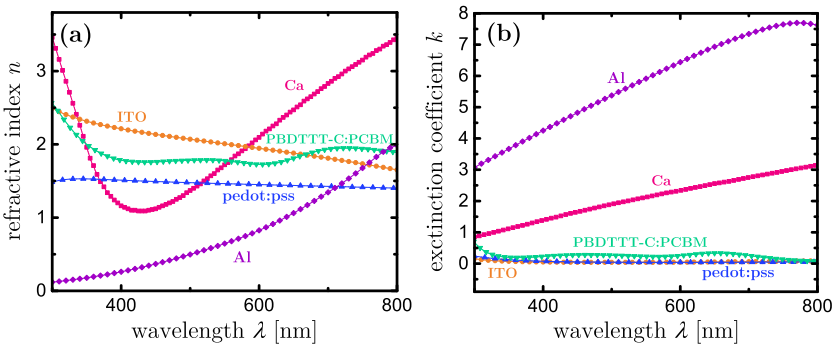

Figure 6.4: Refractive index n and extinction coefficient k of the simulated device materials utilized to create the generation profile with ASA [128, 130].

are visible in Fig. 6.5 which displays the ratio between the mobility μ_{sim} calculated using Eq. (6.10) and the real value μ_{real} of the lowest mobility set for the simulations as a function of light intensity for a 150 nm-thick device (Fig. 6.5(a)) and a 240 nm-thick device (Fig. 6.5(b)), both with unbalanced mobilities ($\mu_{\mathrm{p}} = 5\times10^{-5}$ cm^2/Vs, $\mu_{\mathrm{n}} = 5\times10^{-4}$ cm^2/Vs). For the thin device (Fig. 6.5(a)) the mobility values calculated both

from the simulations with the constant generation rate and with a real generation profile do not change with the light intensity. On the other hand, when a thicker device is considered (Fig. 6.5(b)), the mobility values obtained from the simulations with a real generation profile evidently increase as the light intensity is increased and the mobility values calculated from the simulations with the constant generation rate only slightly change with the light intensity. However, for both devices the μ_{sim}/μ_{real} ratio does not exceed 1.45 indicating the possibility to estimate the value of the lowest mobility from the plot of $(C_{ph,norm})^{-1/2}$ versus voltage even if the lines corresponding to the different light intensities are not overlapping but parallel.

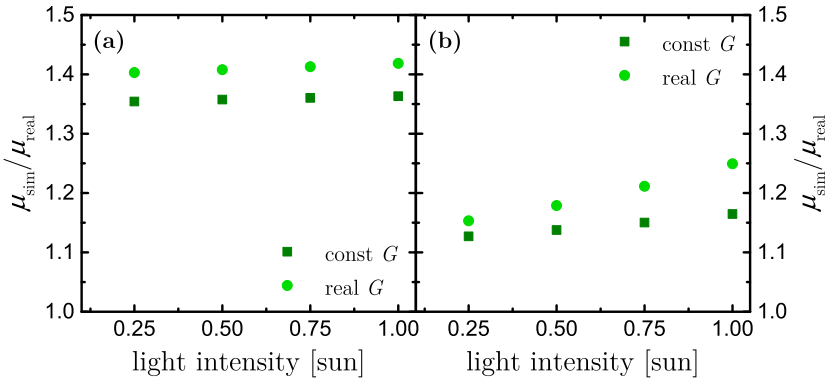

Figure 6.5: Ratio between the mobility μ_{sim} calculated using Eq. (6.10) and the real value μ_{real} of the lowest mobility set for the simulations as function of light intensity for (a) a 150 nm-thick device and (b) a 240 nm-thick device, both with unbalanced mobilities ($\mu_p = 5\times10^{-5}$ cm^2/Vs, $\mu_n = 5\times10^{-4}$ cm^2/Vs). Squares refer to the simulations performed using a constant generation rate and circles to the simulations performed with a real generation profile created with the software ASA. For both devices the μ_{sim}/μ_{real} ratio does not exceed 1.45 indicating the possibility to estimate the value of the lowest mobility from the $(C_{ph,norm})^{-1/2}$ -V plot even in the case of parallel lines.

In order to gain insight into the behavior leading to the presence of parallel lines in Figs. 6.3(a) and 6.3(d), the C-V characteristics under illumination were analyzed (Figs. 6.3(b), 6.3(c), 6.3(e), and 6.3(f)). In Figs. 6.3(b) and 6.3(e), the capacitance C is plotted as a function of the applied bias for different light intensities. The behavior of the device capacitance is the typical behavior observed in solar cells and features two main regions: at forward bias, the capacitance increases exponentially with voltage due

to the injection of electrons and holes from their respective contacts [33, 151]; towards reverse bias, the value of C decreases and slowly approaches the value given by the geometrical capacitance for infinitely low light intensities and high reverse biases [138]. In addition to these two main regions, in the C-V characteristics obtained measuring the PBDTTT-C based device we detect a peak, which becomes more evident and shifts to lower voltages as the light intensity increases. This systematic shift is equally evident in the plot of C^{-2} versus voltage presented in Fig. 6.3(c).

The reason for this behavior is found in the asymmetry of the system considered and the consequent nonuniform electric field. Usually, it is possible to make a useful approximation by assuming that the electric field is nearly uniform in the active layer and equal to $(V_{\mathrm{bi}} - V)/d$. However, there are some cases where the electric field is highly nonuniform, for instance when the device is highly doped or when the cell thickness increases and the charge transport is strongly unbalanced. Also traps in the material, asymmetric contact barriers at the anode or cathode, or any combination of the mentioned reasons could lead to nonuniform electric fields which have implications on current-voltage [152, 153] and capacitance-voltage [154] characteristics. The case with a sufficiently high doping concentration would mean that the cell shows Mott-Schottky type behavior both in the dark and under illumination. This situation is represented in Fig. 6.6 which displays the plot of C^{-2} versus voltage at different light intensities for a simulated 240 nm-thick and highly doped ($N_{\mathrm{A}} = 5{\times}10^{17}$ cm^{-3}) solar cell with unbalanced mobilities ($\mu_{\mathrm{p}} = 5{\times}10^{-5}$ cm^2/Vs, $\mu_{\mathrm{n}} = 5{\times}10^{-4}$ cm^2/Vs). Here, the C^{-2}-V curves are straight lines over the entire voltage range considered, independently of the light intensity, and, therefore, make it possible to derive the doping density and the built-in voltage from this kind of plot even under illumination. Clearly the solar cells studied here do not show this kind of behavior; therefore, we chose to have a look at one of the other cases that can lead to nonuniform electric fields.

For more detailed simulations, we chose as example the case of high cell thickness and unbalanced charge transport ($\mu_{\mathrm{n}} \neq \mu_{\mathrm{p}}$). If one considers a semiconductor where the hole drift length is much smaller than the electron drift length and which has a sufficiently high active-layer thickness ($d > 200$ nm) [32], the holes will accumulate in the device under illumination. As a consequence, the electric field increases in the region near the anode, enhancing the extraction of holes, and decreases in the region near the cathode, diminishing the extraction of electrons [143]. That means that the assumption

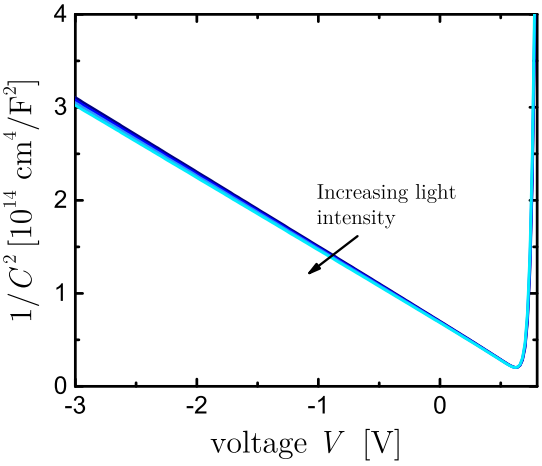

Figure 6.6: Plot of C^{-2} versus voltage as a function of light intensity obtained from the simulations of a 240 nm-thick and highly doped ($N_A = 5\times10^{17}$ cm^{-3}) solar cell with unbalanced mobilities ($\mu_p = 5\times10^{-5}$ cm^2/Vs, $\mu_n = 5\times10^{-4}$ cm^2/Vs). Over the entire voltage range considered the solar cell shows a straight Mott-Schottky plot independently of the light intensity, which allows the derivation of the doping density and the built-in voltage even under illumination.

of constant electric field used to derive the photocapacitance equation (Eq. (6.9)) breaks down. Since almost the entire voltage V drops over the region of hole accumulation, the energy-band diagram shows a parabolic trend, as it is schematically represented in Fig. 6.7 illustrating the simulated band diagram of a 200 nm-thick intrinsic solar cell with asymmetric mobilities ($\mu_p<\mu_n$) under 1-sun illumination at 0 V (short-circuit conditions). The accumulated holes in the region near the anode cause the formation of positive space charge which limits the photocurrent generated by the device, i.e. the initial assumption that recombination at short circuit or reverse bias is negligible breaks down. In this space-charge-limited regime, the length L of the current-limiting layer and the maximum electrostatically allowed photocurrent J_{ph} that can be extracted from the device are, respectively [143],

$$L = \left(\frac{9\varepsilon_0\varepsilon_r \min(\mu_p, \mu_n)}{8qG}\right)^{1/4} V^{1/2} \tag{6.15}$$

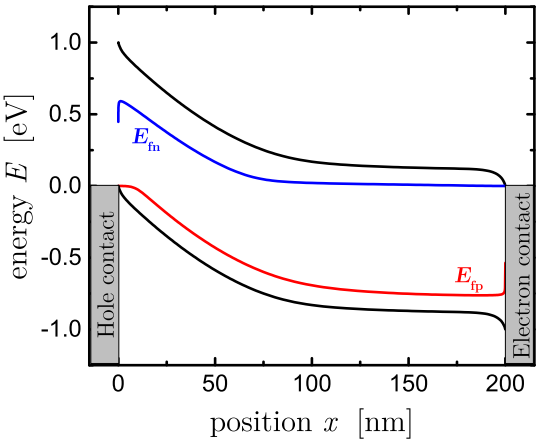

Figure 6.7: Band diagram under 1-sun illumination and short-circuit conditions of a simulated intrinsic solar cell with 200 nm-thick active layer and asymmetric mobilities ($\mu_p = 5{\times}10^{-5}$ cm^2/Vs, $\mu_n = 5{\times}10^{-4}$ cm^2/Vs). The band's bending suggests the presence of a nonuniform electric field inside the active layer. In fact, the holes will accumulate to a greater extent in the device than the electrons, which makes the electric field increase in the region near the anode and decrease in the region near the cathode.

$$J_{ph} = q\left(\frac{9\varepsilon_0\varepsilon_r \min(\mu_p, \mu_n)}{8q}\right)^{1/4} G^{3/4} V^{1/2}. \tag{6.16}$$

By assuming that the capacitance scales with the reciprocal of the length L of the current-limiting layer, it follows that in the space-charge-limited regime the photocapacitance of the solar cell scales with $G^{1/4}$. Moreover, according to Eq. (6.15), the photocapacitance also varies inversely with the square root of the voltage, as in a Schottky barrier. On the other hand, when the length L of the current-limiting layer becomes equal to the device thickness d, the photocurrent saturates to the value of $J_{ph} = qGd$. Under this condition, the electric field can be again considered uniform in the whole active layer and the expression derived for the photocapacitance is equal to the one presented in Eq. (6.9). Only in the saturation region, the photocurrent is at its maximum value, i.e. recombination can be neglected, and the photocapacitance follows Crandall's equation. Thus, when the photocurrent switches from the space-charge-limited regime to the saturation regime, the photocapacitance dependence on the voltage changes consequently. Taking into account that the transition between

the two photocurrent regimes takes place when the space-charge-limited photocurrent is equal to the saturation photocurrent, the voltage V_{p} at which J_{ph} changes can be determined via

$$V_{\mathrm{p}} = \frac{G^{1/2} d^2}{\left(\frac{9\varepsilon_0 \varepsilon_{\mathrm{r}} \min(\mu_{\mathrm{p}}, \mu_{\mathrm{n}})}{8q}\right)^{1/2}}. \tag{6.17}$$

Since from Eq. (6.17) it becomes clear that the voltage at which J_{ph} changes depends on the light intensity, it is reasonable to expect that the position of the peak in the C-V characteristic, which underlines the change of the photocapacitance dependence on the voltage, varies as well moving towards more negative voltages as the light intensity increases. This behavior can be distinctly observed in Figs. 6.8(a) and 6.8(b) which show, respectively, the simulated J_{ph}-$(V_0 - V)$ and C-V characteristics of a simulated intrinsic solar cell with unbalanced mobilities (μ_{p}<μ_{n}). Here, V_0 refers to the compensation voltage, i.e. the voltage at which $J_{\mathrm{ph}} = 0$. In these figures, the transition between the two regions is underlined by a change in the slope in the simulated J_{ph}-$(V_0 - V)$ characteristics and by a peak in the simulated C-V characteristics. As the light intensity is increased, the voltage V_{p} at which the transition occurs decreases. The same trend, even if less marked, can be detected in Figs. 6.8(c) and 6.8(d) showing, respectively, the J_{ph}-$(V_0 - V)$ and C-V characteristics of a 150 nm-thick PBDTTT-C: $PC_{71}BM$ (1:1 wt%) device, i.e. a device with a non-ideal donor-acceptor ratio [148]. However, in this case the active layer is thinner than the one set for the simulations; therefore the current-limiting region L becomes equal to the device thickness d already at forward bias and the photocurrent almost immediately saturates to its maximum value.

The results presented in Fig. 6.8 confirm that the presence of asymmetric mobilities can lead to C-V characteristics with features resembling the ones observed in the C-V characteristics of the devices studied here. It is important to note, however, that it is not possible to assign the trends in experimental data where C-V curves shift with illumination to, e.g., asymmetric mobilities. The shifts in the capacitance-voltage curves with light intensity are indeed due to violations of the assumptions needed to derive Crandall's theory, specifically Eq. (6.9), and asymmetric and low mobilities are only one of several explanations that cannot be easily distinguished without substantial further efforts. For instance, asymmetric contact barriers at the anode or cathode have, on the charge-carrier extraction, effects analogous to the ones caused by unbalanced charge

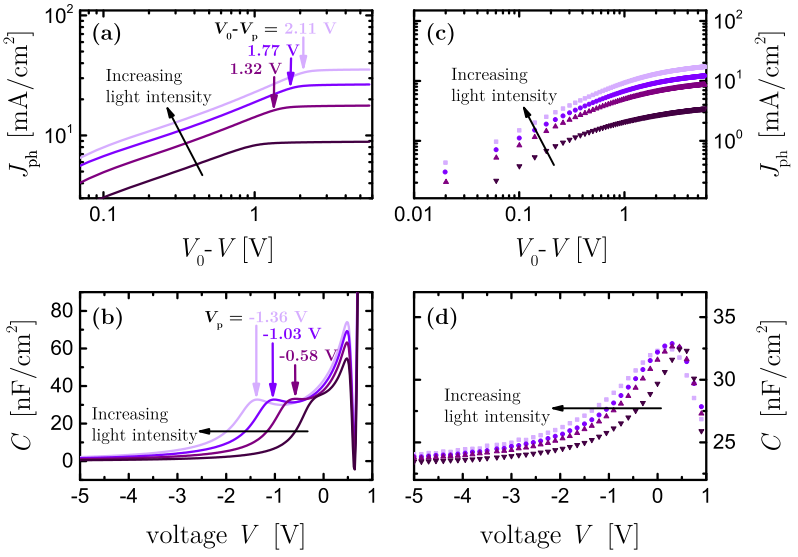

Figure 6.8: Graphs showing the J_{ph}-$(V_0 - V)$ characteristics and C-V characteristics obtained (a) and (b) from the simulations of an intrinsic solar cell with a 200 nm-thick active layer and unbalanced mobilities ($\mu_p = 5\times10^{-5}$ cm^2/Vs, $\mu_n = 5\times10^{-4}$ cm^2/Vs) and (c) and (d) from measuring a 150 nm-thick PBDTTT-C:$PC_{71}BM$ (1:1 wt%) device. The change in the slope of J_{ph}-$(V_0 - V)$ curves underlines the transition from the space-charge-limited regime to the saturation regime. As the arrows indicate, the voltage V_p corresponding to this transition decreases as the light intensity increases. The peak in C-V curves shifts towards more negative voltages as the light intensity is increased and, therefore, the voltage V_p decreases consequently like the arrows point out.

transport, i.e. they lead to a nonuniform electric field and, consequently, to a shift in the plot of C versus voltage and C^{-2} versus voltage. It is also worth highlighting the fact that the simultaneous presence of asymmetric contact barriers and asymmetric mobilities can result in a situation where their effects cancel each other out, yielding better adherence to the assumptions of Crandall's theory. These observations are confirmed by the results presented in Fig. 6.9, which shows the C-V and C^{-2}-V characteristics obtained from the simulations at different light intensities (dark, 0.2, 0.5, 0.7, and 1 sun) of an intrinsic solar cell with a 100 nm-thick active layer and asymmetric contact

barriers ($\varphi_a > \varphi_c$). When the hole and electron mobilities are equal (Figs. 6.9(a) and 6.9(c)), the asymmetric contact barriers produce a non-constant electric field inside the solar cell, which is the cause of the shift of C-V and C^{-2}-V curves as the light intensity increases. By having both asymmetric barriers and asymmetric mobilities (Figs. 6.9(b) and 6.9(d)) it is possible to reduce the shifts because the asymmetric mobilities ($\mu_p > \mu_n$) compensate the effect of the asymmetric contact barriers.

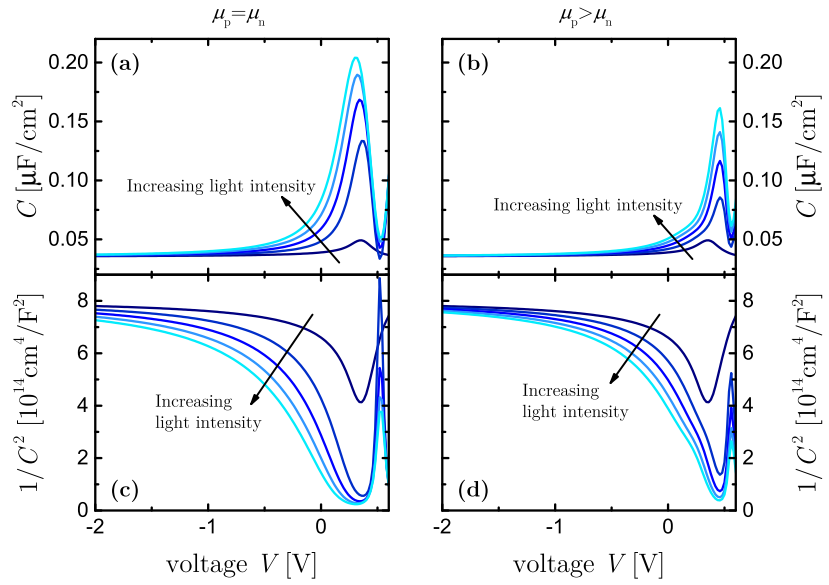

Figure 6.9: C-V characteristics and C^{-2}-V characteristics obtained from the simulations at different light intensities (dark, 0.2, 0.5, 0.7, and 1 sun) of an intrinsic solar cell with a 100 nm-thick active layer and asymmetric contact barriers ($\varphi_a > \varphi_c$). (a) and (c) are obtained setting equal mobilities for electrons and holes while (b) and (d) with asymmetric mobilities ($\mu_p > \mu_n$). When $\mu_p = \mu_n$, the asymmetric contact barriers produce a non-constant electric field inside the solar cell which is the cause of the shift of C-V curves as the light intensity increases. On the other hand, with asymmetric mobilities ($\mu_p > \mu_n$) it is possible to compensate the effect of the asymmetric contact barriers and consequently reduce the shift of C-V curves.

In conclusion, the purpose of Fig. 6.8 is only to show that asymmetric mobilities are one possible explanation to the trends observed in experimental data and not to

suggest that they are the (most likely) explanation for the data in Fig. 6.3 or any other data where the C-V curves shift with illumination.

6.5 Conclusions

The features observed in capacitance-voltage measurements under illumination on fully depleted organic solar cells were explained with a combination of the charge-carrier mobility and the photogenerated space charge in the device. Provided that the device is sufficiently thin and not affected by a high doping concentration, the C-V curves can be approximately described by a theory of photocapacitance developed by Crandall for amorphous silicon solar cells. Through the application of this theory it is possible to extract the charge-carrier mobility from C-V measurements that, thus, become a potential complimentary method to other techniques for the determination of doping density and mobility. The differences between the theory of Crandall and the experimental results were assigned to the breaking down, in certain practical cases, of the assumptions required to derive the photocapacitance equation. Additionally, an explanation of why the apparent built-in voltage that would be obtained from Mott-Schottky plots under illumination is often substantially lower than the built-in voltage obtained in the dark was given. This initially surprising result can be either attributed to the capacitance originating from photogenerated charge carriers that can build up in low-mobility materials even at reverse bias or from using an inappropriate equivalent circuit for data analysis.

Chapter 7

Deriving the Charge-Carrier Lifetime from the Capacitance under Illumination

While the previous chapter focused on the capacitance-voltage measurements performed on fully depleted organic solar cells, this chapter presents an analysis of the capacitance of a partly depleted device under illumination and short-circuit conditions considering the effect of recombination and space-charge region. Since capacitance relates to charge-carrier accumulation and distribution in the device, the determination of the charge-carrier density in the neutral region of such device is addressed by discussing three different analytical models and their validity range in terms of diffusion length and absorption coefficient. The derived relation between charge density, capacitance under illumination, and charge-carrier lifetime is then used to highlight the possibility of extracting the lifetime from capacitance data at short circuit. Finally, it is shown that the methods used to derive the charge-carrier mobility and the charge-carrier lifetime from capacitance-voltage data under illumination require diametrically opposite conditions in terms of doping density and absorber-layer thickness.

7.1 Introduction

We already highlighted the importance of the sample properties and the measurement conditions when choosing a method to analyze capacitance-voltage curves. The analysis methods for C-V measurements performed in the dark on devices both partially and fully depleted are already well established and allow to gain information on the density

of states or the doping concentration, thanks to the Mott-Schottky analysis. On the other hand, the analysis of capacitance-voltage measurements under illumination has so far not attracted much attention in the literature. While the previous chapter focused on *C-V* measurements performed at reverse bias and under illumination on fully depleted organic solar cells with negligible recombination, the present chapter addresses the case of illuminated devices at short circuit with an absorber layer only partly depleted (condition highlighted in Table 7.1). In such a case, a well defined space-charge region exists in the device and the recombination of charge carriers cannot be neglected, which makes the method presented in the previous chapter inapplicable.

Table 7.1: Information accessible through the analysis of capacitance-voltage data depending on the sample properties and the measurement conditions.

	$w < d$	$w \approx d$
DARK	at $V \leq 0$ space-charge capacitance provides the doping density	at $V > 0$ chemical capacitance related to the density of states
LIGHT	at $V = 0$ to be discussed here	at $V \leq 0$ photocapacitance provides the charge-carrier mobility (see chapter 6)

7.2 Photocapacitance at Short Circuit

An analysis of the photocapacitance, i.e. the capacitance under illumination, of a silicon solar cell under short-circuit conditions was already presented in 1975 by Moore [155], who emphasized the strong relation between the charge density in a device and its capacitance. For seek of completeness, we will recall here part of the arguments presented by Moore to derive the expression of the short-circuit capacitance as function of the maximum minority-carrier concentration in the absorber layer of a partly depleted device under illumination.

To illustrate the concept we look at a simple device composed by a *p*-type absorber layer sandwiched between the left electron contact and the right hole contact and we

consider as starting point the expression for the charge density $n(x) = \alpha\phi\tau_{\mathrm{n}}\left(1 - e^{-\frac{x-w}{L_{\mathrm{n}}}}\right)$ presented in Moore's work. Here, L_{n} represents the electron diffusion length, τ_{n} the electron lifetime, α the absorption coefficient, and ϕ the incident monochromatic photon flux. For a p-type absorber layer in contact with an electron injecting contact, the space-charge region width w can then be expressed as

$$w = \sqrt{\frac{2\varepsilon_0\varepsilon_{\mathrm{r}}\left(V_{\mathrm{bi}} - V\right)}{qN_{\mathrm{A}}}}, \tag{7.1}$$

where V_{bi} is the built-in voltage, V the applied DC bias, q the elementary charge, N_{A} the doping density, and ε_0 and ε_{r} are respectively the vacuum and the relative permittivity. When the voltage V is decreased, the width of the space-charge region increases, its edge moves by the quantity $\mathrm{d}w$, and an electron charge $\mathrm{d}Q$ is swept out from the device; this results in a new electron distribution $n_2(x) = n_1(x - \mathrm{d}w)$ where $n_1(x)$ is a steady-state solution with $n_1(w) = 0$. This behavior is schematically illustrated in Fig. 7.1 which presents the energy-band diagram and the electron distribution before (Figs. 7.1(a) and 7.1(c)) and after (Figs. 7.1(b) and 7.1(d)) the increment of the space-charge region width by the quantity $\mathrm{d}w$. The shaded area to the left in Fig. 7.1(d) corresponds to the change in charge $\mathrm{d}Q$ when the new electron distribution $n_2(x)$ arises as consequence of the increment $\mathrm{d}w$ in the depletion region width. This area is equal to the shaded area to the right which represents a virtual increase of the absorber layer thickness d by the quantity $\mathrm{d}w$ for the new electron distribution $n_2(x)$. The electron charge $\mathrm{d}Q$ can then be calculated as

$$\mathrm{d}Q = q\int_w^d n_1(x)\mathrm{d}x - q\int_w^d n_1\left(x - \mathrm{d}w\right)\mathrm{d}x, \tag{7.2}$$

with d being the absorber-layer thickness. Under the assumptions $d \gg L_{\mathrm{n}}$ and $dw \ll L_{\mathrm{n}}$, Eq. (7.2) yields

$$dQ = q\alpha\phi\tau_{\mathrm{n}}\mathrm{d}w = q\hat{n}\mathrm{d}w, \tag{7.3}$$

where $\hat{n} = \alpha\phi\tau_{\mathrm{n}}$ represents the maximum steady-state electron concentration in the neutral region of the absorber layer. The influence of lifetime on $\mathrm{d}Q$ and $n(x)$ is well represented in Fig. 7.2 which displays, for different values of the lifetime τ_{n}, the electron distributions $n_1(x)$ and $n_2(x)$ inside the absorber layer respectively before and after the increment of the space-charge region by the quantity $\mathrm{d}w$, and the corresponding change in charge $\mathrm{d}Q$. As the lifetime is increased, the amount of charge carriers present in the

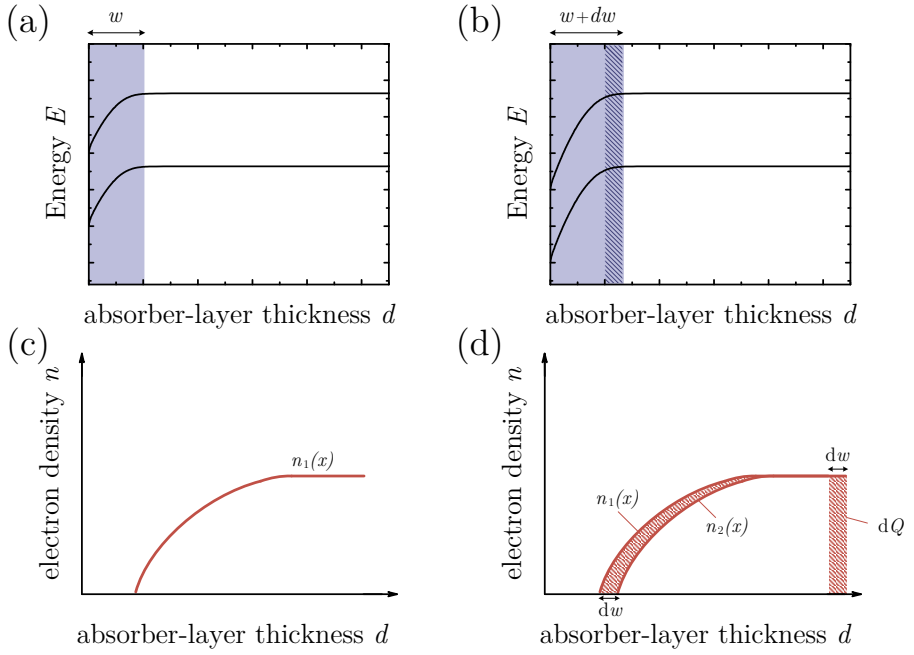

Figure 7.1: Schematic illustration of the changes in the band diagram (a)-(b) and electron distribution (c)-(d) resulting from the increment dw in the space-charge region width.

absorber layer accordingly grows and consequently also dQ increases. It is known that the total capacitance per area C_{tot} of a device under illumination is greater than the capacitance per area C_{dark} measured in the dark: $C_{\text{tot}} = C_{\text{dark}} + C_{\text{ph}}$, with C_{ph} being the photocapacitance. In our case, the dark capacitance of the device corresponds to the space-charge capacitance ($C_{\text{dark}} = \varepsilon_0 \varepsilon_{\text{r}} / w$) and is proportional to the increment in the space-charge region width due to a small voltage change

$$\frac{C_{\text{dark}}}{qN_A} = \frac{\mathrm{d}w}{\mathrm{d}V}. \tag{7.4}$$

By using Eqs. (7.3) and (7.4) the additional capacitance under illumination, i.e. the

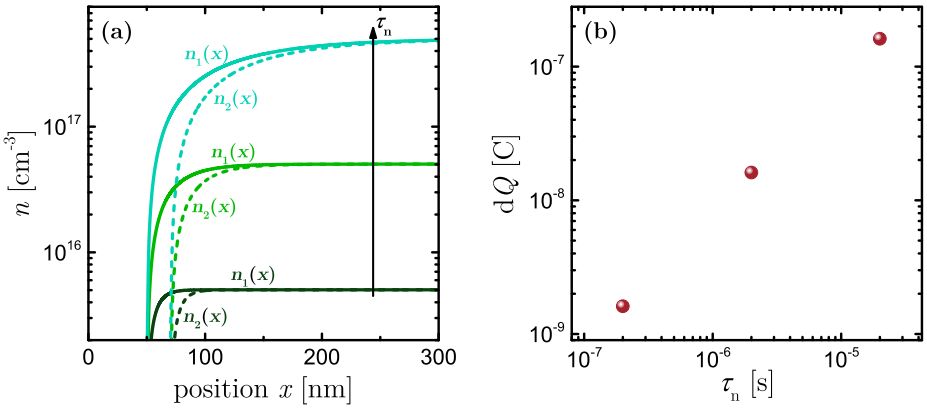

Figure 7.2: Electron distribution $n(x)$ and change in the charge dQ for different values of the lifetime τ_n. (a) electron distribution $n_1(x)$ before and $n_2(x)$ after the increment of the space-charge region by the quantity dw; (b) change in the charge dQ as a function of the electron lifetime.

photocapacitance C_{ph}, at short circuit can then be determined via

$$C_{ph} = \frac{dQ}{dV} = q\hat{n}\frac{dw}{dV} = \hat{n}\frac{C_{dark}}{N_A}, \tag{7.5}$$

which coincides with the additional short-circuit capacitance during illumination derived by Moore.

Equation (7.5), which points out the proportionality between the photocapacitance and the dark capacitance, may be rewritten to highlight instead the relation between C_{ph}, C_{dark}, and τ_n

$$\hat{n} = \alpha\phi\tau_n = \frac{C_{ph}}{C_{dark}}N_A. \tag{7.6}$$

The former equation elucidates in fact more clearly how the photocapacitance, the dark capacitance, the doping density, and the maximum generation rate in absence of reflection of photons at the surface ($G_{max} = \alpha\phi$) relate to the charge-carrier lifetime of minority carriers in the neutral zone of the absorber layer. Thus, if the dark capacitance, the doping density, and the maximum generation rate are determined separately, the measurement of the capacitance under illumination and short-circuit conditions of a partially depleted device should be sensitive to the charge-carrier lifetime and therefore

allow its determination. Note that this situation is substantially different from the one arising in a fully depleted device under illumination, where the photocapacitance at reverse bias is mostly affected by the charge-carrier mobility, as discussed in chapter 6.

7.3 Determination of the Charge Density at Short Circuit

A prerequisite to make use of Eq. (7.6) is identifying the conditions under which the assumptions used for its derivation are valid. The expression of the charge density used by Moore as starting point, i.e. $n(x) = \alpha\phi\tau_{\mathrm{n}}\left(1 - e^{-\frac{x-w}{L_{\mathrm{n}}}}\right)$, describes indeed a very special case and does not represent the general expression for $n(x)$ in an illuminated device which is only partly depleted. For a comprehensive coverage of the different cases, more general equations paired with numerical simulations are therefore needed.

For the analysis of the charge density present in the active layer of a partly depleted device at short circuit and under illumination, i.e. the condition highlighted in Table 7.1, we choose as reference a device with a relatively thick absorber layer ($d = 300$ nm) and a relatively high doping density ($N_{\mathrm{A}} = 5 \times 10^{16}$ cm^{-3}). Figure 7.3 presents the energy-band diagram at short circuit obtained simulating a device with the aforementioned characteristics ($d = 300$ nm and $N_{\mathrm{A}} = 5 \times 10^{16}$ cm^{-3}) at short circuit and under illumination. Here, the left contact acts as cathode while the right contact acts as anode. A defined space-charge region is clearly visible, together with the presence of a nonuniform electric field. The latter is in fact low in most of the device and high only in the space-charge region, whose extension is much smaller than the cell thickness d. As a consequence, charge collection in the depletion region is driven by drift and is therefore more efficient than in the neutral, i.e. field-free, region where it is driven by diffusion. Note again that the situation depicted in Fig. 7.3 is profoundly different from the one presented at the beginning of the previous chapter (Fig. 6.1), where a thin intrinsic device was considered. In that case the electric field was approximately uniform, with the built-in voltage dropping more homogeneously over the active layer and the charge-collection efficiency varying more strongly with the applied voltage.

The analysis of the charge density present under illumination in a device like the one simulated for Fig. 7.3 starts with the consideration that, since the space-charge region is considered free of charge carriers, we can focus on the charge concentration

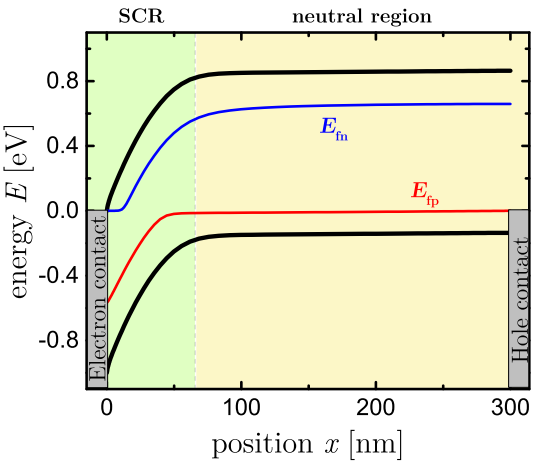

Figure 7.3: Band diagram of a 300 nm-thick solar cell with $N_A = 5 \times 10^{16}$ cm^{-3} and $\mu_n = \mu_p = 5 \times 10^{-4}$ cm^2/Vs under illumination and short-circuit conditions (applied voltage $V_{ext} = 0$ V). The device is only partially depleted and the space-charge region with a width much smaller than the cell thickness is clearly visible.

in the electrically neutral part of the device. Here, the electric field is zero and the majority charge-carrier density is equal to the doping density, i.e. $p = N_A$ for our chosen reference device. The minority carrier concentration, i.e. the electron concentration, is instead controlled by the continuity equation for electrons (Eq. (2.4)) and the electron current density equation (Eq. (2.6)) and can be derived from the transport equation for electrons (Eq. (2.8)). Since in the neutral region the electric field is zero, the transport equation simplifies to

$$\frac{\mathrm{d}^2 n}{\mathrm{d}x^2} - \frac{\Delta n}{L_n^2} + \frac{G}{D_n} = 0, \tag{7.7}$$

where $D_n = \mu_n \frac{k_B T}{q}$ is the diffusion coefficient, $L_n = \sqrt{D_n \tau_n}$ is the electron diffusion length, τ_n is the electron lifetime, x is the depth in the active layer, and the expression $R = \Delta n/\tau$ was used for the recombination rate [61]. For a material of absorption coefficient α, the intensity of an incident monochromatic light will be attenuated by the factor $e^{-\alpha x}$ and thus, neglecting reflection of photons at the surface, the generation rate G can be expressed as $G = \phi \alpha e^{-\alpha x}$, with ϕ being the incident monochromatic photon flux. Under these conditions, the general solution of Eq. (7.7) for the neutral

region is

$$n(x) = A\cosh(\frac{x-w}{L_\mathrm{n}}) - B\sinh(\frac{x-w}{L_\mathrm{n}}) - \gamma e^{-\alpha x}, \tag{7.8}$$

where

$$\gamma = \frac{\alpha\phi L_\mathrm{n}^2}{D_\mathrm{n}\left(\alpha^2 L_\mathrm{n}^2 - 1\right)} \tag{7.9}$$

and w is the width of the space-charge region. The coefficients A and B can be determined considering appropriate boundary conditions. The first boundary condition is defined at the edge of the depletion region, i.e. at $x = w$, and is given by the electron density at that specific point. In principle, the electron density at the edge of the space-charge region depends on the electron quasi Fermi levels, i.e. $n(w) = \frac{n_\mathrm{i}^2}{N_\mathrm{A}} e^{\frac{\left(E_{\mathrm{F_n}}(w) - E_{\mathrm{F_n}}(0)\right)}{k_\mathrm{B}T}}$, with n_i being the intrinsic charge density. However, for our analysis we choose $n(w) = 0$, which implies a quasi Fermi level for electrons constant and equal to zero in the whole SCR. The choice of this boundary condition, which is also the one considered by Moore in his work [155], derives from the assumption of having the same condition on the left and on the right side of the space-charge region. The impact of the boundary condition choice on the energy-band diagram of a simulated 300-nm thick device is shown in Fig. 7.4, where the difference between the quasi Fermi level $E_{\mathrm{F_n}}$ derived from analytical equations considering as boundary condition $n(w) = 0$ (Fig. 7.4(b)) and the quasi Fermi level $E_{\mathrm{F_n}}$ computed numerically via SCAPS simulations (Fig. 7.4(a)) is clearly visible. As we will show in the following, $n(w) = 0$ simplifies the analytical determination of the electron density in the neutral region and, despite being only an approximation, provides results that in most cases well agree with the results obtained using $n(w) = \frac{n_\mathrm{i}^2}{N_\mathrm{A}} e^{\frac{\left(E_{\mathrm{F_n}}(w) - E_{\mathrm{F_n}}(0)\right)}{k_\mathrm{B}T}}$ as boundary condition. The surface recombination at the rear surface, i.e. at $x = d$, provides instead the second boundary condition $S_\mathrm{na} n(d) = D_\mathrm{n} \frac{\mathrm{d}n}{\mathrm{d}x} \mid_{x=d}$, with S_na being the surface recombination velocity for electrons at the anode. The use of the two chosen boundary conditions allows the calculation of the coefficients A and B

$$A = \gamma e^{-\alpha w}, \tag{7.10}$$

$$B = \frac{\gamma\left[e^{-\alpha w}\left(\frac{S_\mathrm{na}L_\mathrm{n}}{D_\mathrm{n}}\cosh\left(\frac{d-w}{L_\mathrm{n}}\right) + \sinh\left(\frac{d-w}{L_\mathrm{n}}\right)\right) + e^{-\alpha d}\left(\alpha L_\mathrm{n} - \frac{S_\mathrm{na}L_\mathrm{n}}{D_\mathrm{n}}\right)\right]}{\frac{S_\mathrm{na}L_\mathrm{n}}{D_\mathrm{n}}\sinh\left(\frac{d-w}{L_\mathrm{n}}\right) + \cosh\left(\frac{d-w}{L_\mathrm{n}}\right)}. \tag{7.11}$$

If we consider the case of zero surface recombination at the anode, i.e. $S_\mathrm{na} = 0$, the

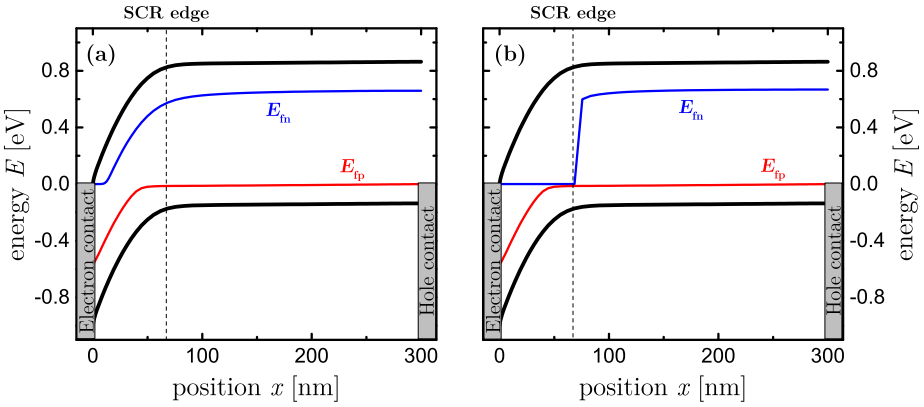

Figure 7.4: Energy-band diagrams of a simulated 300 nm-thick solar cell with $N_A = 5 \times 10^{16}$ cm^{-3} and where the quasi Fermi level E_{F_n} was computed (a) numerically through SCAPS or (b) obtained from analytical equations taking $n(w) = 0$ as boundary condition at the edge of the space-charge region. In the latter case E_{F_n} is constant and equal to zero in the entire space-charge region making the condition on the left and right sides of the SCR equal.

expression for B presented in Eq. (7.11) simplifies to

$$B = \frac{\gamma \left[e^{-\alpha w} \sinh\left(\frac{d-w}{L_n}\right) + e^{-\alpha d} \alpha L_n \right]}{\cosh\left(\frac{d-w}{L_n}\right)}. \tag{7.12}$$

Moreover, simpler analytical forms of Eq. (7.8) can be obtained when restrictions on the absorption coefficient α and the active-layer thickness d are taken into account. Here, we analyze the two extreme and diametrically opposite conditions, namely the case $\alpha d \gg 1$ and the case $\alpha d \ll 1$. The former case was already considered by Hinken et al. [156] within their study of the photoluminescence signal of silicon solar cells. The expression for the electron density inside the neutral region derived in Ref. [156] from the comparison of the luminescence emission under short-circuit and open-circuit conditions can be obtained also from the general solution mentioned above if the assumptions $\alpha d \gg 1$ and $S_{na} = 0$ are considered. In fact, in such a case, the coefficient A remains

unchanged while the coefficient B reduces to

$$B = \gamma e^{-\alpha w} \tanh\left(\frac{d-w}{L_\mathrm{n}}\right) \tag{7.13}$$

as the term containing $e^{-\alpha d}$ in Eq. (7.12) becomes negligible. The case $\alpha d \ll 1$ refers instead to a device illuminated by weakly absorbed light and allows one to approximate the factors $e^{-\alpha d}$ and $e^{-\alpha w}$ to 1. The general solution expressed in Eq. (7.8) is then still usable but the coefficients A and B acquire the new forms

$$A = \gamma \tag{7.14}$$

and

$$B = \frac{\gamma\left[\sinh\left(\frac{d-w}{L_\mathrm{n}}\right) + \alpha L_\mathrm{n}\right]}{\cosh\left(\frac{d-w}{L_\mathrm{n}}\right)}. \tag{7.15}$$

The combination of the assumption $\alpha d \ll 1$ with the assumption of a diffusion length L_n smaller than the absorber-layer thickness ($d \gg L_\mathrm{n}$) permits to obtain even simpler forms for the coefficients A, B, and γ and leads to an easy analytical expression for the electron density, as already pointed out by Moore [155]

$$n_\mathrm{Moore}(x) = \alpha\phi\tau_\mathrm{n}\left(1 - e^{-\frac{x-w}{L_\mathrm{n}}}\right). \tag{7.16}$$

Note that this approach, followed by Moore [155] to study the short-circuit capacitance of silicon solar cells, well highlights the relation between the electron density in the neutral region and the electrons lifetime.

It is clear that, even starting from the same general expression for the charge density at short circuit (Eq. (7.8)), the models based on the three approaches presented above, i.e. the general solution (Eqs. (7.9), (7.10), and (7.12)), Hinken's approach (Eqs. (7.9), (7.10), and (7.13)), and Moore's approach (Eq. (7.16)), provide results for $n(x)$ which, depending on the considered conditions in terms of α and L_n, might differ significantly. Table 7.2 summarizes the equations for the determination of the charge density according to the different models, whose validity conditions are also listed. The charge densities n_gen, n_Hinken, and n_Moore derived from the application of the general solution, Hinken's model, and Moore's model respectively, are compared in Fig. 7.5 as function of the depth in the absorber layer of our chosen reference device for different absorption

Table 7.2: Equations for the determination of the charge density $n(x)$ according to the different models and their corresponding validity ranges.

Model	Equations for the determination of $n(x)$	Approximation valid if
General solution	$n_{\mathrm{gen}}(x) = A\cosh(\frac{x-w}{L_\mathrm{n}}) - B\sinh(\frac{x-w}{L_\mathrm{n}}) - \gamma e^{-\alpha x}$ $A = \left[\frac{\alpha\phi L_\mathrm{n}^2}{D_\mathrm{n}(\alpha^2 L_\mathrm{n}^2-1)}\right]\cdot e^{-\alpha w}$ $B = \frac{\gamma\left[e^{-\alpha w}\sinh\left(\frac{d-w}{L_\mathrm{n}}\right)+e^{-\alpha d}\alpha L_\mathrm{n}\right]}{\cosh\left(\frac{d-w}{L_\mathrm{n}}\right)}$	$S_\mathrm{na} = 0$
Hinken's	$n_{\mathrm{Hinken}}(x) = A\cosh(\frac{x-w}{L_\mathrm{n}}) - B\sinh(\frac{x-w}{L_\mathrm{n}}) - \gamma e^{-\alpha x}$ $A = \left[\frac{\alpha\phi L_\mathrm{n}^2}{D_\mathrm{n}(\alpha^2 L_\mathrm{n}^2-1)}\right]\cdot e^{-\alpha w}$ $B = \gamma e^{-\alpha w}\tanh\left(\frac{d-w}{L_\mathrm{n}}\right)$	$S_\mathrm{na} = 0$ $\alpha d \gg 1$
Moore's	$n_{\mathrm{Moore}}(x) = \alpha\phi\tau_\mathrm{n}\left(1 - e^{-\frac{x-w}{L_\mathrm{n}}}\right)$	$S_\mathrm{na} = 0$ $\alpha d \ll 1$ $d \gg L_\mathrm{n}$

Table 7.3: Parameters used for the simulations with the software SCAPS.

	Quantity	Default set
Band mobility	μ_n [cm^2/Vs]	1×10^{-4} or 1×10^{-2}
	μ_p [cm^2/Vs]	1×10^{-4} or 1×10^{-2}
Effective density of states	$N_\mathrm{C} = N_\mathrm{V}$ [cm^{-3}]	10^{19}
Bandgap	E_g [eV]	1.0
Thickness	d [nm]	300
Doping concentration	N_A [cm^{-3}]	5×10^{16}
Relative permittivity	ε_r	3.0
Direct recombination coefficient	k_dir [cm^3/s]	1×10^{-12}
Absorption coefficient	α [cm^{-1}]	1×10^{3} or 1×10^{5}
Photon flux	ϕ [cm^{-2}s^{-1}]	2.5×10^{17}

coefficient and diffusion length values. The same figure also displays the charge density $n_{\mathrm{SCAPS}}(x)$ obtained from drift-diffusion simulations at short circuit of a 300 nm-thick solar cell with a relatively high doping density ($N_{\mathrm{A}} = 5 \times 10^{16}$ cm^{-3}) performed with the software SCAPS. For such simulations a monochromatic light ($\lambda = 500$ nm) is used as light source, together with the parameters defining the absorber layer summarized in Table 7.3. Since only direct recombination described by the recombination coef-

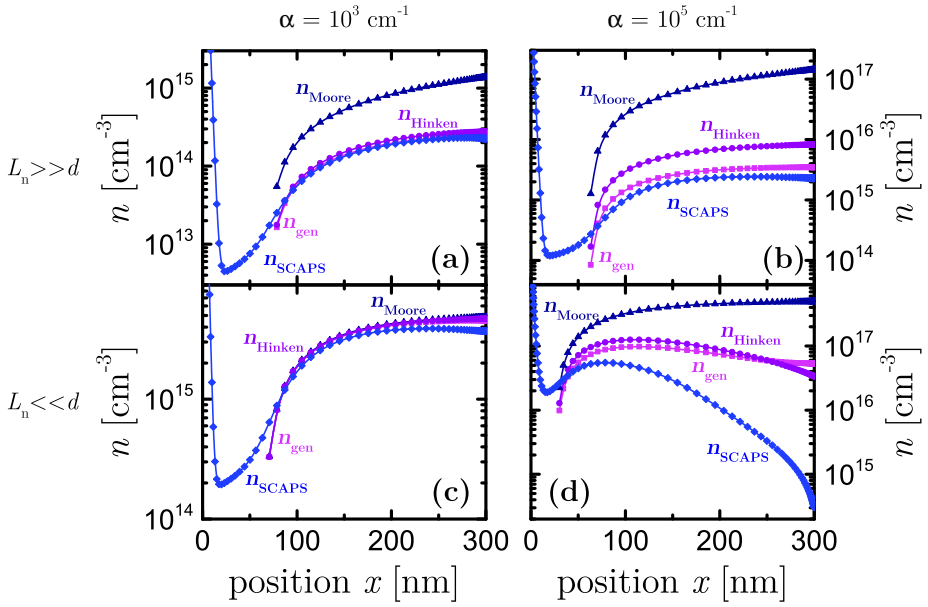

Figure 7.5: Electron densities n_{gen}, n_{Hinken}, and n_{Moore} derived from the three models as a function of the position inside the absorber layer of a 300 nm-thick device with $N_{\mathrm{A}} = 5 \times 10^{16}$ cm^{-3} illuminated by monochromatic light ($\lambda = 500$ nm) at short circuit. (a) and (b) present the cases of electron diffusion length larger than the absorber-layer thickness; (c) and (d) present the cases of electron diffusion length much smaller than the absorber-layer thickness. The results in (a) and (c) were obtained using a relatively lower absorption coefficient than the results in (b) and (d). Even though in most cases n_{gen} and n_{Hinken} are in good agreement, only for low diffusion length and absorption coefficient all three models provide very similar results which resemble quite well also the charge density n_{SCAPS} obtained directly from SCAPS simulations.

ficient k_{dir} is considered, the lifetime τ_{n} necessary for the calculation of the electron

diffusion length can be determined via $\tau_n = 1/(k_{dir} N_A)$. Having fixed the lifetime, L_n is now only a function of the diffusion coefficient D_n which, according to Einstein's relation, depends on the charge-carrier mobility that can therefore be varied to obtain different L_n values. Figures 7.5(a) and 7.5(b) show the cases of high charge-carrier mobility ($\mu_n = \mu_p = 1 \times 10^{-2}$ cm^2/Vs), which results in a diffusion length larger than the absorber-layer thickness ($L_n > d$). Figures 7.5(c) and 7.5(d) present the cases where $d \gg L_n$ is achieved through the low mobility employed for the simulations ($\mu_n = \mu_p = 1 \times 10^{-4}$ cm^2/Vs). Finally, the results in Figs. 7.5(a) and 7.5(c) correspond to the cases with a relatively lower absorption coefficient ($\alpha = 10^3$ cm^{-1}) than the cases presented in Figs. 7.5(b) and 7.5(d) ($\alpha = 10^5$ cm^{-1}). In general, it can be observed that the charge density n_{gen} and n_{Hinken} are in good agreement with each other and with the charge density n_{SCAPS} resulting from SCAPS simulations. On the other hand, the charge density n_{Moore} obtained applying Eq. (7.16) differs by more than one order of magnitude in all the cases considered except the one depicted in Fig. 7.5(c). In fact, just when both assumptions $\alpha d \ll 1$ and $d \gg L_n$ are valid, Eq. (7.16), i.e. Moore's approximation, approximates well the general solution expressed by Eq. (7.8) and is thus able to predict quite accurately the electron distribution inside the neutral zone of the absorber layer of a partially depleted device under illumination. The case displayed in Fig. 7.5(c) is also the only case where all three models provide almost identical results which are in very good agreement also with the charge density obtained directly from SCAPS simulations. Worthy of note it is also the case with a high absorption coefficient and a small diffusion length presented in Fig. 7.5(d). Here, n_{SCAPS} shows a trend completely different even from the one of n_{gen} and n_{Hinken}; the charge density in fact decreases towards the back of the device, i.e. at increasing depth inside the absorber layer. To understand the reason of this discrepancy, the energy-band diagrams of the device under the conditions corresponding to Fig. 7.5(c) and 7.5(d) are analyzed. Figure 7.6(a) displays the band diagram for the case with low L_n and α (as in Fig. 7.5(c)), whereas Fig. 7.6(b) shows the band diagram for the case with identical diffusion length but higher absorption coefficient (as in Fig. 7.5(d)). In the former, the space-charge region is clearly visible, as well as the neutral zone where the electric field is zero. This situation is at the basis of the analysis presented above, which aims at the determination of the charge density in the field-free region by considering only the diffusion of charge carriers. However, it is evident that for the case displayed in

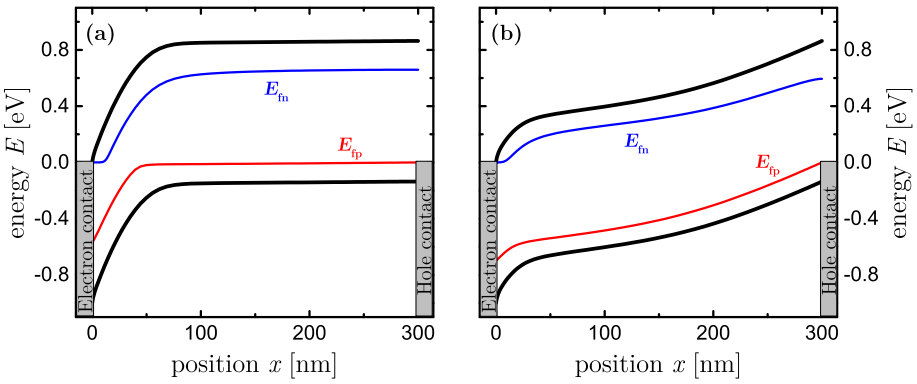

Figure 7.6: Energy-band diagrams under monochromatic illumination and short-circuit conditions of a 300 nm-thick solar cell with $N_A = 5 \times 10^{16}$ cm^{-3}, $\mu_n = \mu_p = 5 \times 10^{-4}$ cm^2/Vs, and (a) $\alpha = 10^3$ cm^{-1} or (b) $\alpha = 10^5$ cm^{-1}. When the absorption coefficient is low the space-charge region and the neutral zone with no electric field are clearly visible, whereas at higher α a region completely field free is absent.

Fig. 7.6(b) a completely field-free region is absent. A significant electric field is, in fact, present even in the zone outside the space-charge region, which implies that the charge collection outside this region is driven not only by diffusion but also by drift. Thus, the transport equation for electrons cannot be simplified to Eq. (7.7), which is the starting point of the analysis presented above. As a consequence, the trend of n_{gen}, n_{Hinken}, and n_{Moore} differs substantially from the one shown by the charge density n_{SCAPS} directly obtained from SCAPS simulations.

In order to have a broader overview of the validity range of the three models used to determine the charge density in the neutral region of a doped ($N_A = 5 \times 10^{16}$ cm^{-3}) 300 nm-thick device, n_{gen}, n_{Hinken}, and n_{Moore} were calculated for several absorption coefficient and diffusion length values. As reference for the comparison, the charge density at the back contact, i.e. at $x = d$, is chosen. Figure 7.7(a) depicts the $n_{gen}(d)$ values computed from the general solution for absorption coefficients ranging from 10^1 to 10^6 cm^{-1} and diffusion lengths ranging from 22.7 to 7.17×10^3 nm (or mobility from 10^{-5} to 10^0 cm^2/Vs). The same α and L_n values were considered to determine, by using Hinken's or Moore's approach, the charge densities n_{Hinken} and n_{Moore} displayed in Figs. 7.7(b) and 7.7(c), respectively. Figure 7.7 clearly shows that for $\alpha < 10^3$ cm^{-1}

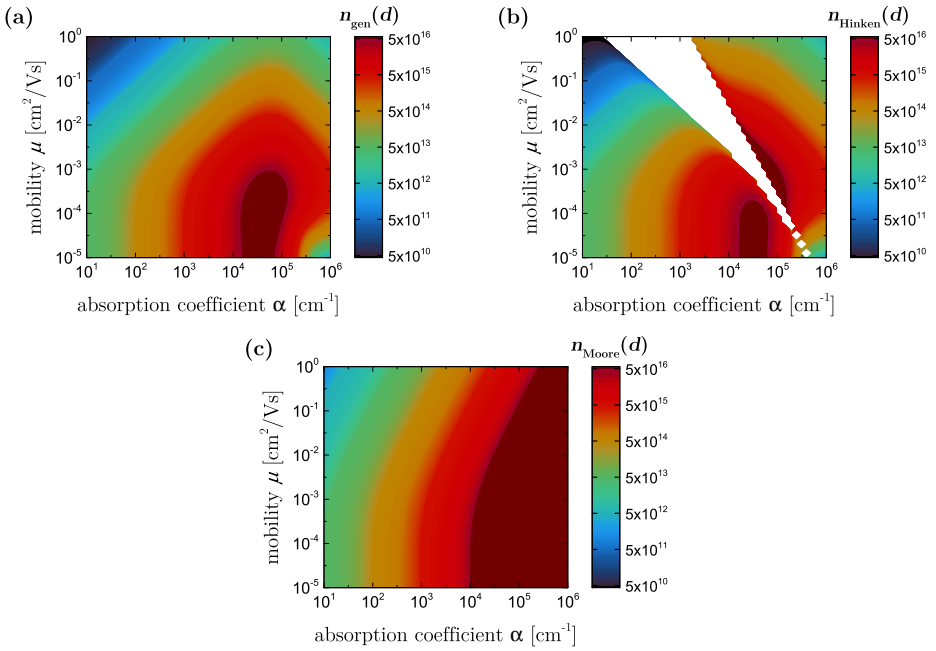

Figure 7.7: Charge densities (a) $n_{\mathrm{gen}}(d)$, (b) $n_{\mathrm{Hinken}}(d)$, and (c) $n_{\mathrm{Moore}}(d)$ determined with the three models for absorption coefficients ranging from 10^1 to 10^6 cm^{-1} and charge carrier mobilities ranging from 10^{-5} to 10^0 cm^2/Vs (or diffusion lengths ranging from 22.7 to 7.17 $\times$ 10^3 nm). At low α and μ (or L_{n}) the three models provide very similar charge densities at $x = d$.

and $\mu < 10^{-3}$ cm^2/Vs (or $L_{\mathrm{n}} < 227$ nm) the charge densities at $x = d$ obtained from the three models are very alike. However, as either the diffusion length or the absorption coefficient increases, $n_{\mathrm{Moore}}(d)$ starts differing more and more from both $n_{\mathrm{gen}}(d)$ and $n_{\mathrm{Hinken}}(d)$. On the other hand, $n_{\mathrm{gen}}(d)$ and $n_{\mathrm{Hinken}}(d)$ are similar in a broader range of α and L_{n} values, including the cases with both high absorption coefficient and large diffusion length. Even if higher α are not expected to significantly affect the calculation of $n_{\mathrm{Hinken}}(d)$ due to the model assumption $\alpha d \gg 1$, a blank region without data is visible in Fig. 7.7(b). The use of combinations of α and L_{n} defining this region for the calculation of the charge density $n_{\mathrm{Hinken}}(d)$ provides in fact negative values. This peculiar behavior is due to the formulation of the expression used to determine

the charge density according to Hinken's model. By substituting the coefficient B of Eq. (7.13) into Eq. (7.8), it is possible to show that $n_{\mathrm{Hinken}}(d)$ acquires negative values when the expression

$$\frac{1}{\cosh\left(\frac{d-w}{L_{\mathrm{n}}}\right)} < e^{-\alpha d} \tag{7.17}$$

is valid, which happens inside the blank region of Fig. 7.7(b).

7.4 Lifetime vs Mobility

The possibility to determine the charge-carrier lifetime from capacitance-voltage data under illumination through the approach presented above mostly depends on the validity of the assumptions $d \gg L_{\mathrm{n}}$ and $dw \ll L_{\mathrm{n}}$ used to derive Eq. (7.5), in addition to the assumption of weakly absorbed light on which Eq. (7.16) relies on. These assumptions can easily break down when the absorber-layer thickness or the doping density are reduced. A low doping density implies in fact a bigger space-charge region whose width might then be in the same order of magnitude of the absorber-layer thickness. The same effect is obtained also with a thinner device and an unaltered relatively high doping density. It is thus clear that a range of validity for the aforementioned model relating the lifetime and C-V data under illumination exists and that it is strongly dependent upon the absorber-layer thickness d and the doping density N_{A}. In the previous chapter it has been shown that under certain circumstances the capacitance-voltage curves obtained under illumination are sensitive to the charge-carrier mobility, whose value can therefore be extracted from C-V data at reverse bias. The method discussed in chapter 6 for the determination of the mobility and the method presented here for the calculation of the lifetime rely on diametrically opposite assumptions. The former requires in fact fully depleted devices (i.e. thin absorber layers and low doping densities) and a constant electric field inside the absorber layer, whereas the latter demands the presence of a space-charge region which can be provided by thick and highly doped absorber layers. Thus, it is reasonable to expect the two methods to be valid in two different ranges in terms of doping density and absorber-layer thickness.

In order to confirm our hypothesis of diametrically different validity ranges of the methods for lifetime and mobility determination, drift-diffusion simulations with the software SCAPS were performed under illumination for several doping densities and

absorber-layer thicknesses. For a better adherence to the real measuring conditions a generation profile was created using the simulation tool ASA in combination with its subroutine *genpro1*. For the creation of the generation profile the device stack glass/ITO/PEDOT:PSS/P3HT:$PC_{61}BM$/Ca/Al was used together with the thicknesses 1 mm, 120 nm, 25 nm, 30 nm, and 150 nm set respectively for glass, ITO, PEDOT:PSS, Ca, and Al layers. The results of these simulations are summarized in Figs. 7.8 and 7.9. The lifetime τ_{CV} obtained from capacitance-voltage data by using Eq. (7.6) and considering the maximum generation rate $G_{max} = \alpha\phi \approx J_{sc}/qd$ is first compared to the lifetime $\tau_{sim} = 1/(k_{dir}N_A)$ set for the simulations. Figure 7.8 presents this comparison showing how the ratio τ_{CV}/τ_{sim} varies as a function of the absorber-layer thickness d and doping densities N_A and confirms that the assumptions $d \gg L_n$ and $dw \ll L_n$ at the basis of the approach presented above make it inapplicable for the cases of low d and N_A. Figure 7.9 displays instead for which absorber-layer thicknesses d and doping

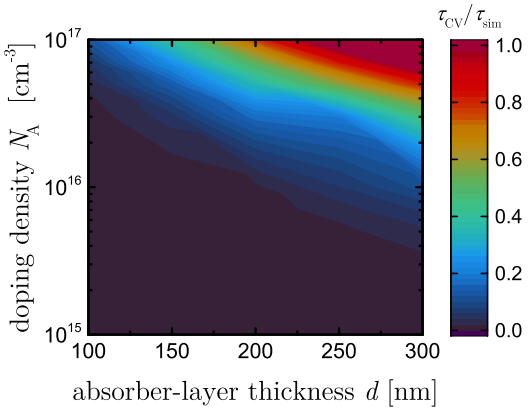

Figure 7.8: Ratio between the lifetime τ_{CV} calculated with Eq. (7.6) and the lifetime τ_{sim} set for the simulations performed under illumination with different doping densities and absorber-layer thicknesses. At low N_A and d the assumptions for the derivation of Eq. (7.6) are not fulfilled and, thus, the lifetime value extracted from C-V data differs strongly from the one set for the simulations.

densities N_A the charge-carrier lifetime and the charge-carrier mobility can be derived from simulated C-V data under illumination. The extracted lifetime values τ_{CV} are obtained with Eq. (7.6) considering the maximum generation rate $G_{max} = \alpha\phi \approx J_{sc}/qd$

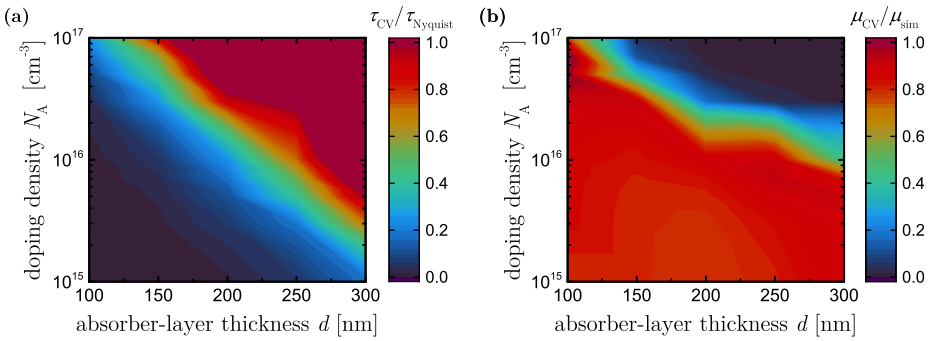

Figure 7.9: Simulations under illumination of devices with $\mu_n = \mu_p = 5 \times 10^{-4}$ cm^2/Vs and different thicknesses and doping densities. (a) Ratio between the lifetime τ_{CV} calculated with Eq. (7.6) and the lifetime $\tau_{Nyquist}$ determined from fitting the Nyquist plots; (b) ratio between the mobility μ_{CV} obtained from the fitting procedure described in chapter 6 and the value μ_{sim} set for the simulations. At low doping densities and thicknesses τ_{CV} is much smaller than $\tau_{Nyquist}$, but they become closer when N_A and d are increased. The behavior of the ratio μ_{CV}/μ_{sim} is completely opposite since it approaches 1 for thin and lowly doped devices.

and are normalized to the reference lifetime value $\tau_{Nyquist}$ obtained by fitting the Nyquist plots of the same simulations with the procedure and the equivalent circuit presented in section 4.4.2. The charge-carrier mobility μ_{CV} is instead determined from the fitting procedure described in the previous chapter and is normalized to the value μ_{sim} set for the numerical simulations. From Fig. 7.9(a) it becomes clear that for thin and lowly doped devices the lifetime τ_{CV} is much smaller than the lifetime derived from the Nyquist plots. However, when N_A and d are increased, the two lifetime values approach each other and finally τ_{CV} becomes larger than $\tau_{Nyquist}$. In contrast, Fig. 7.9(b) shows that the mobility μ_{CV} obtained from C-V data approaches the value μ_{sim} set for the simulations when the device is thin or lowly doped and substantially decreases only when the doping density is increased.

The verified possibility to derive the charge-carrier lifetime and the charge-carrier mobility from C-V data under different circumstances suggests that capacitance-voltage curves under illumination are mostly sensitive to either charge-carrier mobility or charge-carrier lifetime depending on the doping level and the absorber-layer thickness of the device under investigation. For thick and highly doped devices, the lifetime plays a

major role in the modulation of the capacitance obtained under illumination, while the influence of mobility becomes dominant for low doping densities and small absorber-layer thicknesses. This confirms once more that the applicability of a certain analysis method on capacitance-voltage data obtained under illumination strongly depends on the sample properties and the measurement conditions.

7.5 Experimental Results

As final test, capacitance-voltage measurements at a fixed frequency of 5 kHz and at different light intensities were performed on 380 nm-thick P3HT:$PC_{71}BM$ solar cells with $N_A = 2.2 \times 10^{15}$ cm^{-3} and $N_A = 6.8 \times 10^{15}$ cm^{-3}. The resulting extracted lifetime values were then compared to the values obtained from light-dependent simulations of a 400 nm-thick device with two different doping densities ($N_A = 2 \times 10^{15}$ cm^{-3} and $N_A = 7 \times 10^{15}$ cm^{-3}). The parameters used for these simulations are displayed in Table 7.4.

Table 7.4: Parameters used for the simulations with the software SCAPS.

	Quantity	Default set
Band mobility	μ_n [cm^2/Vs]	5×10^{-4}
	μ_p [cm^2/Vs]	5×10^{-4}
Effective density of states	$N_C = N_V$ [cm^{-3}]	10^{19}
Bandgap	E_g [eV]	0.9
Thickness	d [nm]	400
Doping concentration	N_A [cm^{-3}]	2×10^{15} or 7×10^{15}
Relative permittivity	ε_r	3.0
Direct recombination coefficient	k_{dir} [cm^3/s]	1×10^{-12}

Figure 7.10 presents, as a function of the open-circuit voltage, the lifetime values $\tau_{Nyquist}$ obtained from fitting the Nyquist plots and the lifetime values τ_{CV} extracted from C-V data using the method described above. The results for the simulated device with $N_A = 2 \times 10^{15}$ cm^{-3} and $N_A = 7 \times 10^{15}$ cm^{-3} are shown in Figs. 7.10(a) and

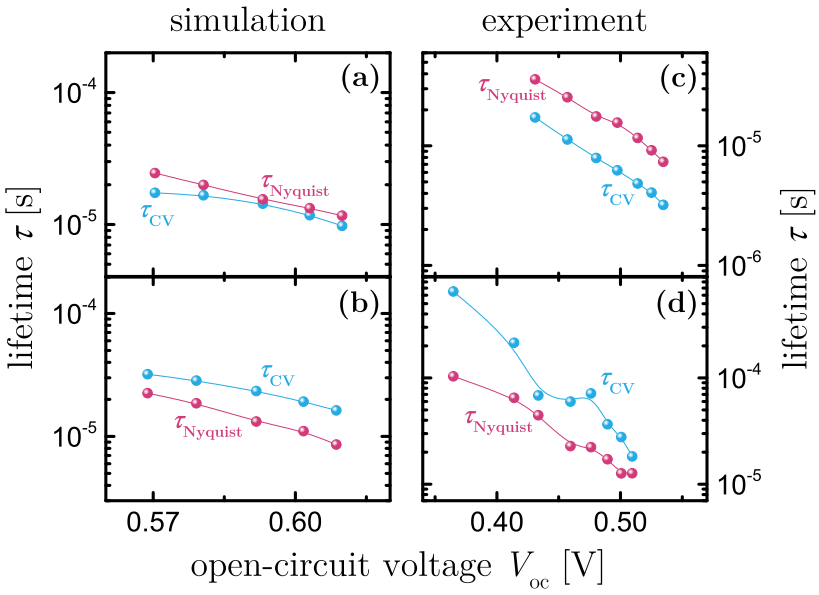

Figure 7.10: Lifetime values, as a function of the open-circuit voltage, extracted from Nyquist plots and from *C-V* data for a simulated 400 nm-thick device with (a) $N_A = 2 \times 10^{15}$ cm^{-3} and (b) $N_A = 7 \times 10^{15}$ cm^{-3} and a 380 nm thick P3HT:PC$_{71}$BM device with (c) $N_A = 2.2 \times 10^{15}$ cm^{-3} and (d) $N_A = 6.8 \times 10^{15}$ cm^{-3}. The filled circles represent the extracted τ values, while the lines are just a guide to the eye. Simulations and experimental measurements provide results with qualitatively the same behavior, i.e. $\tau_{Nyquist} > \tau_{CV}$ for low doping densities ((a) and (c)) and $\tau_{Nyquist} < \tau_{CV}$ for high doping densities ((b) and (d)).

7.10(b), while Figs. 7.10(c) and 7.10(d) display the lifetime values of a P3HT:PC$_{71}$BM solar cell with a doping density equals respectively to $N_A = 2.2 \times 10^{15}$ cm^{-3} and $N_A = 6.8 \times 10^{15}$ cm^{-3}, as determined by Mott-Schottky analysis. As expected, in all cases the lifetime decreases as the open-circuit voltage (or the light intensity) increases. The results obtained from simulations and experimental measurements show qualitatively the same behavior with $\tau_{Nyquist}$ being bigger than τ_{CV} when the doping density is low (Figs. 7.10(a) and 7.10(c)) and smaller than τ_{CV} when the doping density is higher (Figs. 7.10(b) and 7.10(d)). Note that the same behavior as function of the doping density was already highlighted within the discussion of Fig. 7.9(a), which indeed points

out that for thin and lowly doped devices $\tau_{\text{Nyquist}} > \tau_{\text{CV}}$ whereas for high doping densities and absorber-layer thicknesses $\tau_{\text{Nyquist}} < \tau_{\text{CV}}$. The charge-carrier lifetime values τ_{CV} and τ_{Nyquist} are respectively within the time interval $1.7 \times 10^{-5} - 3.2 \times 10^{-6}$ s and $3.6 \times 10^{-5} - 7.4 \times 10^{-6}$ s for the P3HT:PC_{71}BM device with the lower doping density. For the higher doped P3HT:PC_{71}BM device, τ_{CV} is within $6.5 \times 10^{-4} - 1.8 \times 10^{-5}$ s and τ_{Nyquist} within $1.0 \times 10^{-4} - 1.3 \times 10^{-5}$ s. These results are in agreement with literature values for charge-carrier lifetime measured for the same polymer:fullerene system with open-circuit corrected charge-carrier extraction [157], transient photovoltage [158], and impedance spectroscopy [33].

7.6 Conclusions

This chapter presented an analysis of the capacitance of a partly depleted device under illumination and short-circuit conditions. Different analytical models for the determination of the charge-carrier density in the neutral region of such device were presented and their validity range in terms of absorption coefficient and diffusion length discussed. The approach on which one of the aforementioned models relies allowed to derive expressions relating the charge density to the photocapacitance at short circuit and the latter to the charge-carrier lifetime, whose value could thus be derived from C-V data. In addition, the crucial influence of sample properties and measurement conditions on the applicability of methods to analyze capacitance-voltage curves was emphasized once more showing that under illumination C-V data can be strongly affected either by charge-carrier mobility or charge-carrier lifetime depending on the doping level and the absorber-layer thickness. The results of this chapter complete therefore the understanding of capacitance-voltage data obtained in all possible measurement scenarios.

Chapter 8

Extracting Recombination Parameters from Impedance Measurements

This chapter focuses on another type of impedance measurements, namely the capacitance-frequency measurements, and presents a method to extract the recombination parameters from such measurements performed under illumination on organic solar cells. The description of the approach used to determine the charge density from impedance data is followed by numerical simulations and experimental data aimed to illustrate how the dependence of the recombination current on the photogenerated charge density may be used to identify the dominant recombination mechanism and to determine either the charge-carrier lifetime or the bimolecular recombination coefficient. This chapter is based on the results presented in the published paper *Extracting Recombination Parameters from Impedance Measurements on Organic Solar Cells* by Zonno et al. [159] whose copyright lies by the American Physical Society.

8.1 Introduction

As already pointed out, nongeminate recombination has detrimental effects on the open-circuit voltage, the fill factor, and the short-circuit current of organic solar cells. Understanding and reducing this type of recombination is therefore essential for the further enhancement of this technology. Transient measurements commonly used to determine recombination parameters, in particular the transient photovoltage technique, have re-

cently been shown to be affected by capacitive effects [160], which are not directly related to the actual charge-carrier lifetime. Also frequency domain methods, such as capacitance-based techniques, feature some intrinsic problems due to the lack of an unambiguous method to calculate the chemical capacitance [94,161] and the difficulties in taking the non-linear electrode capacitance into account. In order to arrive at comparable values for the recombination coefficient, the determination of the charge-carrier density and the kinetic parameters such as the charge-carrier lifetime is needed. The recombination rate R is, in fact, a function of the density of free electrons and holes which themselves depend on mobility and lifetime. In the following, simulations and experiments are used together to present a method for the determination of the charge-carrier density and the recombination parameters from impedance measurements on organic solar cells under illumination.

8.2 Theoretical Background

The recombination current density J_{rec}, which quantifies the current losses caused by the recombination of photogenerated charge carriers, is related to the total current density J and the current density of photogenerated charge carriers J_{ph} and, as schematically shown in Fig. 8.1, can be experimentally determined from the measured light and dark J-V curves

$$J_{\mathrm{rec}} = J_{\mathrm{ph,sat}} + J_{\mathrm{ph}}, \tag{8.1}$$

where $J_{\mathrm{ph}} = J_{\mathrm{light}} - J_{\mathrm{dark}} < 0$ is the photocurrent and $J_{\mathrm{ph,sat}} = q\bar{G}d > 0$ is the photocurrent at a sufficiently high reverse bias where the current has saturated.

The bulk recombination current density, obtained integrating the bulk recombination rate over the active-layer thickness as expressed by Eq. (3.12), is due to different recombination mechanisms. If we, for simplicity, assume that surface recombination can be neglected and that these bulk recombination mechanisms can be separated into a bimolecular and a monomolecular term, we may describe the recombination current by the integral over thickness of these two contributions

$$J_{\mathrm{rec}} \approx q \int_0^d \left(k_{\mathrm{dir}} n\left(x\right) p\left(x\right) + \frac{\min\left(n\left(x\right), p\left(x\right)\right)}{\tau} \right) \mathrm{d}x. \tag{8.2}$$

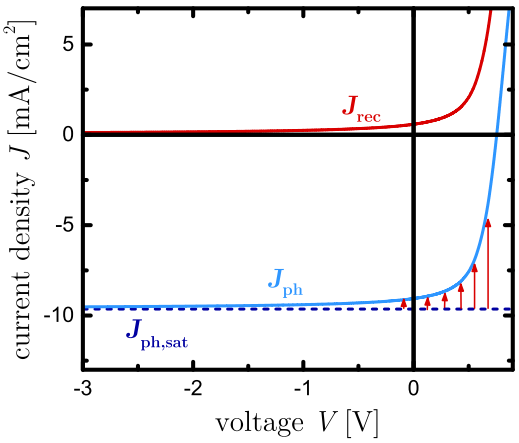

Figure 8.1: Recombination current density J_{rec} and photocurrent density J_{ph} as function of voltage for a simulated intrinsic solar cell with a 100 nm-thick active layer. J_{rec} can be obtained from the saturated photocurrent $J_{ph,sat}$ and the photocurrent J_{ph} which is defined by the difference between the light and dark J-V curve.

Here q represents the elementary charge, k_{dir} the bimolecular or direct recombination coefficient, τ the monomolecular charge-carrier lifetime, and n and p the electron and hole concentration, respectively. Equation (8.2) clearly shows that J_{rec} is a function of the electron and hole concentrations, as well as of the lifetime, and thus its calculation primarily requires the determination of the charge-carrier density in the bulk of the active-layer material. However, this calculation is complicated by the presence of charge on the electrodes which needs to be accounted for via an appropriate correction. In the literature on methods to determine the charge density in the active layer of organic solar cells, the charge density on the electrodes has typically been assumed to be a linear function of voltage and the ratio between charge and voltage has been supposed to be given by the geometrical capacitance $C_g = \varepsilon A/d$, with $\varepsilon = \varepsilon_0 \cdot \varepsilon_r$ being the permittivity and A and d the device area and thickness, respectively. This approach, however, does not take into account that the free charge carriers in the bulk of the material also react to the electric field and thereby they reduce it in the middle of the device and increase it towards the electrodes. This effect, which leads to band bending, changes with the density of electrons and holes and hence with the voltage.

The existence of band bending in intrinsic organic absorber layers has been recognized early on [162] but the consequence of it, namely that the capacitance of the electrode charge is non-linear with voltage, has rarely been spelled out explicitly. Most corrections [148, 163, 164] do not take the non-linear electrode charge into account but are based on a 'geometrical', constant capacitance. Thus, they lead to an error in the determined value of the charge-carrier density in the active layer and, consequently, also of the recombination current density. Once the charge-carrier density has been correctly determined, the second challenge in the calculation of the recombination current density is that the recombination rate averaged over volume is compared to the charge density averaged over volume. However, as already highlighted in literature [165, 166], the relation between recombination rates and charge-carrier densities is a local one (see Eq. (8.2)) and hence there is an error associated with this method that is due to the following inequality

$$\frac{\int_0^d \left(k_{\mathrm{dir}} n(x) p(x) + n\left(x\right)/\tau\right) \mathrm{d}x}{k_{\mathrm{avg}} \bar{n}^2 + \bar{n}/\tau_{\mathrm{avg}}} \neq 1. \tag{8.3}$$

The numerator in Eq. (8.3) correctly accounts for the charge-carrier distributions inside the active layer of a bulk heterojunction device, while the denominator considers the spatial average charge-carrier concentration $\bar{n}$ together with the average recombination coefficient k_{avg} and the average lifetime τ_{avg} calculated from $\bar{n}$. The inequality of Eq. (8.3) stems from two assumptions that are not valid under most measurement conditions; namely that $n(x) = p(x)$ and that $\int n(x)p(x)\mathrm{d}x = \bar{n} \cdot \bar{p}$, where x is the distance from the anode. In a bulk heterojunction solar cell, spatial gradients of both holes and electrons exist and their presence makes the left-hand ratio in Eq. (8.3) smaller than 1. Thus, the steeper these spatial gradients, the lower the ratio in Eq. (8.3) is, i.e. the bigger is the error caused by considering the spatially averaged charge-carrier concentration $\bar{n}$, which is the only value experimentally accessible. Different factors, such as the amount of illumination, the charge-carrier mobility, and the applied voltage, affect the steepness of the charge-carrier spatial gradients. Specifically, at high light intensities, low charge-carrier mobilities, and voltages close to V_{oc} the carrier-concentration gradients diminish [166]. In such a situation, the left-hand ratio of Eq. (8.3) is approximately

1 and Eq. (8.2) can be simplified to

$$J_{\mathrm{rec}} = q \int_0^d \left(k_{\mathrm{avg}} \bar{n}^2 + \frac{\bar{n}}{\tau_{\mathrm{avg}}} \right) \mathrm{d}x. \tag{8.4}$$

Thus, one of the key questions in the literature on characterization methods to determine recombination parameters in organic (and other thin-film) solar cells is the understanding of the circumstances under which a zero-dimensional treatment, as described by Eq. (8.4), is appropriate and useful, and of how the average values k_{avg} and τ_{avg} compare to the local values k_{dir} and τ used in Eqs. (8.2) and (8.3).

8.3 Determination of the Average Charge-Carrier Density

A prerequisite to make use of Eq. (8.4) is finding a way to determine $\bar{n}$ as a function of voltage, so that it could be compared to the recombination current in order to determine k_{avg} and τ_{avg}. One of the main techniques used to determine the charge-carrier density in organic solar cells under different operating conditions is impedance spectroscopy. In fact, the capacitance of a solar cell, derived from the imaginary part of the admittance, is sensitive to the density of charge carriers and, depending on the range of bias voltages and illumination conditions, may yield the doping density of the active layer or the optically or electrically injected charge-carrier concentration. The determination of the charge-carrier density from impedance data relies on the integration over voltage of the chemical capacitance per area C_μ, which is due to the charge carriers present in the active layer [80, 112]

$$\bar{n}\left(V_{\mathrm{int}}\right) = n_{\mathrm{ref}} + \frac{1}{qd} \int_{V_{\mathrm{ref}}}^{V_{\mathrm{int}}} C_\mu\left(V_{\mathrm{int}}\right) \mathrm{d}V_{\mathrm{int}}. \tag{8.5}$$

Here the internal voltage $V_{\mathrm{int}} = V - JR_{\mathrm{s}}$ is obtained correcting the applied voltage V by the series resistance R_{s}, V_{ref} is the reverse bias at which the photocurrent saturates, and d is the active-layer thickness. The charge density n_{ref} refers to the charge density

at the reverse bias V_{ref}, i.e. to the charge density calculated from the $C_\mu\left(V_{\mathrm{ref}}\right)$ value

$$n_{\mathrm{ref}} = \frac{1}{qd} C_\mu\left(V_{\mathrm{ref}}\right) \cdot \left(V_0 - V_{\mathrm{ref}}\right), \tag{8.6}$$

with V_0 being the voltage at which the photocurrent equals zero. The direct application of Eq. (8.5) is, however, hindered by the fact that the determination of the chemical capacitance is not straightforward and presents some intrinsic difficulties. In the majority of the impedance studies on organic solar cells, the chemical capacitance has been obtained using equivalent circuit modeling [151,167,168]. However, as already highlighted in section 4.4.2, the choice of the appropriate circuit can be challenging due to the non-uniqueness of the equivalent circuit and to the possibility to fit the measured impedance spectra with a potential infinitely complex equivalent circuit. One possibility to determine the chemical capacitance via a model-free method is to calculate C_μ subtracting a constant – i.e. voltage independent – geometrical capacitance C_{g} from the capacitance measured at low frequencies $C_{\mathrm{f,low}}$

$$C_\mu\left(V_{\mathrm{int}}\right) \approx C_{\mathrm{f,low}}\left(V_{\mathrm{int}}\right) - C_{\mathrm{g}}. \tag{8.7}$$

A second option, as suggested by Brus et al. [161], is to determine the chemical capacitance from the difference between the low-frequency and high-frequency capacitance under illumination

$$C_\mu\left(V_{\mathrm{int}}\right) \approx C_{\mathrm{f,low}}\left(V_{\mathrm{int}}\right) - C_{\mathrm{f,high}}\left(V_{\mathrm{int}}\right). \tag{8.8}$$

Nevertheless, a more correct approach would be to take the non-linear charge on the electrodes into account and subtract it from the capacitance measured at low frequencies

$$C_\mu\left(V_{\mathrm{int}}\right) \approx C_{\mathrm{f,low}}\left(V_{\mathrm{int}}\right) - C_\sigma,$$

where the capacitance per area of the electrodes C_σ is given by the derivative

$$C_\sigma = q\frac{\mathrm{d}\sigma}{\mathrm{d}V}. \tag{8.9}$$

The areal charge density on the electrodes is defined as $\sigma = \varepsilon F_{\mathrm{c/a}}$, where ε is the permittivity and $F_{\mathrm{c/a}}$ the electric field at the cathode or anode.

In order to present and compare the different capacitance definitions, frequency-

dependent drift-diffusion simulations of an intrinsic 100 nm-thick solar cell under illumination were performed with the software SCAPS using the parameters summarized in Table 8.1. The extraction of the capacitance from the resulting impedance data as

Table 8.1: Parameters used for the simulations with the software SCAPS if not stated otherwise.

	Quantity	Default set
Band mobility	μ_{n} [$\mathrm{cm}^2/\mathrm{Vs}$]	5×10^{-4}
	μ_{p} [$\mathrm{cm}^2/\mathrm{Vs}$]	5×10^{-4}
Effective density of states	$N_{\mathrm{C}} = N_{\mathrm{V}}$ [cm^{-3}]	10^{19}
Bandgap	E_{g} [eV]	1.0
Thickness	d [nm]	100
Doping concentration	N_{A} [cm^{-3}]	0
Relative permittivity	ε_{r}	3.5
Direct recombination coefficient	k_{dir} [cm^3/s]	5×10^{-12}
Generation rate	G [$\mathrm{cm}^{-3}\mathrm{s}^{-1}$]	6×10^{21}

function of frequency is based on the modeling of the device with a simple equivalent circuit consisting of a resistor and a capacitor connected in parallel (i.e. the $\mathrm{C_pR_p}$ model described in section 6.3), at which a series resistance R_{s}, accounting for the wires and connection to the device electrodes, is added. By taking R_{s} into account, it is possible to obtain the series-resistance-corrected capacitance via

$$C = -\frac{1}{\omega}\left(\frac{Z''}{\left(Z' - R_{\mathrm{s}}\right)^2 + \left(Z''\right)^2}\right), \tag{8.10}$$

where $\omega = 2\pi f$ is the angular frequency, Z' the real part of the total impedance, and Z'' the imaginary part of the total impedance. The influence of the series resistance on the capacitance-frequency curves and the impact of the R_{s} correction are displayed in Fig. 8.2 which shows the *C-f* curves obtained measuring under 1-sun illumination a PCE10:$\mathrm{PC_{71}BM}$ device for voltages ranging from -3 to 0.8 V. Even though the effect of the series resistance is visible over the entire frequency range, at low frequencies R_{s} strongly affects the capacitance only at high voltages whereas at high frequencies a

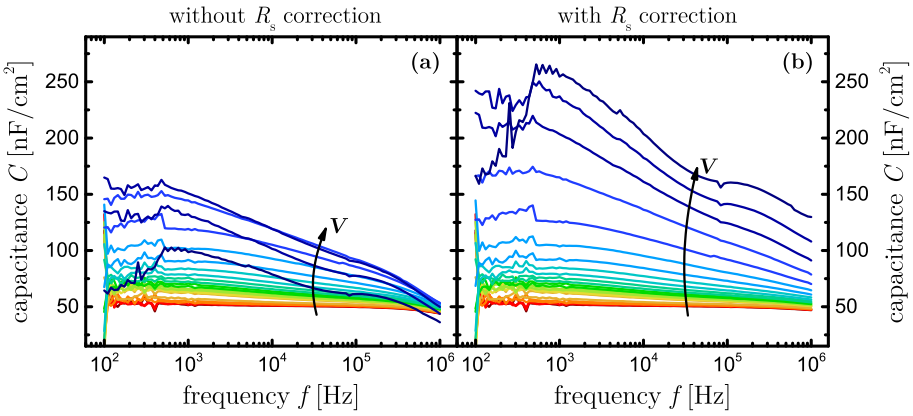

Figure 8.2: Capacitance (a) without and (b) with R_s correction as a function of frequency for voltages ranging from -3 to 0.8 V obtained measuring a PCE10:$PC_{71}BM$ device under 1-sun illumination. At low frequencies the impact of the series resistance is visible only for high voltages whereas at high frequencies R_s causes a rapid decrease in capacitance for all voltages considered.

rapid decrease in capacitance due to R_s can be observed for all the considered voltages. Given the significant influence of R_s, all capacitance-frequency data presented in the following are obtained taking the series resistance into account, i.e. using Eq. (8.10). The R_s value necessary for this correction is determined from the real impedance value Z' obtained measuring the device under investigation in the dark, at high reverse bias, and high frequency. In fact, under these conditions, the few charge carriers present in the active layer are unable to respond to a high frequency AC signal and, thus, the impedance response of the device resembles the one of the resistor R_s.

Figure 8.3(a) shows the capacitance obtained from the simulations as function of frequency of an intrinsic 100 nm-thick device for voltages ranging from -3 to 1 V. Here two plateaus, one at low frequencies and one at high frequencies, are visible. The latter one defines the geometrical capacitance C_g which only depends on the area and the thickness of the active layer. Since the capacitance does not change considerably for frequencies higher than 10^6 Hz and this value is the maximum frequency that the potentiostat used for the subsequent measurements can reach, this was the value taken as f_{high}. The low-frequency capacitance was instead chosen in the region of the first plateau, namely at 10^3 Hz. Figure 8.3(b) compares the different capacitance definitions

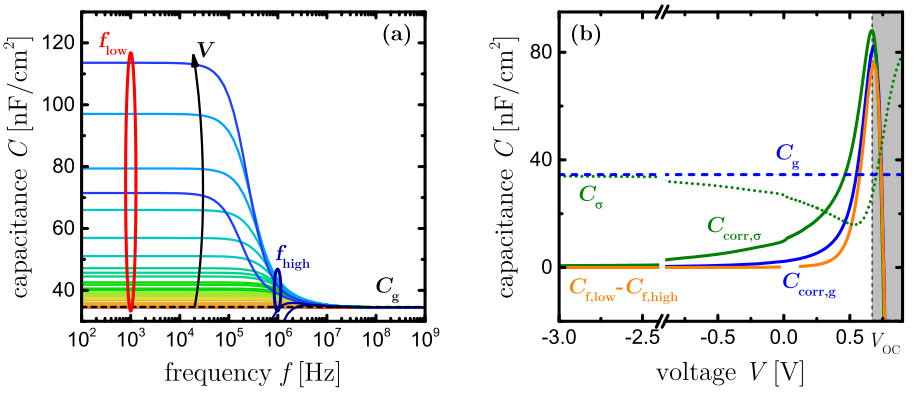

Figure 8.3: (a) Capacitance versus frequency for voltages ranging from -3 to 1 V obtained from SCAPS simulations of an intrinsic solar cell with a 100 nm-thick active layer. One plateau at low frequencies and one at high frequencies, defining the geometrical capacitance C_g, are visible. (b) Comparison of different capacitance definitions for the same simulated cell. The geometrical capacitance C_g and the electrode capacitance C_σ are represented by the blue and green dashed line, respectively. The capacitances $C_{corr,g}$ and $C_{corr,\sigma}$, obtained subtracting C_g or C_σ from the capacitance measured at low frequencies, are displayed in blue and green, whereas the capacitance $C_{f,low} - C_{f,high}$ from the difference between the low-frequency and high-frequency capacitance is plotted in orange.

introduced above and shows that the electrode capacitance C_σ is non-linear and has a larger influence on the results for high voltages. However, there is no obvious way of deducing C_σ from experimental data and thus the calculation of the chemical capacitance for real devices becomes fundamentally difficult.

One easy way to overcome this problem is to determine the excess charge-carrier density under illumination relative to the one in the dark

$$\bar{n}_{ph}(V_{int}) = n_{ph,ref} + \frac{1}{qd}\int_{V_{ref}}^{V_{int}} \left(C_{light}(V_{int}) - C_{dark}(V_{int})\right) dV_{int}, \tag{8.11}$$

with $n_{ph,ref} = \frac{1}{qd}\left(C_{light}(V_{ref}) - C_{dark}(V_{ref})\right) \cdot (V_0 - V_{ref})$ and C_{light} and C_{dark} being the capacitances obtained under illumination and in the dark, respectively. Towards open circuit this strategy is relatively unusable because the injected charge density, whose

influence vanishes upon the calculation of $\bar{n}_{\mathrm{ph}}$, becomes substantial and cannot be neglected. However, at short circuit or reverse bias the excess charge density, i.e the optically injected charge density, approximates rather well the total charge density present in the active layer. Moreover, as it will be shown in the next section, the use of the excess charge-carrier density results in a $\frac{\int(k_{\mathrm{dir}}n(x)p(x)+n(x)/\tau)\mathrm{d}x}{k_{\mathrm{avg}}\bar{n}^2+\bar{n}/\tau_{\mathrm{avg}}}$ ratio closer to unity and, therefore, in a better adherence with the one-dimensional model expressed by Eq. (8.2). Thus, in this voltage range, the $\bar{n}_{\mathrm{ph}}$ definition is quite convenient and, as we will show in the next sections, it allows us to estimate the recombination parameters quite precisely.

8.4 Determination of the SRH Lifetime

Under the assumption of having a solar cell where monomolecular Shockley-Read-Hall (SRH) recombination dominates relative to all other recombination mechanisms, the bulk recombination rate R_{SRH} can be expressed as

$$R_{\mathrm{SRH}} = \frac{np}{\tau_{\mathrm{SRH,p}}n + \tau_{\mathrm{SRH,n}}p}. \tag{8.12}$$

Assuming $\bar{n} \approx \bar{p}$ and $\tau_{\mathrm{SRH,p}} = \tau_{\mathrm{SRH,n}} = \tau_{\mathrm{SRH}}$, the recombination current can be determined via

$$J_{\mathrm{rec}} = q\int_0^d R_{\mathrm{SRH}}\mathrm{d}x \approx qd\frac{\bar{n}}{2\tau_{\mathrm{SRH}}} \tag{8.13}$$

and therefore depends linearly on the charge density. Here, τ_{SRH} represents the average charge-carrier lifetime. By using the excess charge-carrier density $\bar{n}_{\mathrm{ph}}$ defined in Eq. (8.11) and the recombination current as stated in Eq. (8.1), the lifetime can be expressed as

$$\tau_{\mathrm{SRH}} \approx qd\frac{\mathrm{d}\bar{n}_{\mathrm{ph}}}{2\mathrm{d}J_{\mathrm{rec}}} \tag{8.14}$$

and can, thus, be derived from J-V curves and impedance data under illumination. Note that the impedance data used for this method are not a direct measurement of the charge-carrier lifetime and, therefore, are not affected by capacitive discharge effects which, in contrary, have recently been shown to strongly affect the data acquired performing transient photovoltage measurements [158, 160]. Moreover, the effects of

potential capacitive contributions to the charge density are avoided here by using the photocapacitance at reverse bias for the calculation of the excess charge-carrier density.

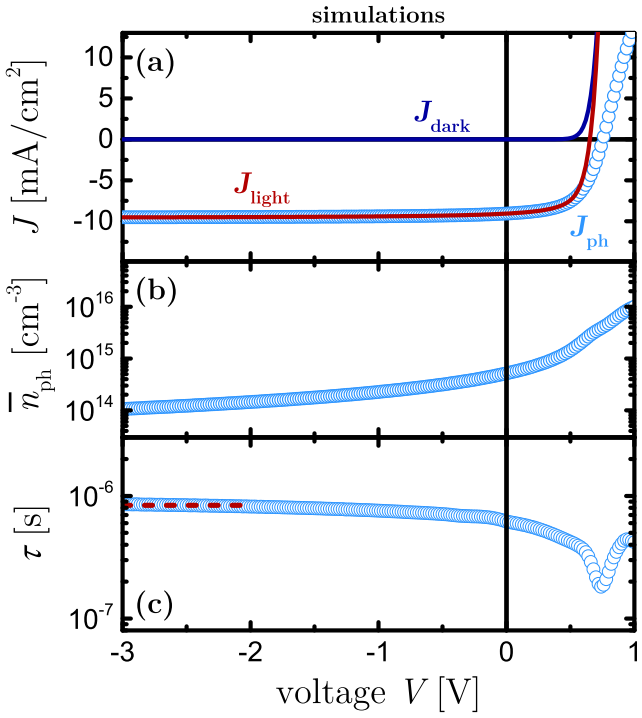

Figure 8.4: (a) Current density, (b) average excess charge density, and (c) lifetime as function of voltage for a simulated 100 nm-thick intrinsic solar cell with Shockley-Read-Hall recombination as dominant recombination mechanism. At high reverse bias, the lifetime approaches the value set for the simulations (1 µs).

Figure 8.4 illustrates the trend of the photocurrent density, the average excess charge density, and the lifetime as function of voltage for a simulated 100 nm-thick intrinsic solar cell. For the calculation of the recombination current J_{rec} by means of Eq. (8.1), the constant generation rate set for the SCAPS simulations ($G = 6 \times 10^{21}$ cm^{-3}s^{-1}) is used. The excess charge density varies with voltage as expected, increasing by two orders of magnitude from -3 to 1 V. Below V_{oc}, the calculated lifetime increases as the voltage is decreased and at high reverse bias it approaches a nearly constant value

which resembles the value of 1 µs set for the simulations. The same value is obtained even when different light intensities are used to perform the simulations, as it is shown in Fig. 8.5. As expected, both the photocurrent and the charge density increase as the light intensity is increased. However, the trend of lifetime as function of voltage remains unaltered, independently of the light intensity. It is crucial to stress that

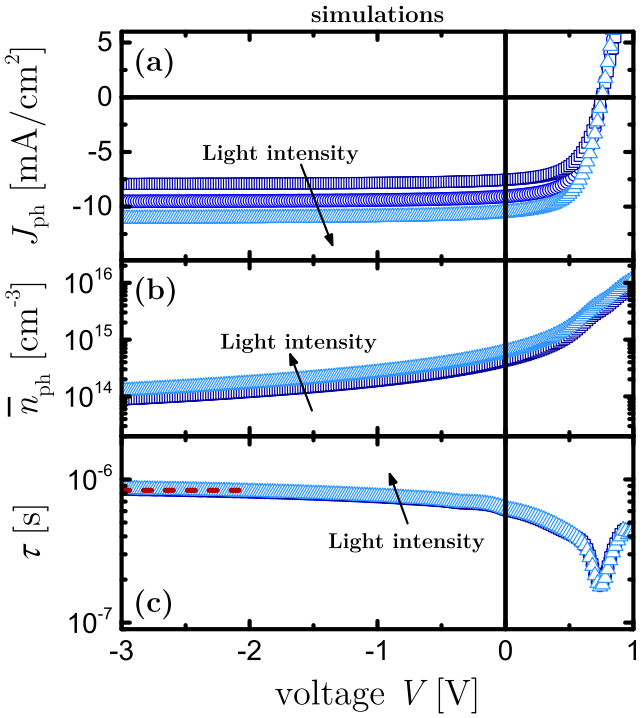

Figure 8.5: (a) Photocurrent density, (b) average excess charge density, and (c) lifetime as function of voltage obtained from the simulations at different light intensities of a 100 nm-thick intrinsic solar cell with Shockley-Read-Hall recombination as dominant recombination mechanism. Both the photocurrent and the charge density increase as the light intensity is increased, whereas the lifetime remains unaltered approaching at high reverse bias the value set for the simulations (1 µs).

the evident decrease in lifetime for voltages approaching V_{oc} in both Fig. 8.4(c) and Fig. 8.5(c) does not coincide with a real change of τ but rather with the breakdown of

the main assumption at the basis of the model presented here, i.e. the possibility of using the excess charge density to approximate the charge density present in the active layer. In fact, as already pointed out in the previous section, the use of the excess charge-carrier density under illumination relative to the one in the dark is an unusable strategy at high forward bias where the injected charge density becomes significant as well as its effect on the charge density in the active layer. In such scenario, the total charge density n is much bigger than the excess charge density, i.e. $n \gg n_{\mathrm{ph}}$, and consequently $J_{\mathrm{rec}} \approx qd\frac{\bar{n}}{2\tau_{\mathrm{SRH}}} \gg qd\frac{\bar{n}_{\mathrm{ph}}}{2\tau_{\mathrm{SRH}}}$, which results in a lifetime determined using Eq. 8.14 lower than the actual value. The behavior observed for τ at high forward bias is therefore to assign to a limitation of the method. Moreover, it is important to stress that the charge lifetime obtained here does not represent the local lifetime but only an average lifetime. This is due to the fact that only the spatially integrated concentration values for electrons and holes are experimentally accessible, and they are usually strong functions of the position in the active layer. This condition is represented in Fig. 8.6

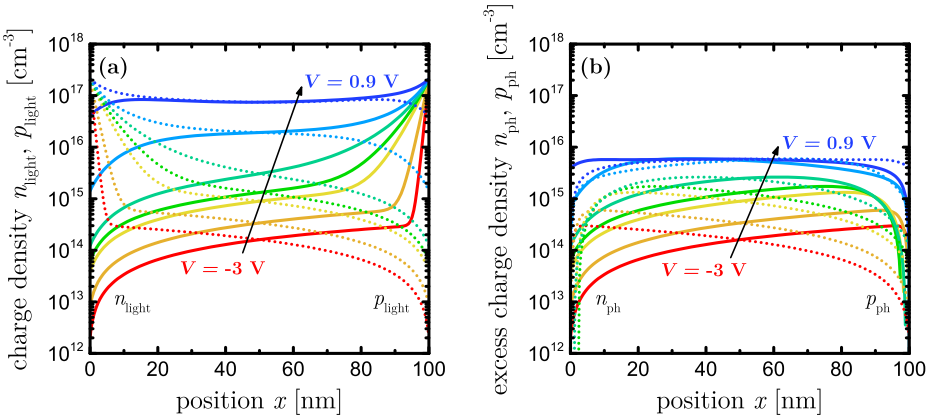

Figure 8.6: Simulations of the spatial distribution of (a) electrons and holes and (b) excess electrons and holes across the active layer of a 100 nm-thick intrinsic solar cell at different voltages. The solid lines refer to the electron density and the dashed lines to the hole density. The same trend as function of voltage is observable for both the total density of electrons n_{light} and holes p_{light} under illumination and the excess electron and hole densities n_{ph} and p_{ph}. However, when the excess charge-carrier densities are considered, the spatial gradients are substantially less steep indicating that this situation resembles more the zero-dimensional model.

which shows the spatial distribution of electrons and holes (Fig. 8.6(a)) and excess electrons and holes (Fig. 8.6(b)) across the active layer of a simulated 100 nm-thick intrinsic solar cell at different voltages. When the total densities of electrons n_{light} and holes p_{light} under illumination are considered (Fig. 8.6(a)), the spatial gradients are quite steep and the increase in concentration as function of voltage is strongly position dependent. As the voltage increases and approaches the built-in voltage, the hole and electron concentrations become more homogeneous and, therefore, the spatial gradients get less steep. The same trend as function of voltage is visible even when the excess electron and hole densities n_{ph} and p_{ph} are considered (Fig. 8.6(b)). However, in this case the spatial gradients are substantially less steep indicating that this situation resembles more the zero-dimensional model discussed in the context of Eq. (8.4). The presence of carrier concentration gradients is responsible for the inequality presented in Eq. (8.3) and, ultimately, for the discrepancy between the local and the average lifetime. The choice of extracting the lifetime from the data at high reverse bias may initially be surprising since, as shown in Fig. 8.6, in this voltage range the carrier concentrations are much more position dependent than at open circuit. However, when the excess charge-carrier density is considered, the left-hand ratio in Eq. (8.3) reaches a nearly constant value closer to 1 at high reverse bias and, consequently, in this voltage range the zero-dimensional model represented by the use of $\bar{n}_{\mathrm{ph}}$ resembles more the one-dimensional model which accounts for the charge-carrier distribution inside the active layer. This behavior is confirmed by Fig. 8.7 which presents the comparison between the left-hand ratio in Eq. (8.3) calculated considering the total charge densities under illumination n_{light} and p_{light} and the one obtained considering the excess charge densities n_{ph} and p_{ph}. When n_{light} and p_{light} are considered, the value of the ratio $\frac{\int\left(n_{\mathrm{light}}(x)\cdot p_{\mathrm{light}}(x)\right)\mathrm{d}x}{\bar{n}_{\mathrm{light}}\cdot\bar{p}_{\mathrm{light}}}$ is close to zero for almost the entire voltage range indicating that, in such a situation, the error introduced using the average charge densities $\bar{n}_{\mathrm{light}}$ and $\bar{p}_{\mathrm{light}}$ is significant. On the other hand, the ratio $\frac{\int\left(n_{\mathrm{ph}}(x)\cdot p_{\mathrm{ph}}(x)\right)\mathrm{d}x}{\bar{n}_{\mathrm{ph}}\cdot\bar{p}_{\mathrm{ph}}}$ obtained considering n_{ph} and p_{ph} does not decrease strongly with decreasing voltages and remains above 0.7 even at high reverse bias.

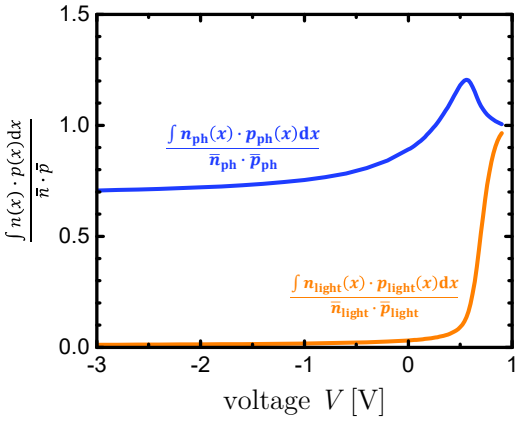

Figure 8.7: Ratio between the charge density obtained considering the charge-carrier distributions inside the active layer, i.e. $\int (n(x) \cdot p(x))\,\mathrm{d}x$, and the product of the spatial average charge-carrier concentrations $\bar{n}$ and $\bar{p}$. The data are obtained from the simulations at different voltages of a 100 nm-thick solar cell. When the charge densities under illumination n_{light} and p_{light} are considered, the ratio approaches zero and therefore the error introduced using the average charge densities strongly increases. In contrast, the ratio obtained considering n_{ph} and p_{ph} is much closer to 1, even at reverse bias. In such a situation, the zero-dimensional model results in a better agreement with the one-dimensional model and, thus, allows a sufficiently accurate determination of the recombination parameters.

8.5 Determination of the Bimolecular Recombination Coefficient

In this section, the determination of the bimolecular or direct recombination coefficient is discussed in an analogous way as done for the monomolecular lifetime before. We now assume that bimolecular recombination is the dominant recombination mechanism, i.e. the recombination rate is given by $R_{\mathrm{dir}} = k_{\mathrm{dir}} n^2$. In this situation, the recombination current depends quadratically on the charge density

$$J_{\mathrm{rec}} \approx q d k_{\mathrm{avg}} \bar{n}^2, \tag{8.15}$$

with k_{avg} being the average bimolecular recombination coefficient. Figure 8.8 well illus-

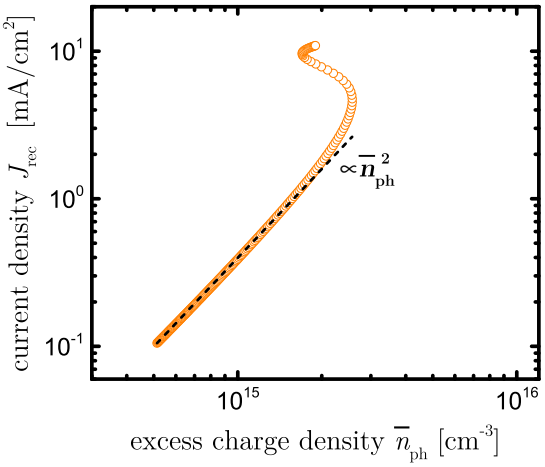

Figure 8.8: Recombination current density J_{rec} as function of the average excess charge density $\bar{n}_{ph}$ for a simulated 100 nm-thick intrinsic solar cell with bimolecular recombination as dominant recombination mechanism.

trates this quadratic relation between recombination current and average excess charge density for a simulated 100 nm-thick intrinsic solar cell with bimolecular recombination as dominant recombination mechanism. Analogously to the procedure followed during the study of the monomolecular lifetime, J_{rec} is obtained by means of Eq. (8.1) considering the constant generation rate set in the software SCAPS ($G = 6 \times 10^{21}$ cm^{-3}s^{-1}). It is evident that for high negative voltages, i.e. where $\bar{n}_{ph}$ well approximates the charge density present in the device, the gradient $d\ln(J_{rec})/d\ln(\bar{n}_{ph})$ is equal to 2, as implied by Eq. (8.15). From Eq. (8.15) it also becomes clear that in this scenario the average bimolecular recombination coefficient can be obtained directly from the recombination current expressed in Eq. (8.1) and the excess charge density defined in Eq. (8.11)

$$k_{avg} \approx \frac{1}{qd} \frac{\mathrm{d}J_{rec}}{\mathrm{d}\bar{n}_{ph}^2}. \tag{8.16}$$

The bimolecular recombination coefficient calculated applying Eq. (8.16) to the data obtained from the simulation of a 100 nm-thick solar cell with $\mu_n = \mu_p = 10^{-4}$ cm^2/Vs and bimolecular recombination as dominant recombination mechanism is displayed as function of voltage in Fig. 8.9(c). Figures 8.9(a) and 8.9(b) show instead the photocur-

rent density and the average excess charge density of the same simulated cell. At biases

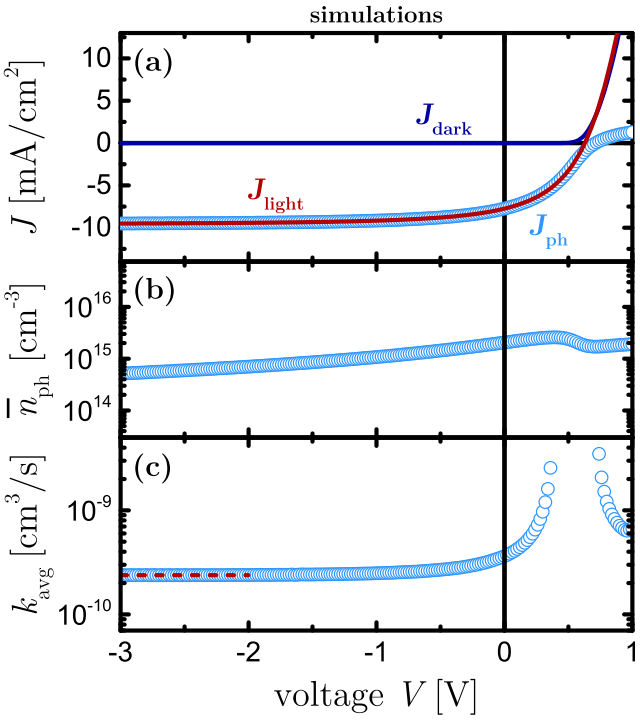

Figure 8.9: (a) Current density, (b) average excess charge density, and (c) average bimolecular recombination coefficient as function of voltage for a simulated 100 nm-thick intrinsic solar cell with $\mu_n = \mu_p = 10^{-4}$ cm^2/Vs and bimolecular recombination as dominant recombination mechanism. The calculated recombination coefficient decreases as the voltage is decreased and at high reverse bias approaches the value used for the simulations (10^{-10} cm^3/s).

smaller than V_{oc}, the calculated recombination coefficient decreases with decreasing voltages approaching the value of 10^{-10} cm^3/s set for the simulations, whereas towards open circuit k_{avg} noticeably increases. The reason for this behavior is found in the impossibility of approximating at forward bias the charge density n present in the active layer with the excess charge-carrier density n_{ph}. In fact, at voltages approaching V_{oc}, the amount of charges present in the active layer is much more affected by the injected

charge density which now greatly exceeds the excess charge-carrier density n_{ph}. This increased impact of the injected charges on the charge density in the active layer results in $n \gg n_{\mathrm{ph}}$ and, consequently, in $J_{\mathrm{rec}} \approx qdk_{\mathrm{avg}}\bar{n}^2 \gg qdk_{\mathrm{avg}}\bar{n}_{\mathrm{ph}}^2$ which in turn leads to an overestimation of k_{avg}. However, it is important to stress that the behavior observed for k_{avg} at high forward bias is to assign to a limitation of the method and not to a real change in the value of the recombination coefficient.

8.6 Experimental Results

In order to test the validity of Eqs. (8.14) and (8.16), capacitance-frequency measurements under 1-sun illumination were performed at different voltages on solar cells fabricated following the procedure illustrated in section 4.2 with the inverted structure glass/ITO/ZnO/PCE10:$PC_{71}BM$/MoO_3/Ag.

Figure 8.10(a) presents the capacitance as function of frequency obtained measuring a 68 nm-thick PCE10:$PC_{71}BM$ based device for voltages ranging from -3 to 0.8 V. The two plateaus, one at low frequencies and one at high frequencies, clearly visible in Fig. 8.3(a) showing the data obtained from SCAPS simulations, are here no longer detectable. Instead, a continuous capacitance decrease with increasing frequency is present at low and intermediate voltages. A noise in the data at frequencies lower than 10^3 Hz is also visible for all the curves shown in Fig. 8.10(a). This behavior has been observed in other polymer:fullerene systems as well and has been attributed to a low shunt resistance due to charges leaking into the active layer from the electrodes [169]. As the applied voltage approaches V_{oc}, in Fig. 8.10(a) two additional shoulders at intermediate frequencies arise and make the identification of reference regions along the frequency axis difficult. The high frequency plateau cannot be reached due to the frequency range limitations of the Gamry Interface 1000 potentiostat used to perform the measurements. Thus, the value at the maximum reachable frequency (10^6 Hz) is considered for the geometrical capacitance calculation. It is clear that in such scenario the determination of the chemical capacitance from the difference between the low-frequency and high-frequency capacitance under illumination, as expressed by Eq. (8.8), becomes problematic and inconvenient. Moreover, as already mentioned in the previous sections, the determination of the non-linear electrode capacitance C_σ from experimental data is not straightforward and, thus, the introduction of its contribution

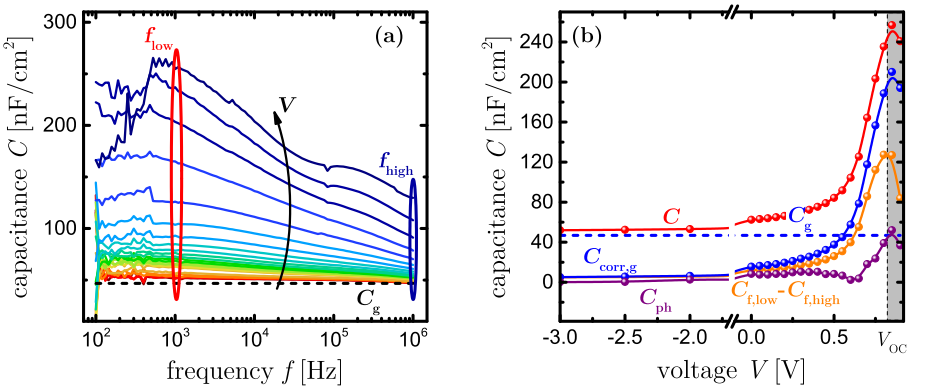

Figure 8.10: (a) Capacitance as function of frequency for voltages ranging from -3 to 0.8 V obtained measuring a PCE10:$PC_{71}BM$ device under 1-sun illumination. No clear and defined plateau is visible and the capacitance monotonously decreases as the frequency increases. (b) Comparison of different capacitance definitions for the same measured device. The capacitance $C_{corr,g}$ obtained subtracting the geometrical capacitance C_g (dashed blue line) from the low-frequency (10^3 Hz) capacitance is displayed in blue, whereas the capacitance $C_{f,low} - C_{f,high}$ from the difference between the low-frequency (10^3 Hz) and high-frequency (10^6 Hz) capacitance is represented in orange. Also showed in purple is the photocapacitance C_{ph} calculated from the capacitances C_{light} and C_{dark} obtained at $f = 10^3$ Hz under illumination and in the dark.

in the calculation of the chemical capacitance becomes difficult to realize. For sake of comparison with the data obtained from SCAPS simulations, the capacitance values from the different definitions presented in section 8.3 are plotted in Fig. 8.10(b). In absence of clear and defined plateaus, the capacitance $C_{f,low} - C_{f,high}$ is obtained considering 10^3 Hz and 10^6 Hz as f_{low} and f_{high}, analogously to the analysis performed on the simulated data. In the same figure is also plotted, as function of voltage, the photocapacitance $C_{ph} = C_{light} - C_{dark}$ at the frequency $f = 10^3$ Hz which was subsequently used to determine the excess charge-carrier density $\bar{n}_{ph}$ according to Eq. 8.11. Figure 8.11 presents as a function of frequency the dark capacitance C_{dark} (Fig. 8.11(a)) obtained measuring for voltages ranging from -3 to 0.8 V the same PCE10:$PC_{71}BM$ device whose capacitance data under illumination are displayed in Fig. 8.10(a). Figure 8.11(b) depicts instead for the same device the photocapacitance $C_{ph} = C_{light} - C_{dark}$ needed for

the determination of the excess charge-carrier density $\bar{n}_{\mathrm{ph}}$.

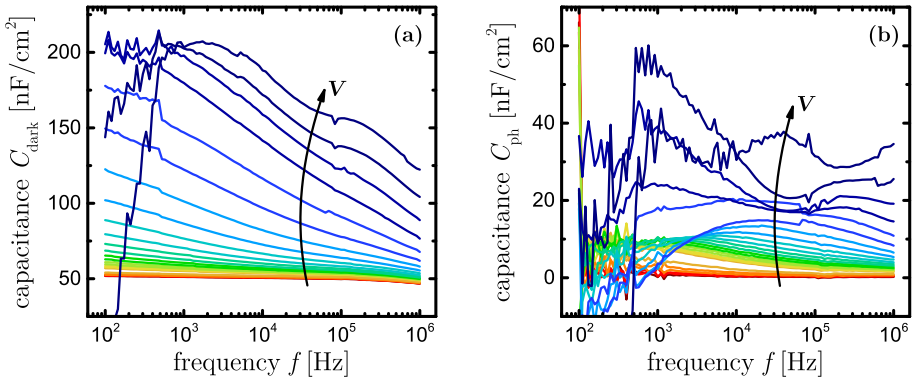

Figure 8.11: (a) Capacitance C_{dark} as function of frequency for voltages ranging from -3 to 0.8 V obtained measuring a PCE10:$PC_{71}BM$ device in the dark. (b) Photocapacitance $C_{\mathrm{ph}} = C_{\mathrm{light}} - C_{\mathrm{dark}}$ as function of frequency for voltages ranging from -3 to 0.8 V calculated from the capacitance values obtained measuring the same device under 1-sun illumination and in the dark.

One of the biggest differences between simulated and experimental data is represented by the smeared-out features in capacitance observed in Fig. 8.10(a). One explanation for this behavior is the presence of lateral disorder which, in the simplest way, can be modeled with two capacitors connected in parallel representing two cells with different charge-carrier mobilities. Figure 8.12 displays the result of this approach, showing the change in the capacitance-frequency curve as the ratio x between capacitors representing the high- and low-mobility cells is varied from 0 to 1. Here, the lower mobility is set to 10^{-5} cm^2/Vs and the higher mobility to 10^{-3} cm^2/Vs. It is evident that for systems with just one mobility (either low or high) the *C-f* curve presents only two clear plateaus, one in the low frequency range and one in the high frequency range. However, when systems with two mobilities are considered, a third plateau at intermediate frequencies arises. Thus, for a system with a broad range of mobilities, multiple plateaus are to be expected and smeared-out capacitance-frequency curves might develop.

Given the difficulties in the determination of the electrode capacitance C_σ, the most convenient way to obtain a charge density that well approximates the charge density

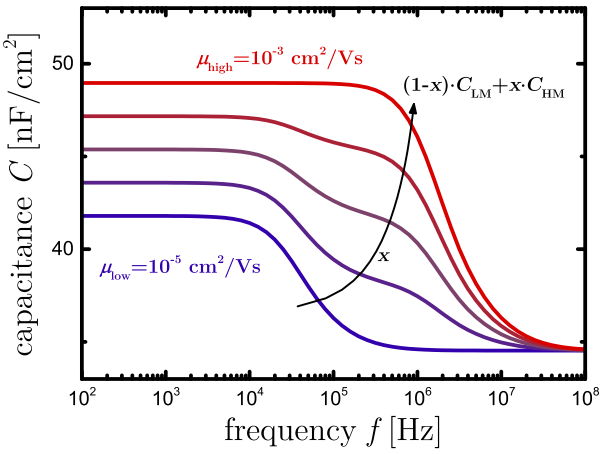

Figure 8.12: Capacitance-frequency curves obtained from a parallel connection of a capacitor representing a cell with low mobility, C_{LM}, and a capacitor representing a cell with high mobility, C_{HM}. As the ratio x between high- and low-mobility capacitors is varied from 0 to 1, a third plateau, in addition to the one in the low frequency range and the one in the high frequency range, becomes visible at intermediate frequencies. Thus, lateral disorder can be accounted for as one possible cause for the smeared-out features in capacitance observed in the experimental data.

in the active layer of the solar cell under investigation is considering the excess charge-carrier density under illumination relative to the one in the dark, as defined in Eq. (8.11). This approach differs significantly from the one presented both by Brus et al. [161] and more recently by Heiber et al. [170] who defined the chemical capacitance as difference between the capacitance measured at low frequency (10^3 Hz) and the capacitance obtained in the dark at the same frequency and at high reverse bias. This calculation of C_{μ} is, in fact, analogous to the calculation based on the subtraction of a constant, voltage-independent geometrical capacitance from the capacitance measured at low frequencies. Thus, it lacks the consideration of the non-linear impact of the charge on the electrodes, which is substantial at voltages approaching V_{oc}, and leads to an underestimation of the charge density present in the active layer, especially at forward bias. The use of the excess charge-carrier density, instead, allows a rather precise estimation of either the charge-carrier lifetime or the bimolecular recombination coefficient,

depending on whether the dominant recombination mechanism is Shockley-Read-Hall or bimolecular recombination. As already highlighted in the previous sections, an indication of the dominant recombination mechanism can be acquired by looking at the trend of the recombination current J_{rec} as function of the excess charge density $\bar{n}_{\mathrm{ph}}$ determined from the values of C_{light} and C_{dark}. In fact, according to Eqs. (8.13) and (8.15) the dependence of the recombination current on the charge density is different for the two mechanisms: linear dependence for SRH recombination and quadratic dependence for bimolecular recombination. Thus, the gradient $d\ln\left(J_{\mathrm{rec}}\right)/d\ln\left(\bar{n}_{\mathrm{ph}}\right)$ at high reverse bias, i.e. where the excess charge density approximation ($n_{\mathrm{ph}} \approx n$) is valid, indicates which recombination mechanism dominates in that voltage range and, therefore, which recombination parameter (charge-carrier lifetime or bimolecular recombination coefficient) can be determined. The possibility to identify the dominant recombination mechanism by the gradient $d\ln\left(J_{\mathrm{rec}}\right)/d\ln\left(\bar{n}_{\mathrm{ph}}\right)$ constitutes an additional difference between the method presented here and the recombination analysis performed recently on the same polymer:fullerene system by Heiber et al. [170]. In fact, in their work Heiber et al. assumed direct recombination as dominant recombination mechanism and extracted the coefficient k_{dir} from the values of the recombination current and the charge density as function of voltage. Note, however, that the identification of the dominant recombination mechanism by looking at the gradient $d\ln\left(J_{\mathrm{rec}}\right)/d\ln\left(\bar{n}_{\mathrm{ph}}\right)$ is possible only if the current density $J_{\mathrm{ph,sat}}$ can be precisely determined.

Before analyzing the *C-f* data of the solar cell under investigation with the same procedure discussed and presented in the previous sections, it is important to stress again that experimental data feature some peculiarities which make some adjustments to the method necessary. Firstly, since the average generation rate cannot be independently determined with sufficient accuracy, the calculation of the saturated photocurrent as $J_{\mathrm{ph,sat}} = q\bar{G}d$ becomes impracticable and $J_{\mathrm{ph,sat}}$ is thus approximated with the value of the photocurrent J_{ph} at the lowest measured voltage, i.e. -3 V in our case. This approximation has direct consequences on the obtained recombination current J_{rec} whose value at -3 V will then be zero, which in turn makes the identification of the dominant recombination mechanism by looking at the gradient $d\ln\left(J_{\mathrm{rec}}\right)/d\ln\left(\bar{n}_{\mathrm{ph}}\right)$ impossible. Secondly, the absence of a clear plateau in the low frequency range of the *C-f* curves in Fig. 8.10(a) noticeably complicates the choice of the frequency for the determination of the excess charge density by means of Eq. (8.11). A feasible way to overcome this

problem is to consider for the determination of the charge density a frequency range, $10^3 < f < 5 \times 10^3$ Hz for instance, instead of a single frequency and calculate $\bar{n}_{\mathrm{ph}}$ as average of the charge densities over this frequency range. By taking these adjustments into account, it is thus possible to determine the excess charge density $\bar{n}_{\mathrm{ph}}$ and the charge-carrier lifetime τ of the solar cell under investigation. Figure 8.13 shows the trend of the photocurrent density, the average excess charge density, and the calculated lifetime as function of voltage for a PCE10:$PC_{71}BM$ solar cell measured under 1-sun illumination. The variation of both charge density and lifetime as function of voltage

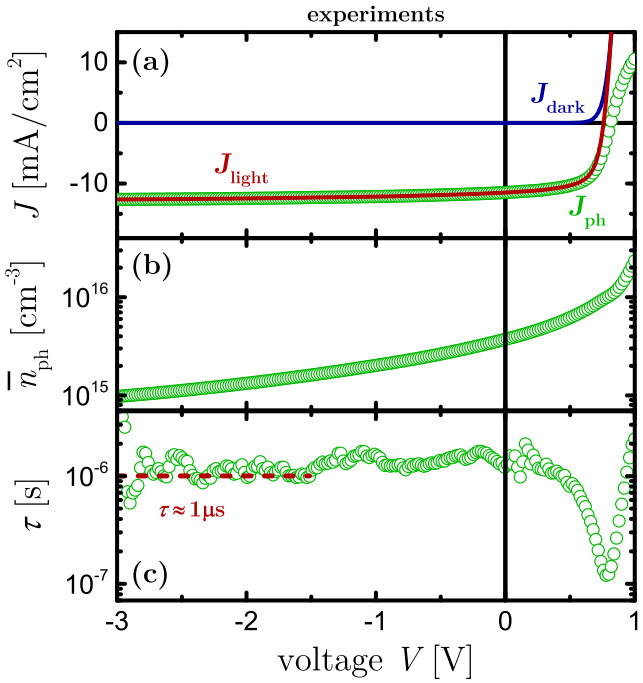

Figure 8.13: (a) Current density, (b) average excess charge density, and (c) calculated lifetime as function of voltage for a PCE10:$PC_{71}BM$ solar cell measured under 1-sun illumination. The lifetime calculated from the recombination current and $\bar{n}_{\mathrm{ph}}$ reaches an average value of approximately 1 µs at high reverse bias.

reflects the behavior observed for the data obtained from SCAPS simulations. The lifetime values are predictably more scattered than the ones obtained from simulations,

but the trend is very alike with τ reaching a saturation at high reverse bias. The error in J_{rec} introduced by the approximation of $J_{\mathrm{ph,sat}}$ with J_{ph} at -3 V is mitigated here by the calculation of τ as average over a relatively broad voltage range. The resulted average lifetime value in that voltage range is $\sim$1 µs and, therefore, in good agreement with the values reported in literature for the same polymer:fullerene system [171–173].

8.7 Conclusions

This chapter presented a method to determine the recombination parameters from impedance measurements on organic solar cells. This approach is based on the charge density dependence of the recombination current, which can be derived from the dark and light current-voltage curves. By means of numerical simulations, it was showed that the use of the density of photogenerated charge carriers as approximation of the charge density present in the active layer allows the identification of the dominant recombination mechanism and the subsequent determination of either the charge-carrier lifetime or the bimolecular recombination coefficient. The application of this method on organic solar cells based on PCE10:$PC_{71}BM$ revealed that for such a system the lifetime can be extracted from impedance data at high reverse bias.

Chapter 9

Conclusions

The main scope of this work was to study charge transport and recombination in organic bulk heterojunction solar cells by means of capacitance-based methods. The key experimental technique was impedance spectroscopy in the form of capacitance-voltage and capacitance-frequency measurements which provide access to the charge-carrier density and insights into recombination parameters such as charge-carrier lifetime and charge-carrier mobility. Impedance spectroscopy, in contrast to other techniques used to investigate recombination dynamics (like time delayed collection field or charge extraction by linear increasing voltage), requires a rather simple setup and allows the testing of organic solar cells under operating conditions. Besides impedance spectroscopy, also current-voltage measurements were used to test the performance of fabricated devices and to discriminate between bulk and surface recombination. The investigated devices contained active layers consisting of the same electron acceptor, namely the fullerene $PC_{71}BM$, but different donor polymers, namely P3HT, PTB7, PBDTTT-C, or PCE10.

A deep analysis of the thickness dependence of the saturation current density derived from the open-circuit voltage and the photocurrent at short circuit or reverse bias allowed the development of a new method to distinguish between surface and bulk recombination in organic solar cells. Thanks to numerical simulations, it was shown that bulk and surface recombination currents scale differently with the active-layer thickness, with the bulk recombination current always increasing with thickness and the surface recombination current decreasing or remaining constant with thickness for active layers thinner than 400 nm. The different scaling with thickness permitted to elucidate if the dominant recombination mechanism in the device under investigation

was surface or bulk recombination. Moreover, the application of the new method on experimental data, both from literature and our laboratory, verified the occurrence of the entire range of cases in the field of organic photovoltaics.

The central part of this work addressed capacitance-voltage measurements on organic solar cells under illumination with the aim of completing the understanding of data obtained from capacitance-voltage measurements under different conditions. Firstly, fully depleted organic solar cells, provided by the use of thin and lowly doped active layers, were considered. A theory of photocapacitance originally developed by Crandall for amorphous silicon solar cells, was demonstrated to be able to approximately describe the capacitance-voltage curves obtained measuring such devices under illumination and, through its application, it was feasible to extract charge-carrier mobility from capacitance-voltage data at reverse bias. A deeper analysis of the discrepancies between the theory of Crandall and the experimental results revealed that they are due to the breaking down, in certain practical cases, of the assumptions required to derive the photocapacitance equation. Furthermore, the significantly lower apparent built-in voltage that would be obtained from Mott-Schottky plots under illumination in comparison to the built-in voltage obtained in the dark was explained by a shift of the onset of space-charge-limited collection with illumination intensity.

After investigating the case of fully depleted organic solar cells under illumination, an analysis of the capacitance of a partly depleted device under illumination and short-circuit conditions was presented. The determination of the charge-carrier density in the neutral region of such device was tackled by comparing three different analytical models for each of which the validity range in terms of absorption coefficient and diffusion length was discussed. The assumptions on which one of the analytical models relies permitted the derivation of two expressions for the photocapacitance, one as function of the charge density and one as function of the charge-carrier lifetime. The obtained expressions enabled the estimation of the lifetime from capacitance-voltage data highlighting that for partly depleted devices under illumination and short-circuit conditions the capacitance is more sensitive to charge-carrier lifetime than to charge-carrier mobility. In addition, the analysis of capacitance-voltage data under illumination obtained simulating devices with different doping densities and active-layer thicknesses demonstrated that under illumination capacitance-voltage data can be strongly affected by either charge-carrier mobility or charge-carrier lifetime depending on the doping level and the active-layer

thickness. This clearly showed that sample properties and measurement conditions affect significantly the applicability of analysis methods for capacitance-voltage data.

Finally, capacitance measurements as a function of frequency and under illumination were addressed and a method to determine the recombination parameters from such measurements on organic solar cells was presented. Numerical drift-diffusion simulations showed that the density of photogenerated charge carriers derived from the photocapacitance well approximates the charge density present in the active layer, especially at reverse bias. The dependence on this charge density of the recombination current allowed to identify the dominant recombination mechanism and to subsequently determine either the charge-carrier lifetime or the bimolecular recombination coefficient. Moreover, capacitance-frequency measurements performed under illumination on organic solar cells based on PCE10:$PC_{71}BM$ revealed that for such a system it is possible to extract the lifetime from the impedance data at high reverse bias.

In summary, this work presented new methods to analyze data from capacitance measurements performed under illumination as a function of voltage or frequency with the aim of completing the understanding of capacitance-voltage data obtained in all possible measurement scenarios and identifying a model-free approach to extract recombination parameters from capacitance-frequency data. By separately addressing the cases of capacitance-voltage measurements on fully depleted and partly depleted devices, the sensitivity of the photocapacitance to either charge-carrier mobility or charge-carrier lifetime was revealed and the importance of considering the sample properties and the measurement conditions during the choice of the analysis method was highlighted. While the lifetime plays a major role in the modulation of the photocapacitance for thick and highly doped devices, the mobility more strongly affects capacitance-voltage curves under illumination in case of low doping densities and small active-layer thicknesses. When the capacitance is measured under illumination as a function of frequency, the use of the obtained photocapacitance for the determination of the photogenerated charge density allows instead a rather precise approximation of the charge-carrier density present in the active layer and the subsequent determination of the recombination parameters. Thanks to the relative simplicity and feasibility of the methods presented here, I believe that this work makes a substantial step forward in the method development needed to further understand the physics of recombination mechanisms in organic solar cells and that it will be interesting to researchers working on organic de-

vices comprising novel semiconducting materials but also those who study any type of thin film solar cell made from 'new' materials and containing different recombination active interfaces.

Bibliography

[1] Directive 2009/28/EC of the European Parliament and of the Council of 23 April 2009, 2009.

[2] COMMUNICATION FROM THE COMMISSION TO THE EUROPEAN PARLIAMENT, THE COUNCIL, THE EUROPEAN ECONOMIC AND SOCIAL COMMITTEE AND THE COMMITTEE OF THE REGIONS A policy framework for climate and energy in the period from 2020 to 2030, 2014.

[3] Statistische Zahlen der deutschen Solarstrombranche (Photovoltaik). Technical report, Bundesverband Solarwirtschaft e.V. (BSW-Solar), 2018.

[4] Solare Fotovoltaico - Rapporto Statistico. Technical report, Gestore dei Servizi Energetici S.p.A., 2017.

[5] A. E. Becquerel. Memoire sur les Effects d'Electriques Produits Sous l'Influence des Rayons Solaires. *Comptes Rendus de l'Academie des Sciences*, 9:561–567, 1839.

[6] D. M. Chapin, C. S. Fuller, and G. L. Pearson. A new silicon p-n junction photocell for converting solar radiation into electrical power. *Journal of Applied Physics*, 25:676–677, 1954.

[7] Martin A. Green, Yoshihiro Hishikawa, Ewan D. Dunlop, Dean H. Levi, Jochen Hohl-Ebinger, and Anita W.Y. Ho-Baillie. Solar cell efficiency tables (version 51). *Progress in Photovoltaics: Research and Applications*, 26:3–12, 2018.

[8] William Shockley and Hans J. Queisser. Detailed balance limit of efficiency of p-n junction solar cells. *Journal of Applied Physics*, 32:510–519, 1961.

[9] Hideki Shirakawa, Edwin J Louis, Alan G MacDiarmid, Chwan K Chiang, and Alan J Heeger. Synthesis of electrically conducting organic polymers: halogen derivatives of polyacetylene, (CH)x. *Journal of the Chemical Society, Chemical Communications*, pages 578–580, 1977.

[10] Frederik C. Krebs. Fabrication and processing of polymer solar cells: A review of printing and coating techniques. *Solar Energy Materials and Solar Cells*, 93:394–412, 2009.

[11] Christoph J Brabec and James R Durrant. Solution-Processed Organic Solar Cells. *MRS Bulletin*, 33:670–675, 2008.

[12] Vishal Shrotriya. Organic photovoltaics: Polymer power. *Nature Photonics*, 3:447–449, 2009.

[13] Rafael Betancur, Pablo Romero-Gomez, Alberto Martinez-Otero, Xavier Elias, Marc Maymó, and Jordi Martorell. Transparent polymer solar cells employing a layered light-trapping architecture. *Nature Photonics*, 7:995–1000, 2013.

[14] Yong Cui, Huifeng Yao, Jianqi Zhang, Tao Zhang, Yuming Wang, Ling Hong, Kaihu Xian, Bowei Xu, Shaoqing Zhang, Jing Peng, Zhixiang Wei, Feng Gao, and Jianhui Hou. Over 16% efficiency organic photovoltaic cells enabled by a chlorinated acceptor with increased open-circuit voltages. *Nature Communications*, 10:2515, 2019.

[15] Runnan Yu, Huifeng Yao, Yong Cui, Ling Hong, Chang He, and Jianhui Hou. Improved Charge Transport and Reduced Nonradiative Energy Loss Enable Over 16 % Efficiency in Ternary Polymer Solar Cells. *Advanced Materials*, 31:1902302, 2019.

[16] Ling Hong, Huifeng Yao, Ziang Wu, Yong Cui, Tao Zhang, Ye Xu, Runnan Yu, and Qing Liao. Eco-Compatible Solvent-Processed Organic Photovoltaic Cells with Over 16 % Efficiency. *Advanced Materials*, 31:1903441, 2019.

[17] Andrea Maurano, Rick Hamilton, Chris G. Shuttle, Amy M. Ballantyne, Jenny Nelson, Brian O'Regan, Weimin Zhang, Iain McCulloch, Hamed Azimi, Mauro Morana, Christoph J. Brabec, and James R. Durrant. Recombination dynamics as a key determinant of open circuit voltage in organic bulk heterojunction solar cells: A comparison of four different donor polymers. *Advanced Materials*, 22(44):4987–4992, 2010.

[18] Lindsay C. C. Elliott, James I. Basham, Kurt P. Pernstich, Pragya R. Shrestha, Lee J. Richter, Dean M. DeLongchamp, and David J. Gundlach. Probing Charge Recombination Dynamics in Organic Photovoltaic Devices under Open-Circuit Conditions. *Advanced Energy Materials*, 4:1400356, 2014.

[19] Makoto Okano, Le Quang Phuong, and Yoshihiko Kanemitsu. Photocarrier dynamics in CIGS, CZTS, and related materials revealed by ultrafast optical spectroscopy. *Physica Status Solidi (B) Basic Research*, 252:1219–1224, 2015.

[20] Sarah R. Cowan, Natalie Banerji, Wei Lin Leong, and Alan J. Heeger. Charge formation, recombination, and sweep-out dynamics in organic solar cells. *Advanced Functional Materials*, 22:1116–1128, 2012.

[21] Riccardo Casalini, Sai Wing Tsang, James J Deininger, Frank a Arroyave, John R Reynolds, and Franky So. Investigation of the Role of the Acceptor Molecule in Bulk Heterojunction Photovoltaic Cells Using Impedance Spectroscopy. *The Journal of Physical Chemistry C*, 117:13798–13804, 2013.

[22] Isaac Zarazua, Juan Bisquert, and Germà Garcia-Belmonte. Light-Induced Space-Charge Accumulation Zone as Photovoltaic Mechanism in Perovskite Solar Cells. *Journal of Physical Chemistry Letters*, 7:525–528, 2016.

[23] Minlin Jiang, Fei Lan, Bingxin Zhao, Quan Tao, Jiamin Wu, Di Gao, and Guangyong Li. Observation of lower defect density in CH3NH3Pb(I,Cl)3 solar cells by admittance spectroscopy. *Applied Physics Letters*, 108:243501, 2016.

[24] Hui Li, Dan He, Qing Zhou, Peng Mao, Jiamin Cao, Liming Ding, and Jizheng Wang. Temperature-dependent Schottky barrier in high-performance organic solar cells. *Scientific reports*, 7:40134, 2017.

[25] Upkar K. Verma, Durgesh C. Tripathi, and Y. N. Mohapatra. Direct determination of defect density of states in organic bulk heterojunction solar cells. *Applied Physics Letters*, 109:113301, 2016.

[26] Antonio Guerrero, Emilio J. Juarez-Perez, Juan Bisquert, Ivan Mora-Sero, and Germà Garcia-Belmonte. Electrical field profile and doping in planar lead halide perovskite solar cells. *Applied Physics Letters*, 105:133902, 2014.

[27] Charles W. Warren, Ellis T. Roe, D. Westley Miller, William N. Shafarman, and Mark C. Lonergan. An improved method for determining carrier densities via drive level capacitance profiling. *Applied Physics Letters*, 110:203901, 2017.

[28] Daniele Menossi, Elisa Artegiani, Andrei Salavei, Simone Di Mare, and Alessandro Romeo. Study of MgCl2 activation treatment on the defects of CdTe solar cells by capacitance-voltage, drive level capacitance profiling and admittance spectroscopy techniques. *Thin Solid Films*, 633:97–100, 2017.

[29] Robert A. Street, Yang Yang, Barry C. Thompson, and Iain McCulloch. Capacitance Spectroscopy of Light Induced Trap States in Organic Solar Cells. *The Journal of Physical Chemistry C*, 120:22169–22178, 2016.

[30] Samira Khelifi, Koen Decock, Johan Lauwaert, Henk Vrielinck, Donato Spoltore, Fortunato Piersimoni, Jean Manca, Abderrahmane Belghachi, and Marc Burgelman. Investigation of defects by admittance spectroscopy measurements in poly (3-hexylthiophene):(6,6)-phenyl C61-butyric acid methyl ester organic solar cells degraded under air exposure. *Journal of Applied Physics*, 110:094509, 2011.

[31] Zhengrong Shang, Thomas Heumueller, Rohit Prasanna, George F. Burkhard, Benjamin D. Naab, Zhenan Bao, Michael D. Mcgehee, and Alberto Salleo. Trade-Off between Trap Filling, Trap Creation, and Charge Recombination Results in Performance Increase at Ultralow Doping Levels in Bulk Heterojunction Solar Cells. *Advanced Energy Materials*, 6:1601149, 2016.

[32] Thomas Kirchartz, Wei Gong, Steven A. Hawks, Tiziano Agostinelli, Roderick C. I. MacKenzie, Yang Yang, and Jenny Nelson. Sensitivity of the Mott-Schottky Analysis in Organic Solar Cells. *The Journal of Physical Chemistry C*, 116:7672–7680, 2012.

[33] Germà Garcia-Belmonte, Pablo P. Boix, Juan Bisquert, Michele Sessolo, and Henk J. Bolink. Simultaneous determination of carrier lifetime and electron density-of-states in P3HT:PCBM organic solar cells under illumination by impedance spectroscopy. *Solar Energy Materials and Solar Cells*, 94:366–375, 2010.

[34] M. Mingebach. Photocurrent in Organic Solar Cells, 2012.

[35] Jenny Nelson. Polymer: Fullerene bulk heterojunction solar cells. *Materials Today*, 14(10):462–470, 2011.

[36] R.E. Peierls. *Quantum Theory of Solids*. Oxford University Press, 1955.

[37] Anna Köhler and Heinz Bassler. *Electronic Processes in Organic Semiconductors*, volume 1. Wiley - VCH, 2015.

[38] C J Brabec and N. S. Sariciftci. Plastic solar cells. *Advanced Functional Materials*, 11(1):15–26, 2001.

[39] Brian A. Gregg. Excitonic Solar Cells. *The Journal of Physical Chemistry B*, 107(20):4688–4698, 2003.

[40] Barry C. Thompson and Jean M.J. Fréchet. Polymer-fullerene composite solar cells. *Angewandte Chemie - International Edition*, 47(1):58–77, 2008.

[41] C. W. Tang. Two-layer organic photovoltaic cell. *Applied Physics Letters*, 48(2):183–185, 1986.

[42] Tracey M. Clarke and James R. Durrant. Charge Photogeneration in Organic Solar Cells. *Chemical Reviews*, 110(11):6736–6767, 2010.

[43] Ala'a F. Eftaiha, Jon-Paul Sun, Ian G. Hill, and Gregory C. Welch. Recent advances of non-fullerene, small molecular acceptors for solution processed bulk heterojunction solar cells. *J. Mater. Chem. A*, 2(5):1201–1213, 2014.

[44] Björn Lüssem, Moritz Riede, and Karl Leo. Doping of Organic Semiconductors. In Wolfgang Brütting and Chihaya Adachi, editors, *Physics of Organic Semiconductors*, pages 427–496. Wiley - VCH, 2012.

[45] V. A. Trukhanov, V. V. Bruevich, and D. Y. Paraschuk. Effect of doping on performance of organic solar cells. *Physical Review B*, 84:205318, 2011.

[46] Uli Würfel, Dieter Neher, Annika Spies, and Steve Albrecht. Impact of charge transport on current-voltage characteristics and power-conversion efficiency of organic solar cells. *Nature Communications*, 6:6951, 2015.

[47] Markus Hösel, Dechan Angmo, Roar R. Søndergaard, Gisele A. dos Reis Benatto, Jon E. Carlé, Mikkel Jørgensen, and Frederik C. Krebs. High-volume processed, ITO-free superstrates and substrates for roll-to-roll development of organic electronics. *Advanced Science*, 1(1), 2014.

[48] Carsten Deibel, Andreas Baumann, and Vladimir Dyakonov. Photogeneration and Recombination in Polymer Solar Cells. In Wolfgang Brütting and Chihaya Adachi, editors, *Physics of Organic Semiconductors*, pages 575–602. Wiley - VCH, 2012.

[49] Paul W M Blom, Valentin D. Mihailetchi, L. Jan Anton Koster, and Denis E. Markov. Device physics of polymer:Fullerene bulk heterojunction solar cells. *Advanced Materials*, 19(12):1551–1566, 2007.

[50] Christoph J. Brabec, Srinivas Gowrisanker, Jonathan J. M. Halls, Darin Laird, Shijun Jia, and Shawn P. Williams. Polymer-Fullerene Bulk-Heterojunction Solar Cells. *Advanced Materials*, 22(34):3839–3856, 2010.

[51] Wallace C H Choy. *Organic Solar Cells: Materials and Device Physics*. 2013.

[52] A. Pivrikas, N. S. Sariciftci, G. Juska, and R. Osterbacka. A Review of Charge Transport and Recombination in Polymer/Fullerene Organic Solar Cells. *Progress in Photovoltaics: Research and Applications*, 15:677–696, 2007.

[53] Carsten Deibel, Thomas Strobel, and Vladimir Dyakonov. Origin of the efficient polaron-pair dissociation in polymer-fullerene blends. *Physical Review Letters*, 103(3):036402, 2009.

[54] Frédéric Laquai, Denis Andrienko, Carsten Deibel, and Dieter Neher. Charge Carrier Generation, Recombination, and Extraction in Polymer-Fullerene Bulk

Heterojunction Organic Solar Cells. In Karl Leo, editor, *Elementary Processes in Organic Photovoltaics*, volume 272, pages 267–291. Springer International Publishing, 2017.

[55] Wolfgang Tress. *Organic Solar Cells: Theory, Experiment, and Device Simulation*. Springer International Publishing, 2014.

[56] Ikerne Etxebarria, Jon Ajuria, and Roberto Pacios. Solution-processable polymeric solar cells: A review on materials, strategies and cell architectures to overcome 10%. *Organic Electronics*, 19:34–60, 2015.

[57] Jong Hyeok Park, Tae-Woo Lee, Byung-Doo Chin, Dong Hwan Wang, and O Ok Park. Roles of Interlayers in Efficient Organic Photovoltaic Devices. *Macromolecular Rapid Communications*, 31(24):2095–2108, 2010.

[58] Tzung Han Lai, Sai Wing Tsang, Jesse R. Manders, Song Chen, and Franky So. Properties of interlayer for organic photovoltaics. *Materials Today*, 16(11):424–432, 2013.

[59] Markus Mingebach, Carsten Deibel, and Vladimir Dyakonov. Built-in potential and validity of Mott–Schottky analysis in organic bulk heterojunction solar cells. *Physical Review B*, 84:153201, 2011.

[60] Juan Bisquert. *The physics of solar cells: Perovskites, Organics, and Photovoltaic Fundamentals*. CRC Press, 2017.

[61] Jenny Nelson. *The Physics of Solar Cells*. Imperial College Press, London, 2003.

[62] Juan Bisquert. *Nanostructured Energy Devices : Equilibrium Concepts and Kinetics*. CRC Press, 2015.

[63] Boyuan Qi and Jizheng Wang. Open-circuit voltage in organic solar cells. *Journal of Materials Chemistry*, 22:24315–24325, 2012.

[64] V. Dyakonov. Mechanisms controlling the efficiency of polymer solar cells. *Applied Physics A: Materials Science and Processing*, 79(1):21–25, 2004.

[65] Jonathan D. Servaites, Mark A. Ratner, and Tobin J. Marks. Organic solar cells: A new look at traditional models. *Energy & Environmental Science*, 4:4410–4422, 2011.

[66] W. Shockley. The Theory of p-n Junctions in Semiconductors and p-n Junction Transistors. *Bell System Technical Journal*, 28:435–489, 1949.

[67] Andres Cuevas. The recombination parameter J0. *Energy Procedia*, 55:53–62, 2014.

[68] Kristofer Tvingstedt and Carsten Deibel. Temperature Dependence of Ideality Factors in Organic Solar Cells and the Relation to Radiative Efficiency. *Advanced Energy Materials*, 6(9):1502230, 2016.

[69] Markus C. Scharber, David Mühlbacher, Markus Koppe, Patrick Denk, Christoph Waldauf, Alan J. Heeger, and Christoph J. Brabec. Design rules for donors in bulk-heterojunction solar cells - Towards 10 % energy-conversion efficiency. *Advanced Materials*, 18:789–794, 2006.

[70] Thomas Kirchartz, Florent Deledalle, Pabitra Shakya Tuladhar, James R. Durrant, and Jenny Nelson. On the Differences between Dark and Light Ideality Factor in Polymer: Fullerene Solar Cells. *Journal of Physical Chemistry Letters*, 4:2371–2376, 2013.

[71] Koen Vandewal, Kristofer Tvingstedt, Abay Gadisa, Olle Inganäs, and Jean V. Manca. On the origin of the open-circuit voltage of polymer-fullerene solar cells. *Nature Materials*, 8:904–909, 2009.

[72] Christoph Waldauf, Marcus C. Scharber, Pavel Schilinsky, Jens A. Hauch, and Christoph J. Brabec. Physics of organic bulk heterojunction devices for photovoltaic applications. *Journal of Applied Physics*, 99:104503, 2006.

[73] R. A. Street, Sarah Cowan, and A. J. Heeger. Experimental test for geminate recombination applied to organic solar cells. *Physical Review B*, 82:121301, 2010.

[74] Ivan G. Scheblykin, Arkady Yartsev, Tonu Pullerits, Vidmantas Gulbinas, and Villy Sundström. Excited state and charge photogeneration dynamics in conjugated polymers. *Journal of Physical Chemistry B*, 111(23):6303–6321, 2007.

[75] Maha A. Alamoudi, Jafar I. Khan, Yuliar Firdaus, Kai Wang, Denis Andrienko, Pierre M. Beaujuge, and Frédéric Laquai. Impact of Nonfullerene Acceptor Core Structure on the Photophysics and Efficiency of Polymer Solar Cells. *ACS Energy Letters*, 3(4):802–811, 2018.

[76] Justin M. Hodgkiss, Andrew R. Campbell, R. Alex Marsh, Akshay Rao, Sebastian Albert-Seifried, and Richard H. Friend. Subnanosecond geminate charge recombination in polymer-polymer photovoltaic devices. *Physical Review Letters*, 104(17):1–4, 2010.

[77] Hyojung Cha, Scot Wheeler, Sarah Holliday, Stoichko D. Dimitrov, Andrew Wadsworth, Hyun Hwi Lee, Derya Baran, Iain McCulloch, and James R. Durrant. Influence of Blend Morphology and Energetics on Charge Separation and Recombination Dynamics in Organic Solar Cells Incorporating a Nonfullerene Acceptor. *Advanced Functional Materials*, 28(3):1–11, 2018.

[78] Sarah R. Cowan, Anshuman Roy, and Alan J. Heeger. Recombination in polymer-fullerene bulk heterojunction solar cells. *Physical Review B*, 82:245207, 2010.

[79] George F Dibb, Fiona C. Jamieson, Andrea Maurano, Jenny Nelson, and James R. Durrant. Limits on the fill factor in organic photovoltaics: Distinguishing nongeminate and geminate recombination mechanisms. *Journal of Physical Chemistry Letters*, 4:803–808, 2013.

[80] Christopher M. Proctor, Chunki Kim, Dieter Neher, and Thuc Quyen Nguyen. Nongeminate recombination and charge transport limitations in diketopyrrolopyrrole-based solution-processed small molecule solar cells. *Advanced Functional Materials*, 23:3584–3594, 2013.

[81] Sung Heum Park, Anshuman Roy, Serge Beaupré, Shinuk Cho, Nelson Coates, Ji Sun Moon, Daniel Moses, Mario Leclerc, Kwanghee Lee, and Alan J. Heeger. Bulk heterojunction solar cells with internal quantum efficiency approaching 100%. *Nature Photonics*, 3:297–302, 2009.

[82] Alexander Foertig, Juliane Kniepert, Markus Gluecker, Thomas Brenner, Vladimir Dyakonov, Dieter Neher, and Carsten Deibel. Nongeminate and Gemi-

nate Recombination in PTB7 : PCBM Solar Cells. *Advanced Functional Materials*, pages 1306–1311, 2014.

[83] Christopher M. Proctor, Martijn Kuik, and Thuc-Quyen Nguyen. Charge carrier recombination in organic solar cells. *Progress in Polymer Science*, 38:1941–1960, 2013.

[84] Davide Bartesaghi, Irene Del Carmen Pérez, Juliane Kniepert, Steffen Roland, Mathieu Turbiez, Dieter Neher, and L. Jan Anton Koster. Competition between recombination and extraction of free charges determines the fill factor of organic solar cells. *Nature Communications*, 6:7083, 2015.

[85] L J A Koster, E C P Smits, V D Mihailetchi, and P W M Blom. Device model for the operation of polymer/fullerene bulk heterojunction solar cells. *Physical Review B*, 72:085205, 2005.

[86] Xugang Guo, Nanjia Zhou, Sylvia J. Lou, Jeremy Smith, Daniel B. Tice, Jonathan W. Hennek, Rocío Ponce Ortiz, Juan T. López Navarrete, Shuyou Li, Joseph Strzalka, Lin X. Chen, Robert P. H. Chang, Antonio Facchetti, and Tobin J. Marks. Polymer solar cells with enhanced fill factors. *Nature Photonics*, 7:825–833, 2013.

[87] Johannes Benduhn, Kristofer Tvingstedt, Fortunato Piersimoni, Sascha Ullbrich, Yeli Fan, Manuel Tropiano, Kathryn A. McGarry, Olaf Zeika, Moritz K. Riede, Christopher J. Douglas, Stephen Barlow, Seth R. Marder, Dieter Neher, Donato Spoltore, and Koen Vandewal. Intrinsic non-radiative voltage losses in fullerene-based organic solar cells. *Nature Energy*, 2:17053, 2017.

[88] Girish Lakhwani, Akshay Rao, and Richard H. Friend. Bimolecular Recombination in Organic Photovoltaics. *Annual Review of Physical Chemistry*, 65:557–581, 2014.

[89] A. V. Nenashev, M. Wiemer, A. V. Dvurechenskii, L. V. Kulik, A. B. Pevtsov, F. Gebhard, M. Koch, and S. D. Baranovskii. Analytical theory for charge carrier recombination in blend organic solar cells. *Physical Review B*, 95:104207, 2017.

[90] Timothy M. Burke, Sean Sweetnam, Koen Vandewal, and Michael D. McGehee. Beyond Langevin recombination: How equilibrium between free carriers and charge transfer states determines the open-circuit voltage of organic solar Cells. *Advanced Energy Materials*, 5:1500123, 2015.

[91] Theresa Linderl, Thomas Zechel, Michael Brendel, Daniel Moseguí González, Peter Müller-Buschbaum, Jens Pflaum, and Wolfgang Brütting. Energy Losses in Small-Molecule Organic Photovoltaics. *Advanced Energy Materials*, 7:1700237, 2017.

[92] Thomas Kirchartz, Tom Markvart, Uwe Rau, and David A. Egger. Impact of Small Phonon Energies on the Charge-Carrier Lifetimes in Metal-Halide Perovskites. *Journal of Physical Chemistry Letters*, 9:939–946, 2018.

[93] Dan Credgington and James R. Durrant. Insights from transient optoelectronic analyses on the open-circuit voltage of organic solar cells. *Journal of Physical Chemistry Letters*, 3:1465–1478, 2012.

[94] Julien Gorenflot, Michael C. Heiber, Andreas Baumann, Jens Lorrmann, Matthias Gunz, Vladimir Dyakonov, and Carsten Deibel. Nongeminate recombination in neat P3HT and P3HT:PCBM blend films. *Journal of Applied Physics*, 115:144502, 2014.

[95] Daniel Rauh, Carsten Deibel, and Vladimir Dyakonov. Charge density dependent nongeminate recombination in organic bulk heterojunction solar cells. *Advanced Functional Materials*, 22:3371–3377, 2012.

[96] Scot Wheeler, Florent Deledalle, Nurlan Tokmoldin, Thomas Kirchartz, Jenny Nelson, and James R. Durrant. Influence of Surface Recombination on Charge-Carrier Kinetics in Organic Bulk Heterojunction Solar Cells with Nickel Oxide Interlayers. *Physical Review Applied*, 4:024020, 2015.

[97] Thomas Kirchartz and Jenny Nelson. Meaning of reaction orders in polymer:fullerene solar cells. *Physical Review B*, 86:165201, 2012.

[98] P. Vanlaeke, A. Swinnen, I. Haeldermans, G. Vanhoyland, T. Aernouts, D. Cheyns, C. Deibel, J. D'Haen, P. Heremans, J. Poortmans, and J. V. Manca.

P3HT/PCBM bulk heterojunction solar cells: Relation between morphology and electro-optical characteristics. *Solar Energy Materials and Solar Cells*, 90:2150–2158, 2006.

[99] Eva Bundgaard and Frederik C. Krebs. Low band gap polymers for organic photovoltaics. *Solar Energy Materials and Solar Cells*, 91:954–985, 2007.

[100] Yongye Liang, Zheng Xu, Jiangbin Xia, Szu Ting Tsai, Yue Wu, Gang Li, Claire Ray, and Luping Yu. For the bright future-bulk heterojunction polymer solar cells with power conversion efficiency of 7.4%. *Advanced Energy Materials*, 22:E135–E138, 2010.

[101] Jianhui Hou, H-Y Hsiang-Yu Chen, Shaoqing Zhang, Ruby I Chen, Yang Yang, Yue Wu, and Gang Li. Synthesis of a low band gap polymer and its application in highly efficient polymer solar cells. *Journal of the American Chemical Society*, 131(43):15586–15587, 2009.

[102] Sih Hao Liao, Hong Jyun Jhuo, Yu Shan Cheng, and Show An Chen. Fullerene derivative-doped zinc oxide nanofilm as the cathode of inverted polymer solar cells with low-bandgap polymer (PTB7-Th) for high performance. *Advanced Materials*, 25:4766–4771, 2013.

[103] Martijn M. Wienk, Jan M. Kroon, Wiljan J. H. Verhees, Joop Knol, Jan C. Hummelen, Paul A. van Hal, and René A. J. Janssen. Efficient Methano[70]fullerene/MDMO-PPV Bulk Heterojunction Photovoltaic Cells. *Angewandte Chemie International Edition*, 42:3371–3375, 2003.

[104] David Mühlbacher, Markus Scharber, Mauro Morana, Zhengguo Zhu, David Waller, Russel Gaudiana, and Christoph Brabec. High photovoltaic performance of a low-bandgap polymer. *Advanced Materials*, 18(21):2884–2889, 2006.

[105] L. Yu Y. Liang, Y. Wu, D. Feng, S.T. Tsai, H.J. Son, G. Li. Development of new semiconducting polymers for high performance solar cells. *J. Am. Chem. Soc.*, 131:56–57, 2009.

[106] Dong Yang, Ping Fu, Fujun Zhang, Nan Wang, Jian Zhang, and Can Li. High efficiency inverted polymer solar cells with room-temperature titanium ox-

ide/polyethylenimine films as electron transport layers. *Journal of Materials Chemistry A*, 2:17281–17285, 2014.

[107] Scott R. Hammond, Jens Meyer, N. Edwin Widjonarko, Paul F. Ndione, Ajaya K. Sigdel, Andrés Garcia, Alexander Miedaner, Matthew T. Lloyd, Antoine Kahn, David S. Ginley, Joseph J. Berry, and Dana C. Olson. Low-temperature, solution-processed molybdenum oxide hole-collection layer for organic photovoltaics. *Journal of Materials Chemistry*, 22:3249–3254, 2012.

[108] Yang (Michael) Yang, Wei Chen, Letian Dou, Wei-Hsuan Chang, Hsin-Sheng Duan, Brion Bob, Gang Li, and Yang Yang. High-performance multiple-donor bulk heterojunction solar cells. *Nature Photonics*, 9:190–198, 2015.

[109] Hsiang-Yu Chen, Jianhui Hou, Shaoqing Zhang, Yongye Liang, Guanwen Yang, Yang Yang, Luping Yu, Yue Wu, and Gang Li. Polymer solar cells with enhanced open-circuit voltage and efficiency. *Nature Photonics*, 3:649–653, 2009.

[110] Derya Baran, Raja Shahid Ashraf, David A Hanifi, Maged Abdelsamie, Nicola Gasparini, Jason A Röhr, Sarah Holliday, Andrew Wadsworth, Sarah Lockett, Marios Neophytou, Christopher J M Emmott, Jenny Nelson, Christoph J Brabec, Aram Amassian, Alberto Salleo, Thomas Kirchartz, James R. Durrant, and Iain McCulloch. Reducing the efficiency-stability-cost gap of organic photovoltaics with highly efficient and stable small molecule acceptor ternary solar cells. *Nature Materials*, 16(3):363–369, nov 2016.

[111] Francisco Fabregat-Santiago, Germà Garcia-Belmonte, Iván Mora-Seró, and Juan Bisquert. Characterization of nanostructured hybrid and organic solar cells by impedance spectroscopy. *Physical Chemistry Chemical Physics*, 13:9083–9118, 2011.

[112] James I. Basham, Thomas N. Jackson, and David J. Gundlach. Predicting the J-V Curve in Organic Photovoltaics Using Impedance Spectroscopy. *Advanced Energy Materials*, 4:1400499, 2014.

[113] Iván Mora-Seró, Germà Garcia-Belmonte, Pablo P. Boix, Miguel A. Vázquez, and Juan Bisquert. Impedance spectroscopy characterisation of highly efficient silicon

solar cells under different light illumination intensities. *Energy & Environmental Science*, 2:678–686, 2009.

[114] Jian V. Li, Alexandre M. Nardes, Ziqi Liang, Sean E. Shaheen, Brian A. Gregg, and Dean H. Levi. Simultaneous measurement of carrier density and mobility of organic semiconductors using capacitance techniques. *Organic Electronics*, 12:1879–1885, 2011.

[115] Jennifer Heath and Pawel Zabierowski. Capacitance Spectroscopy of Thin-Film Solar Cells. In Daniel Abou-Ras, Thomas Kirchartz, and Uwe Rau, editors, *Advanced Characterization Techniques for Thin Film Solar Cells*. Wiley - VCH, 2011.

[116] Benjamin J. Leever, Christopher a. Bailey, Tobin J. Marks, Mark C. Hersam, and Michael F. Durstock. In situ characterization of lifetime and morphology in operating bulk heterojunction organic photovoltaic devices by impedance spectroscopy. *Advanced Energy Materials*, 2(1):120–128, 2012.

[117] Juan Bisquert, Luca Bertoluzzi, Ivan Mora-sero, and Germa Garcia-belmonte. Theory of Impedance and Capacitance Spectroscopy of Solar Cells with Dielectric Relaxation , Drift-Di ff usion Transport , and Recombination. *The Journal of Physical Chemistry C*, 118:18983–18991, 2014.

[118] Alexander Wagenpfahl, Carsten Deibel, and Vladimir Dyakonov. Organic solar cell efficiencies under the aspect of reduced surface recombination velocities. *IEEE Journal on Selected Topics in Quantum Electronics*, 16:1759–1763, 2010.

[119] Andreas Petersen, Thomas Kirchartz, and Thomas A. Wagner. Charge extraction and photocurrent in organic bulk heterojunction solar cells. *Physical Review B*, 85(4):045208, 2012.

[120] Wolfgang Tress, Karl Leo, and Moritz Riede. Optimum mobility, contact properties, and open-circuit voltage of organic solar cells: A drift-diffusion simulation study. *Physical Review B - Condensed Matter and Materials Physics*, 85:155201, 2012.

[121] Pascal Kaienburg, Uwe Rau, Thomas Kirchartz, and Forschungszentrum Jülich. Extracting Information about the Electronic Quality of Organic Solar-Cell Absorbers from Fill Factor and Thickness. *Physical Review Applied*, 6:024001, 2016.

[122] B. E. Pieters, J. Krč, and M. Zeman. Advanced Numerical Simulation Tool for Solar Cells - ASA5. In *Conference Record of the 2006 IEEE 4th World Conference on Photovoltaic Energy Conversion*, pages 1513–1516, Hawaii, 2006. IEEE.

[123] M Burgelman, P Nollet, and S Degrave. Modelling polycrystalline semiconductor solar cells. *Thin Solid Films*, 362:527–532, 2000.

[124] Irene Zonno, Benedikt Krogmeier, Verena Katte, Dana Lübke, Alberto Martinez-Otero, and Thomas Kirchartz. Discriminating between surface and bulk recombination in organic solar cells by studying the thickness dependence of the open-circuit voltage. *Applied Physics Letters*, 109:183301, 2016.

[125] Oskar J. Sandberg, Mathias Nyman, and Ronald Österbacka. Effect of contacts in organic bulk heterojunction solar cells. *Physical Review Applied*, 1:024003, 2014.

[126] A. B. Sproul. Dimensionless solution of the equation describing the effect of surface recombination on carrier decay in semiconductors. *Journal of Applied Physics*, 76(5):2851–2854, 1994.

[127] P. J. Rostan, U. Rau, V. X. Nguyen, T. Kirchartz, M. B. Schubert, and J. H. Werner. Low-temperature a-Si:H/ZnO/Al back contacts for high-efficiency silicon solar cells. *Solar Energy Materials and Solar Cells*, 90:1345–1352, 2006.

[128] L. H. Slooff, S. C. Veenstra, J. M. Kroon, D. J. D. Moet, J. Swelssen, and M. M. Koetse. Determining the internal quantum efficiency of highly efficient polymer solar cells through optical modeling. *Applied Physics Letters*, 90:143506, 2007.

[129] Thomas Kirchartz, Jenny Nelson, and Uwe Rau. Reciprocity between Charge Injection and Extraction and Its Influence on the Interpretation of Electroluminescence Spectra in Organic Solar Cells. *Physical Review Applied*, 5:054003, 2016.

[130] http://www.stanford.edu/group/mcgehee/transfermatrix/index.html.

[131] Oskar J. Sandberg, Anton Sundqvist, Mathias Nyman, and Ronald Österbacka. Relating Charge Transport, Contact Properties, and Recombination to Open-Circuit Voltage in Sandwich-Type Thin-Film Solar Cells. *Physical Review Applied*, 5(4):044005, 2016.

[132] Hoon Park, Jongdeok An, Jongwoo Song, Myounghee Lee, Hyuntak Ahn, Matthias Jahnel, and Chan Im. Thickness-dependent internal quantum efficiency of narrow band-gap polymer-based solar cells. *Solar Energy Materials and Solar Cells*, 143:242–249, 2015.

[133] Gang Li, Vishal Shrotriya, Yan Yao, and Yang Yang. Investigation of annealing effects and film thickness dependence of polymer solar cells based on poly(3-hexylthiophene). *Journal of Applied Physics*, 98(4):043704, 2005.

[134] Jonathan A. Bartelt, Zach M. Beiley, Eric T. Hoke, William R. Mateker, Jessica D. Douglas, Brian A. Collins, John R. Tumbleston, Kenneth R. Graham, Aram Amassian, Harald Ade, Jean M. J. Fréchet, Michael F. Toney, and Michael D. Mcgehee. The importance of fullerene percolation in the mixed regions of polymer-fullerene bulk heterojunction solar cells. *Advanced Energy Materials*, 3(3):364–374, 2013.

[135] Donggu Lee, Junyoung Kim, Seunguk Noh, and Changhee Lee. The Thickness of Active Layer Dependence of Polymer Solar Cells. In *Proceedings of 10th IEEE International Conference on Nanotechnology Joint Symposium with Nano Korea*, pages 1175–1178, 2010.

[136] Irene Zonno, Alberto Martinez-otero, Jan-christoph Hebig, and Thomas Kirchartz. Understanding Mott-Schottky Measurements under Illumination in Organic Bulk Heterojunction Solar Cells. *Physical Review Applied*, 7:034018, 2017.

[137] Boyuan Qi, Zhi-Guo Zhang, and Jizheng Wang. Uncovering the role of cathode buffer layer in organic solar cells. *Scientific Reports*, 5:7803, 2015.

[138] Juan Bisquert, Germà Garcia-Belmonte, Antoni Munar, Michele Sessolo, Alejandra Soriano, and Henk J. Bolink. Band unpinning and photovoltaic model for P3HT:PCBM organic bulk heterojunctions under illumination. *Chemical Physics Letters*, 465:57–62, 2008.

[139] Antonio Guerrero, Sylvain Chambon, Lionel Hirsch, and Germà Garcia-Belmonte. Light-modulated TiOx Interlayer Dipole and Contact Activation in Organic Solar Cell Cathodes. *Advanced Functional Materials*, 24:6234–6240, 2014.

[140] Yu Ning, Longfeng Lv, Yunzhang Lu, Chunmei Zhang, Yi Fang, Aiwei Tang, Yufeng Hu, Zhidong Lou, Feng Teng, and Yanbing Hou. Effects of photo-induced defects on the performance of PBDTTT-C/PC 70 BM solar cells. *Physica Status Solidi (RRL)*, 9:120–124, 2015.

[141] Christopher G. Shuttle, Richard Hamilton, Jenny Nelson, Brian C. O'Regan, and James R. Durrant. Measurement of charge-density dependence of carrier mobility in an organic semiconductor blend. *Advanced Functional Materials*, 20:698, 2010.

[142] Richard S. Crandall. Modeling of thin film solar cells: Uniform field approximation. *Journal of Applied Physics*, 54:7176–7186, 1983.

[143] V D Mihailetchi, J Wildeman, and P W M Blom. Space-Charge Limited Photocurrent. *Physical Review Letters*, 94:126602, 2005.

[144] Ardalan Armin, Aren Yazmaciyan, Mike Hambsch, Jun Li, Paul L. Burn, and Paul Meredith. Electro-Optics of Conventional and Inverted Thick Junction Organic Solar Cells. *ACS Photonics*, 2:1745–1754, 2015.

[145] Jeffrey Gerhart Tait, Ulrich Wilhelm Paetzold, David Cheyns, Mathieu Turbiez, Paul Heremans, and Barry P. Rand. Interfacial Depletion Regions: Beyond the Space Charge Limit in Thick Bulk Heterojunctions. *ACS Applied Materials & Interfaces*, 8:2211–2219, 2016.

[146] Jian Wang, Liang Xu, Yun-Ju Lee, Manuel De Anda Villa, Anton V. Malko, and Julia W. P. Hsu. Effects of Contact-Induced Doping on the Behaviors of Organic Photovoltaic Devices. *Nano Letters*, 15:7627–7632, 2015.

[147] James C. Blakesley, Fernando A. Castro, William Kylberg, George F. A. Dibb, Caroline Arantes, Rog??rio Valaski, Marco Cremona, Jong Soo Kim, and Ji Seon Kim. Towards reliable charge-mobility benchmark measurements for organic semiconductors. *Organic Electronics*, 15:1263–1272, 2014.

[148] Steven A. Hawks, Florent Deledalle, Jizhong Yao, Dylan G. Rebois, Gang Li, Jenny Nelson, Yang Yang, Thomas Kirchartz, and James R. Durrant. Relating Recombination, Density of States, and Device Performance in an Efficient Polymer:Fullerene Organic Solar Cell Blend. *Advanced Energy Materials*, 3:1201–1209, 2013.

[149] Andreas Zusan, Björn Gieseking, Mario Zerson, Vladimir Dyakonov, Robert Magerle, and Carsten Deibel. The effect of diiodooctane on the charge carrier generation in organic solar cells based on the copolymer PBDTTT-C. *Scientific reports*, 5:8286, 2015.

[150] Bernd Ebenhoch, Stuart A.J. Thomson, Kristijonas Genevičius, Gytis Juška, and Ifor D.W. Samuel. Charge carrier mobility of the organic photovoltaic materials PTB7 and PC71BM and its influence on device performance. *Organic Electronics*, 22:62–68, 2015.

[151] Germà Garcia-Belmonte, Antoni Munar, Eva M. Barea, Juan Bisquert, Irati Ugarte, and Roberto Pacios. Charge carrier mobility and lifetime of organic bulk heterojunctions analyzed by impedance spectroscopy. *Organic Electronics*, 9:847–851, 2008.

[152] Florent Deledalle, Thomas Kirchartz, Michelle S. Vezie, Mariano Campoy-Quiles, Pabitra Shakya Tuladhar, Jenny Nelson, and James R. Durrant. Understanding the effect of unintentional doping on transport optimization and analysis in efficient organic bulk-heterojunction solar cells. *Physical Review X*, 5:011032, 2015.

[153] George F. A. Dibb, Mathis-Andreas Muth, Thomas Kirchartz, Sebastian Engmann, Harald Hoppe, Gerhard Gobsch, Mukundan Thelakkat, Nicolas Blouin, Steve Tierney, Miguel Carrasco-Orozco, James R. Durrant, and Jenny Nelson. Influence of doping on charge carrier collection in normal and inverted geometry polymer:fullerene solar cells. *Scientific Reports*, 3:3335, 2013.

[154] Richard S. Crandall. Modeling of thin-film solar cells: Nonuniform field. *Journal of Applied Physics*, 55:4418–4425, 1984.

[155] Arnold R. Moore. Short-circuit capacitance of illuminated solar cells. *Applied Physics Letters*, 27(1):26, 1975.

[156] David Hinken, Karsten Bothe, Klaus Ramspeck, Sandra Herlufsen, and Rolf Brendel. Determination of the effective diffusion length of silicon solar cells from photoluminescence. *Journal of Applied Physics*, 105(10), 2009.

[157] A. Baumann, J. Lorrmann, D. Rauh, C. Deibel, and V. Dyakonov. A new approach for probing the mobility and lifetime of photogenerated charge carriers in organic solar cells under real operating conditions. *Advanced Materials*, 24(32):4381–4386, 2012.

[158] C. G. Shuttle, B. O'Regan, A. M. Ballantyne, J. Nelson, D. D. C. Bradley, J. De Mello, and J. R. Durrant. Experimental determination of the rate law for charge carrier decay in a polythiophene: Fullerene solar cell. *Applied Physics Letters*, 92:093311, 2008.

[159] Irene Zonno, Hayat Zayani, Marcel Grzeslo, Benedikt Krogmeier, and Thomas Kirchartz. Extracting Recombination Parameters from Impedance Measurements on Organic Solar Cells. *Physical Review Applied*, 11:054024, 2019.

[160] David Kiermasch, Andreas Baumann, Mathias Fischer, Vladimir Dyakonov, and Kristofer Tvingstedt. Revisiting lifetimes from transient electrical characterization of thin film solar cells; a capacitive concern evaluated for silicon, organic and perovskite devices. *Energy and Environmental Science*, 11(3):629–640, 2018.

[161] Viktor V. Brus, Christopher M. Proctor, Niva A. Ran, and Thuc-Quyen Nguyen. Capacitance Spectroscopy for Quantifying Recombination Losses in Nonfullerene Small-Molecule Bulk Heterojunction Solar Cells. *Advanced Energy Materials*, 6:1502250, 2016.

[162] V. D. Mihailetchi, P. W.M. Blom, J. C. Hummelen, and M. T. Rispens. Cathode dependence of the open-circuit voltage of polymer:fullerene bulk heterojunction solar cells. *Journal of Applied Physics*, 94(10):6849–6854, 2003.

[163] Andrea Maurano, Chris G. Shuttle, Rick Hamilton, Amy M. Ballantyne, Jenny Nelson, Weimin Zhang, Martin Heeney, and James R. Durrant. Transient optoelectronic analysis of charge carrier losses in a selenophene/fullerene blend solar cell. *Journal of Physical Chemistry C*, 115(13):5947–5957, 2011.

[164] C. G. Shuttle, a. Maurano, R. Hamilton, B. O'Regan, J. C. De Mello, and J. R. Durrant. Charge extraction analysis of charge carrier densities in a polythiophene/fullerene solar cell: Analysis of the origin of the device dark current. *Applied Physics Letters*, 93(18):91–93, 2008.

[165] C G Shuttle, R Hamilton, Brain C O'Regan, J Nelson, and J R Durrant. Charge-density-based analysis of the current-voltage response of polythiophene / fullerene photovoltaic devices. *Proceedings of the National Academy of Sciences of the United States of America*, 107:16448–16452, 2010.

[166] C. Deibel, A. Wagenpfahl, and V. Dyakonov. Origin of reduced polaron recombination in organic semiconductor devices. *Physical Review B*, 80:075203, 2009.

[167] Bernhard Ecker, Hans Joachim Egelhaaf, Roland Steim, Jürgen Parisi, and Elizabeth Von Hauff. Understanding S-shaped current-voltage characteristics in organic solar cells containing a TiO x interlayer with impedance spectroscopy and equivalent circuit analysis. *Journal of Physical Chemistry C*, 116:16333–16337, 2012.

[168] Liang Xu, Yun-Ju Lee, and Julia W. P. Hsu. Charge collection in bulk heterojunction organic photovoltaic devices: An impedance spectroscopy study. *Applied Physics Letters*, 105:123904, 2014.

[169] Michael P Hughes, Katie D Rosenthal, Niva A Ran, Martin Seifrid, and Guillermo C Bazan. Determining the Dielectric Constants of Organic Photovoltaic Materials Using Impedance Spectroscopy. *Advanced Functional Materials*, 28:1801542, 2018.

[170] Michael C. Heiber, Takashi Okubo, Seo-Jin Ko, Benjamin R. Luginbuhl, Niva A. Ran, Ming Wang, Hengbin Wang, Mohammad Afsar Uddin, Han Young Woo, Guillermo C. Bazan, and Thuc-Quyen Nguyen. Measuring the Competition between Bimolecular Charge Recombination and Charge Transport in Organic Solar Cells under Operating Conditions. *Energy & Environmental Science*, 2018.

[171] Wenchao Huang, Eliot Gann, Naresh Chandrasekaran, Shyamal K.K. Prasad, Sheng Yung Chang, Lars Thomsen, Dinesh Kabra, Justin M. Hodgkiss, Yi Bing Cheng, Yang Yang, and Christopher R. McNeill. Influence of Fullerene Acceptor

on the Performance, Microstructure, and Photophysics of Low Bandgap Polymer Solar Cells. *Advanced Energy Materials*, 7:1602197, 2017.

[172] Andrew J. Pearson, Paul E. Hopkinson, Elsa Couderc, Konrad Domanski, Mojtaba Abdi-Jalebi, and Neil C. Greenham. Critical light instability in CB/DIO processed PBDTTT-EFT:PC71BM organic photovoltaic devices. *Organic Electronics*, 30:225–236, 2016.

[173] Wenchao Huang, Eliot Gann, Naresh Chandrasekaran, Lars Thomsen, Shyamal K.K. Prasad, Justin M. Hodgkiss, Dinesh Kabra, Yi Bing Cheng, and Christopher R. McNeill. Isolating and quantifying the impact of domain purity on the performance of bulk heterojunction solar cells. *Energy and Environmental Science*, 10(8):1843–1853, 2017.

List of Symbols

α	absorption coefficient
β_{n}; β_{n}	rate constant for capture of electrons by traps; rate constant for capture of holes by traps
Δn_{a}	excess electron concentration at anode
Δp_{c}	excess hole concentration at cathode
δ	reaction order
η	power conversion efficiency
$\hbar$	Planck's constant/2π
λ	wavelength
μ	charge-carrier mobility
μ_{n}; μ_{p}	electron mobility; hole mobility
ν_{d}	drift velocity of charge carriers
ω	angular frequency
Φ	electrostatic potential
ϕ	photon flux density
ρ	space charge

σ	areal charge density on electrodes
$\sigma_\mathrm{n}; \sigma_\mathrm{p}$	capture cross section for electrons; capture cross section for holes
τ	charge-carrier lifetime
τ_SRH	charge-carrier lifetime with Shockley-Read-Hall recombination
τ_avg	average charge-carrier lifetime
τ_n; τ_p	electron lifetime; hole lifetime
$\upsilon_\mathrm{n,th}$	electron thermal velocity
$\upsilon_\mathrm{p,th}$	hole thermal velocity
ε_0	dielectric permittivity of vacuum
ε_r	relative permittivity of semicondutor
φ_a; φ_c	contact barrier at anode; contact barrier at cathode
ϑ	phase angle
A	area
C	capacitance
C_μ	chemical capacitance per unit area
C_σ	capacitance of electrodes per unit area
C_dark	dark capacitance per unit area
C_g	geometrical capacitance
C_light	capacitance under illumination per unit area
$C_\mathrm{ph,norm}$	generation-rate-normalized photocapacitance
C_ph	photocapacitance per unit area
d	active-layer thickness

D_{n}; D_{p}	electron diffusion coefficient; hole diffusion coefficient
E	energy
E_{CT}	charge-transfer state energy
E_{c}	minimum energy of conduction band
$E_{\mathrm{F_n}}$; $E_{\mathrm{F_p}}$	electron quasi-Fermi level; hole quasi-Fermi level
E_{F}	Fermi level or Fermi energy
E_{g}	energy gap or bandgap
e_{n}; e_{n}	rate constant for electrons release by traps; rate constant for holes release by traps
E_{v}	maximum energy of valence band
F	electric field
f	frequency
f_0	Fermi-Dirac distribution function
FF	fill factor
G	generation rate per unit volume
$g(E)$	density of electronic states per unit energy
I	current
J	current density
$J_{0,\mathrm{B}}$	saturation current density due to bulk recombination
$J_{0,\mathrm{S}}$	saturation current density due to surface recombination
J_0	saturation current density
J_{sc}	short-circuit current density

J_{dark}	dark current density
J_{gen}	current density due to generation
J_{light}	current density under illumination
J_{mpp}	current density at maximum power point
J_{n}; J_{p}	electron current density; hole current density
$J_{\mathrm{ph,sat}}$	saturated photocurrent
J_{ph}	photocurrent density
$J_{\mathrm{rec,B}}$	bulk recombination current density
$J_{\mathrm{rec,S}}$	surface recombination current density
J_{rec}	recombination current density
k_{avg}	average recombination coefficient
k_{B}	Boltzmann's constant
k_{dir}	direct or bimolecular recombination coefficient
k_{L}	Langevin recombination prefactor
n	electron density per unit volume
N_{A}	doping density
N_{c}	effective density of states of conduction band
n_{id}	ideality factor
n_{i}	intrinsic charge-carrier density
n_{light}	total electron density under illumination
n_{ph}	photocharge density per unit volume
N_{t}	density of trap states

n_{t}	electron density when Fermi level coincides with trap energy
N_{v}	effective density of states of valence band
p	hole density per unit volume
P_{light}	incident light power density
p_{light}	total hole density under illumination
p_{t}	hole density when Fermi level coincides with trap energy
Q	charge
q	elementary charge
R	recombination rate per unit volume
R_{s}	series resistance
R_{B}	bulk recombination rate per unit volume
R_{dir}	direct or bimolecular recombination rate per unit volume
R_{i}	internal series resistance
R_{nrd}	non-radiative recombination rate
R_{rec}	recombination resistance
R_{sh}	parallel or shunt resistance
R_{SRH}	Shockley-Read-Hall recombination rate per unit volume
S	surface recombination velocity
S_{na}	surface recombination velocity of electrons at anode
S_{pc}	surface recombination velocity of holes at cathode
T	temperature
t	time

V	voltage or bias
V_0	compensation voltage
V_{bi}	built-in voltage
V_{int}	internal voltage
V_{mpp}	voltage at maximum power point
V_{oc}	open-circuit voltage
w	space-charge region width
Y	admittance
Y'	real part of admittance
Y''	imaginary part of admittance
Y_0	magnitude of constant phase element
Z	impedance
Z'	real part of impedance
Z''	imaginary part of impedance
Z_0	impedance modulus
Z_{CPE}	impedance of constant phase element

List of Publications

- I. Zonno, H. Zayani, M. Grzeslo, B. Krogmeier, T. Kirchartz, "Extracting Recombination Parameters from Impedance Measurements on Organic Solar Cells", *Physical Review Applied*, 11, 054024-1, 2019.
- I. Zonno, A. Martinez-Otero, J. C. Hebig, T. Kirchartz, "Understanding Mott-Schottky Measurements under Illumination in Organic Bulk Heterojunction Solar Cells", *Physical Review Applied*, 7, 034018-1, 2017.
- I. Zonno, B. Krogmeier, V. Katte, D. Lübke, A. Martinez-Otero, T. Kirchartz, "Discriminating between surface and bulk recombination in organic solar cells by studying the thickness dependence of the open-circuit voltage", *Applied Physics Letters*, 109, 183301-1, 2016.
- L. Krückemeier, P. Kaienburg, J. Flohre, K. Bittkau, I. Zonno, B. Krogmeier, T. Kirchartz, "Developing design criteria for organic solar cells using well-absorbing non-fullerene acceptors", *Communications Physics*, 1, 2018.

Band / Volume 516
Zinc Oxide / Nanocrystalline Silicon Contacts for Silicon Heterojunction Solar Cells
H. Li (2020), VIII, 135 pp
ISBN: 978-3-95806-508-6

Band / Volume 517
Iron isotope fractionation in arable soil and graminaceous crops
Y. Xing (2020), X, 111 pp
ISBN: 978-3-95806-509-3

Band / Volume 518
Geophysics-based soil mapping for improved modelling of spatial variability in crop growth and yield
C. Brogi (2020), xxi, 127 pp
ISBN: 978-3-95806-510-9

Band / Volume 519
Measuring and modelling spatiotemporal changes in hydrological response after partial deforestation
I. Wiekenkamp (2020), xxxvii, 276 pp
ISBN: 978-3-95806-512-3

Band / Volume 520
Characterization of Root System Architectures from Field Root Sampling Methods
S. Morandage (2020), xxii, 157 pp
ISBN: 978-3-95806-511-6

Band / Volume 521
Generation Lulls from the Future Potential of Wind and Solar Energy in Europe
D. S. Ryberg (2020), xxvii, 398 pp
ISBN: 978-3-95806-513-0

Band / Volume 522
Towards a Generalized Framework for the Analysis of Solar Cell Performance based on the Principle of Detailed Balance
B. J. Blank (2020), iv, 142 pp
ISBN: 978-3-95806-514-7

Band / Volume 523
A Robust Design of a Renewable European Energy System Encompassing a Hydrogen Infrastructure
D. G. Çağlayan (2020), xxii, 312 pp
ISBN: 978-3-95806-516-1

Band / Volume 524
Control and Optimization of a Lorentz Force Based Actuator System for External Flow
M. F. Seidler (2020), xii, 136 pp
ISBN: 978-3-95806-518-5

Band / Volume 525
ETV Online Tagung 2020 Industrielle Groß- und Hochtemperaturwärmepumpen im Energiesystem
D. Stolten, G. Markowz (Hrsg.) (2020), ca. 71 pp
ISBN: 978-3-95806-519-2

Band / Volume 526
Atmospheric Trace Gas Measurements Using Chemical Ionisation Time-of-Flight Mass Spectrometry
Y. Li (2020), xi, 110 pp
ISBN: 978-3-95806-520-8

Band / Volume 527
Uranium accumulation in agricultural soils as derived from long-term phosphorus fertilizer applications
Y. Sun (2020), XII, 136 pp
ISBN: 978-3-95806-521-5

Band / Volume 528
Entwicklung von Schutzschichten für nicht-oxidische Faserverbundwerkstoffe
M. Wolf (2021), VI, 150, 2 pp
ISBN: 978-3-95806-524-6

Band / Volume 529
Mechanical reliability and oxygen permeation of $Ce_{0.8}Gd_{0.2}O_{2-\delta}$-$FeCo_2O_4$ dual phase membranes
F. Zeng (2021), IV, VI, 222 pp
ISBN: 978-3-95806-527-7

Band / Volume 530
Capacitance-Based Methods to Study Charge Transport and Recombination in Organic Solar Cells
I. Zonno (2021), vi, 153 pp
ISBN: 978-3-95806-528-4

Energie & Umwelt / Energy & Environment
Band / Volume 530
ISBN 978-3-95806-528-4

Mitglied der Helmholtz-Gemeinschaft

JÜLICH
Forschungszentrum